Spray generated by an airblast atomizer: atomization, propagation and aerodynamic instability

Vom Fachbereich Maschinenbau
an der Technische Universität Darmstadt
Zur Erlangung des Grades eines
Doktor-Ingenieurs (Dr.-Ing.)
genehmigte

D I S S E R T A T I O N

Vorgelegt von

Feras Z. Batarseh, M.Sc.

aus Amman, Jordanien

Berichterstatter:	Prof. Dr.-Ing. Cameron Tropea
Mitberichterstatter:	Prof. Dr. Rer. Nat. Andreas Dreizler
	Priv.-Doz. Dr.-Ing. Habil Ilia V. Roisman
Tag der Einreichung:	26.08.2008
Tag der mündlichen Prüfung:	12.11.2008

Darmstadt,2008
D 17

Acknowledgements

I would like to express my sincere gratitude to Prof. Cameron Tropea, the head of SLA, and my supervisor Dr. Ilia Roisman, for their expert guidance and constructive criticism as well as being a constant source of inspiration, throughout this study.

Grateful acknowledgements are due to SLA staff for their assistance and help; the workshop staff for their help realizing the drawings to working facilities, the administrative departments for their logistic support and my colleagues for the constructive discussions and help, especially Benjamin Lambie, Markus Gnirss and Belal Al-Zaitoneh.

I would like to acknowledge the financial support provided by. DAAD for my living expenses in Germany and DFG financial support through project SFB 568-A1 that covered the research cost. Also thanks due to SLA department for the financial support to cover conference expenses.

Finally, a great thanks to my family and my friends, with whom I shared good and also difficult times throughout the duration of this study.

Erklärung

Hiermit erkläre ich, dass ich die vorliegende Dissertation selbständig verfasst und nur die angegebenen Hilfsmittel verwendet habe. Ich habe bisher noch keinen Promotionsversuch unternommen.

Darmstadt,

Feras Zaki Batarseh

Abstract

This thesis presents a study that has been performed to investigate different phenomena exhibited by a spray generated by an airblast atomizer. Three main subjects are addressed:

- Characterization of the spray generated by an airblast atomizer at various operating conditions, including ambient pressure, airflow rate and liquid flow rate.
- Investigation of instationary phenomena in spray, its natural and forced oscillations
- Modelling of spray atomization inside the nozzle

Characterization of both liquid and gas phases of the two-phase flow of an airblast spray is performed using high-speed video imaging, Particle Image Velocimetry and the phase Doppler technique. Three velocity components profiles and size distribution of the droplets in the spray are obtained. The effect of three parameters on the velocity profile and the size distribution, namely; chamber pressure, liquid flow rate and airflow rate has been thoroughly investigated. The collected data can be used for the validation of the numerical Euler-Lagrange code developed for simulation of spray propagation.

Next, spray fluctuations at various chamber pressures are characterized using two techniques, namely; Proper Orthogonal Decomposition of time-resolved images and spectral analysis of laser Doppler velocity data. The airblast spray frequency exhibited a strong dependency on the chamber pressure and the gas-phase flow rate and is totally independent of the liquid phase flow rate. The obtained frequencies from both techniques match each other closely.

Scaling analysis of the spray frequency demonstrates that it depends only on the average air velocity at the nozzle outlet and on the atomizer geometry. A specific Strouhal number is proposed which could be used as a predictive tool for the determination of spray frequencies at various operational conditions. The value of the Strouhal number depends only on the geometry and type of the atomizer. For the atomizer used in this study the empirical value of the Strouhal number is determined as $St = 0.75$.

The effect of oscillating downstream pressure conditions on the airblast spray is qualitatively investigated. It is found that small pressure oscillating magnitudes has a noticeable effect on the spray behavior. Furthermore, the penetration velocity of the spray under the oscillating pressure conditions is estimated by analyzing the high-speed video images. It is found that the penetration velocity and the oscillation frequency increase when increasing the chamber pressure.

Then, in order to better understand the mechanism of film formation in an airblast atomizer with pre-filmer, an auxiliary series of spray impact experiments onto inclined targets experiments are performed the outcome of the impingement process is investigated. The film

thickness of the residual liquid on the target is estimated by processing high-speed video images whereas the ejected droplets are characterized using the phase Doppler technique. The experimental data is used to express the film thickness as function of the primary spray parameters.

Finally, a novel scaling analysis for the droplet size in the airblast spray is proposed based on the energy balance principle in the framework of the chaotic disintegration theory. The model is validated by the comparison with the experimental data from this and other studies.

Kurzfassung

Die vorliegende Arbeit beschäftigt sich mit der Untersuchung verschiedener Phänomene, die bei der Sprayentstehung eines Airblast Zerstäubers auftreten. Drei Hauptaspekte werden betrachtet:

- Charakterisierung des entstehenden Sprays im Airblast Zerstäuber bei verschiedenen Betriebsbedingungen, einschließlich des Umgebungsdrucks
- Untersuchung der instationären Phänomene im Spray sowie der natürlichen und erzwungenen Sprayoszillationen
- Modellierung der Sprayzerstäubung im Inneren der Düse

Die Charakterisierung der flüssigen und gasförmigen Phase der Strömung im Airblast Zerstäuber wurde mittels Hochgeschwindigkeitsaufnahmen, Particle Image Velocimetry und der Phase-Doppler Technik durchgeführt. Dreidimensionale Geschwindigkeitsprofile und die Größenverteilungen der Tropfen im Spray konnten so bestimmt werden. Die Einflüsse des Kammerdrucks, sowie des Flüssigkeits- und Luftvolumenstroms auf das Geschwindigkeitsprofil und die Größenverteilung wurden intensiv untersucht. Die erhaltenen Daten werden für die Validierung des numerischen Euler-Langrange Verfahrens zur Simulation der Sprayausbreitung verwendet.

Zwei Methoden wurden zur Messung der Sprayfluktuationen bei verschiedenen Kammerdrücken angewendet: Proper Orthogonal Decomposition der zeitaufgelösten Bilder und die Spektralanalyse der Laser-Doppler Anemometrie Daten. Die Ergebnisse zeigen, dass die dominante Airblast Sprayfrequenz eine starke Abhängigkeit vom Kammerdruck und dem Volumenstrom der Gasphase aufweist und dabei im untersuchten Parameterbereich völlig unabhängig vom Volumenstrom der flüssigen Phase ist. Die ermittelten Frequenzen beider Techniken zeigen eine enge Übereinstimmung.

Die Skalierungsanalyse der Sprayfrequenzen veranschaulicht, dass die Frequenz ausschließlich von der mittleren Strömungsgeschwindigkeit am Düsenaustritt und von der Zerstäubergeometrie abhängt. In diesem Zusammenhang wird eine Strouhal-Zahl ermittelt, die die Vorhersage der Sprayfrequenzen für verschiedene Betriebszustände erlaubt. Die Strouhal-Zahl hängt hierbei von der Geometrie und Typ des Zerstäubers ab. Der empirisch ermittelte Wert der Strouhal-Zahl für den Zerstäuber der vorliegenden Arbeit beträgt St = 0,75.

Im Weiteren wurde der Einfluss von oszillierendem Drücken auf das Airblast Spray qualitativ untersucht. Es konnte festgestellt werden, dass kleine Druckschwankungen einen deutlichen Einfluss auf das Sprayverhalten haben. Weiterhin wurde die Durchdringungsgeschwindigkeit

des Sprays unter oszillierenden Druckbedingungen mit Hochgeschwindigkeitsaufnahmen abgeschätzt. Dabei zeigte sich, dass die Durchdringungsgeschwindigkeit steigt, wenn Kammerdruck und Oszillationsfrequenz erhöht werden.

Im Hinblick auf ein besseres Verständnis der Mechanismen während der Filmbildung in einem Airblast Zerstäuber mit Filmleger, wurden Experimente zum Sprayaufprall auf einer schiefen Ebene durchgeführt. Die Filmdicke der Restflüssigkeit auf der Oberfläche wurde mit Hochgeschwindigkeitsaufnahmen abgeschätzt und gleichzeitig wurde das Verhalten der entstehenden Tropfen mittels der Phase-Doppler Technik charakterisiert. Aus den experimentellen Daten kann die Filmdicke als Funktion der erfassten Sprayparameter bestimmt werden.

Abschließend wird eine neue Skalierungsmethode für die Tropfengrößen des Sprays basierend auf dem Energieerhaltungsprinzip im Rahmen der „Chaotic Disintegration Theory“ vorgestellt. Das Modell wurde durch den Vergleich mit den Versuchsergebnissen validiert.

Contents

List of figures

List of tables

NOMENCLATURE

Latin characters	Unit	
a	M	typical size of an element in liquid film
b	Mm	bandwidth of a single bar in the histogram
c	m/s	speed of light
d_p	Mm	Droplet diameter
D_{32}	Mm	Sauter Mean Diameter
d_l	M	Thickness of the laser beam
D_i	Mm	Diameter of individual particle
d_t	M	Effective diameter of the measurement volume
$\mathbf{e}_i$		Unit vector of the incident light
$\mathbf{e_s}$		Unit vector of the scattered light,
F	M	Focal length
f_m	Hz	Measured frequency
f_c	Hz	Characteristic frequency
f_D	Hz	Doppler frequency
H	Mm	Film thickness
K	W	kinetic energy of deformation of the element
K		curve weighting
K_i		splash threshold
L_s	M	thickness of the slit
L	M	Length of the pre-filmer
N		minimum number of collected samples
n		Total number of observations or samples
q_n	$cm^3/cm^2/s$	Flux density normal to the target
S	W	Surface energy
$\mathbf{U}$	m/s	Particle velocity
$\overline{U}_{ax}$	m/s	Axial velocity
U_n	m/s	Normal–to-the-wall velocity
U_p	m/s	Parallel–to-the-wall velocity
$\overline{U}_{\varphi}^{*}$	m/s	Characteristic tangential velocity

Subscripts	
ax	Axial
Cal	Calculated
g	Gas
i	Incoming
I	Incident
meas	Measured
n	Normal
o	Outgoing
p	Parallel

Abbreviation	
ACF	Auto correlation function
AFR	Air-to-Fuel mass Ratio
CCD	Charge Coupled Device
LDA	Laser Doppler Technique
PDA	Phase Doppler Technique
PIV	Particle Image Velocimetry
POD	Proper Orthogonal Decomposition
PSD	power spectra density
SMD	Sauter Mean Diameter
SCMH	Standard Cubic Meter per Hour

Greek characters		
α	°	Inclination angle
δ_A	M	Thickness of boundary layer
ε^2		Relative normalized variance
$\dot{\gamma}$	m/s	Rate of deformation
σ	m/s	Surface tension
τ_w	N/m^2	Shear stress
λ_i	M	Wavelength of the incident light
$\sigma_{\overline{\varphi}}^2$		Variance of mean value of quantity φ
φ		Typical measured quantity
Φ	°	Scattering angle
$\Delta\phi_{12}$		Phase shift
θ	°	Trajectory angle
ψ_i	°	Trajectory of individual particle
Δt	S	Time difference between two signals
ρ	kg/ m^3	Density

Dimensionless numbers

Oh	$\frac{\mu}{(\rho\sigma D)^{1/2}}$	Ohnesorge Number
Re	$\frac{\rho U D}{\mu}$	Reynolds Number
S	$\frac{\int_0^{r_0} U_{ax}(r) U_{\varphi}(r) r^2 dr}{r_0 \int_0^{r_0} U_{ax}^2(r) dr}$	swirl number
St	$\frac{f_m D}{\overline{U}_{ax}}$	Strouhal number
ST	$\frac{\tau_{rex}}{\tau}$	Stokes Number
We	$\frac{\rho U^2 D}{\sigma}$	Weber Number

1 Introduction

1.1 General

The atomization of liquid bulk into small droplets in form of a spray is an important process in industrial and combustion systems. By forming droplets, a larger surface area is produced, thus reducing the liquid vaporization time. For liquid-fuelled combustion applications such as liquid fuel injectors for diesel and spark ignition engines, gas turbines, industrial furnaces, rocket engines, etc, this results in better mixing and an increase in the time available for complete combustion [1]. This distributed drop size generation may also be significant for spray cooling, spray painting and agricultural applications. In some applications, the aim of atomization can be mono-size drops generation: cellular micro-encapsulation; medical nebulizers; ink-jet printers or powdered metallurgy [2]. In aero engines, gas turbines and diesel engines the nature of the atomization process plays an important role in controlling NO_x, CO_2 and unburnt hydrocarbons since ignitability and flame stability are dependent on the droplet size of the fuel and air-fuel mixture properties. The mixing mechanisms in combustion chambers involve the disintegration of the liquid phase and forming a homogeneous mixture to avoid single droplet combustion and to create an advantageous spatial distribution of the liquid spray within the combustion chamber [3]. The mechanism of introducing the liquid fuel in the combustor and the mixing process plays a key role in the combustion efficiency in terms of combustion, performance and emissions.

1.2 Airblast atomizers

Most of the atomizers used for industrial applications exploit two types of atomization. The first type is based on the capillary or chaotic breakup of a jet or liquid sheet ejected with high velocity from the nozzle under the high injection pressure, whereas the second type is based on the aerodynamic breakup caused by the shear stresses at the liquid-gas interface.

Other kinds of atomizers use different forms of energy to proceed with the atomization process (for example in electro-spraying, plasma spraying, etc.).

Typical examples of the first type are the pressure swirl atomizer and the simplex atomizer which are used in this work to produce the primary spray in the airblast atomization mechanism and the incoming spray in the spray-wall interaction experiments, respectively.

In airblast atomizers, the kinetic energy of the gas-phase initiates the transformation of the initial continuous medium of the liquid-phase into a discrete form of ligaments and droplets.

In the different available designs of airblast atomizers, the basic objective is to deploy the available air in the most effective way to produce the best atomized liquid phase. Figure 1.1 shows a cross section of an airblast atomizer with pre-filmer, where the liquid phase is initially introduced by a pressure swirl atomizer. The gas phase interacts with the liquid film, first inside the atomizer and subsequently outside the atomizer.

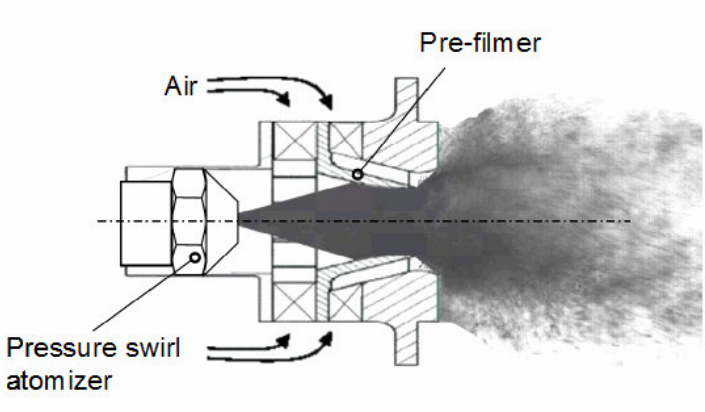

Figure 1.1: Airblast atomizer with pre-filmer.

Different designs of airblast atomizers can be found in the literature. Three types are reported in [1]; a) pre-filming, b) piloted and c) plain-jet airblast atomizers as shown schematically in figure 1.2. In the atomizer shown in figure 1.2a the liquid flows through a number of tangential equally spaced openings onto a pre-filmer before being discharged at the atomization lip where it is subjected to two separate airflows.

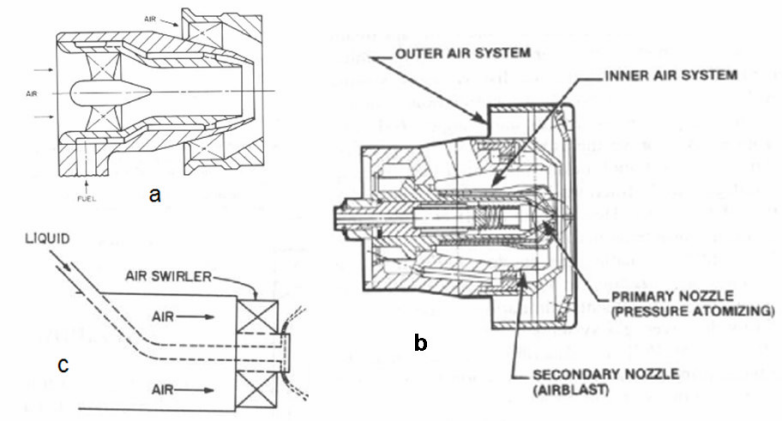

Figure 1.2: Different types of airblast atomizers

A disadvantage of pure airblast atomizers is the poor atomization associated with low air velocities. To overcome this problem, a pressure swirl atomizer or a simplex nozzle can be used to produce atomized droplets in cases where low velocity is dominant. A sample of such

atomizers is shown in figure 1.2 b. The liquid phase can also be introduced directly to the high-velocity air stream in form of discrete jets as in the atomizer shown in figure 1.2 c. In the plain-jet airblast atomizer the liquid flows through a number of radial distributed drilled plain holes, from which discrete liquid jets emerge and enter the swirling air stream.

1.3 Mechanisms of liquid atomization

1.3.1. Atomization of jets and films

Understanding the mechanism of liquid droplets generation from liquid bulk is rather difficult due to the complexity of the phenomenon involved. The efforts that have been made in the past are addressed in [4], in which the effect of surface tension and gravitational forces on the breakup of liquid jets is theoretically introduced to predict the critical conditions under which a non-viscous, laminar liquid bulk in form of a jet breaks up under the effect of gravitational and surface tension forces. This work introduced Rayleigh breakup, which occurs when the wavelength of the disturbance is equal to the circumference in the liquid jets and results in droplets equal to 1.89 times the diameter of the liquid jet. An example of such breakup process is the flow from a commercial shower head as shown in figure 1.3. This theoretical result was originally experimentally validated by [5].

Figure 1.3: Atomization of water jets in a shower by Rayliegh capillary instability.

Further theoretical work has been performed by [6] to consider the effect of viscosity of the liquid, aerodynamic forces and the drag forces on drop formation. This study concluded that the relative velocity between the liquid jet and the surrounding air reduces the wavelength at which the breakup takes place. Experimental results show that four regimes of liquid jet

breakup exist; Rayleigh breakup, where the air doesn't influence the drop formation, formation of drops under the influence of air, formation of drops as a result of sinuous waves on the liquid jet and then a complete disintegration of the liquid jet [7]. The combination of the effects of the surface tension, gravitational forces and the viscous effect of high velocity liquid jets in high air velocity regimes has been treated in [8] in form of a dimensionless number known as the Ohnesorge (Oh) number after extensive visualization of the disintegrating liquid jets of different diameters.

As the main problem in airblast atomizers is the transformation of the liquid bulk in the form of a sheet or film in to drops, early attempts to theoretically investigate this phenomenon can be found in the literature. [9] provide information about the disintegration of planar non-viscous liquid sheets of defined thickness. In this work, the major factors that drive the disintegration process of the liquid sheet into droplets are considered to be the instability of the sheet and the wave formation at the liquid-air interface. An extension of this analytical work to flat, non-viscous liquid sheets by a slender orifice as [10] has done, can reduce the difficulties in [9] analytical treatment of the problem. It is concluded that only two types of waves are possible on the surface of a liquid sheet [10]. Each of the liquid sheet surfaces can be either in-phase to produce sinuous waves or out-of-phase to produce dilatational waves and this yields equation 1.1 for the stable frequency of these waves.

$$f_c = \frac{\rho U^3}{2\pi\sigma} \tag{1.1}$$

In real applications, the liquid film is subjected to more than a simple air stream. In the atomizer used in the present study for instance, a swirl air stream is responsible for the breakup of the liquid film that is generated by an impaction process of the hollow-cone pressure swirl spray onto an inclined pre-filmer. Dombrowski with co-authors [11-14] have performed a series of experiments to investigate various phenomena related to the disintegration of liquid sheets. In [11] they provided photographic information about the breakup of conical liquid sheets emerging from a pressure swirl nozzle and a fan spray. The effects of liquid temperature, viscosity, density and surface tension have been documented. They found that the fundamental concept of disintegration of a radially expanding liquid sheet is the increase of its surface area. They also distinguished between three modes of sheet disintegration; rim, wavy and perforated disintegration. In the rim mode the flow at the edges of the liquid sheet under the action of capillary forces leads to the creation of the rims. In many cases these rims are unstable, their centerline deflects which leads to the appearance of the cusps and finger-like jets. In the wavy mode, the waves on the sheet surface initiate the

disintegration process. In the third mode the film starts to disintegrate in the regions where the thickness is minimal. In [12] Clark and Dombrowski developed a mathematical model for the aerodynamic growth of sinuous waves on parallel sided inviscid liquid sheets. They have obtained an asymptotic analytical solution of the wave growth for the case where the wave length is relatively long comparing to the sheet thickness. The results were compared with the experimental results that have been obtained in [11]. Crapper, Dombrowski and Jepson [13-14] implemented a linear analysis to investigate wave growth on flat sheets of Newtonian and non-Newtonian liquids. They found that the viscosity has no effect on the initial wave growth, and the growth depends only on the sheet velocity and the distance from the nozzle.

1.3.2. Atomization mechanisms in an airblast atomizer with pre-filmer

In an airblast atomizer a hollow-cone spray generated by a pressure swirl atomizer impacts onto a pre-filmer. Under isothermal conditions, this impaction process may produce secondary droplets, but in any case it generates a thin liquid film. This liquid film is subjected to a shear force as a result of the interaction of its free surface with airflow stream. This interaction forces the liquid film to move towards the lip of the pre-filmer where a second swirl air stream deforms its edge and leads to disintegration of the liquid film in form of ligaments and then to small droplets as schematically shown in figure 1.4.

Various mechanisms inside the airblast atomizer lead to atomization and generation of a two-phase flow that leaves the atomizer in the form of spray droplets that are carried by the airstream. The droplets follow the air flow or they develop their own trajectory depending on their size and relative velocity.

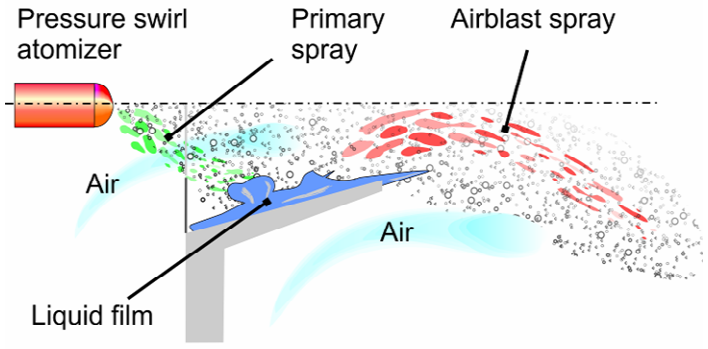

Figure 1.4: Schematic of airblast atomizer with pre-filmer.

The outcome of the different atomization processes inside the airblast atomizer is influenced by many parameters like the volumetric flow rates of the airflow and the liquid flow, parameters of the primary spray, ambient pressure, material properties of the fluids, etc. The flow in the atomizers and the atomization processes are extremely complicated and are not always well described and modeled. Therefore, parametrical studies are important to better understand the effect of these parameters and to serve as a source of modeling concepts.

Such complicated atomization mechanisms can be better investigated if various processes are studied and modeled separately. The following very basic atomization mechanisms in the ariblast atomizer can be distinguished which determine the main integral parameters of the airblast spray:

- Primary spray generation by a pressure swirl nozzle
- Drop evaporation in the atomizer
- Secondary (aerodynamic) drop breakup
- Spray/wall interaction leading to the generation of the secondary spray and spray deposition on the prefilmer
- Disintegration of the liquid film on the prefilmer by an air-flow

The parameters of the *primary spray* for a certain nozzle are determined mainly by the injection and ambient pressure and by the thermodynamic properties of the liquid. These spray parameters can be usually obtained from the nozzle manufacturer. It can be also shown that *drop evaporation* has only minor influence on the drop diameter of the airblast spray, even at the rather high temperatures, since the residence time of the drops inside the atomizer is very small. Moreover, the physics of evaporation of single drops is clearly understood and this process can be thus easily modeled.

Secondary atomization of a single drop and the mechanisms involved in *spray impact* are briefly reviewed below.

The *aerodynamic film disintegration* on the prefilmer leads actually to the generation of the main airblast spray [15]. This phenomenon is not yet completely understood. In this study the theory of chaotic disintegration is applied for the prediction of the diameter of drops in the airblast spray. It is described in the section 6.3.

1.3.3 Secondary breakup of a single drop

An important mechanism in airblast atomization is the secondary atomization, referring to the breakup of a single droplet. The conditions at which the secondary atomization takes place is important to properly understand the effect of the different parameters on the droplet size

distribution in the primary and the final airblast spray and their behavior during the penetration in the pressure chamber.

Liquid drops detached from a liquid film or ligaments, follow certain trajectories, depending on their Stokes number. They may disintegrate into smaller droplets.

Non-uniform distribution of pressure and shear stress on the droplet surface may occur due to the relative motion between the droplet and the surrounding gas. The droplet may disintegrate if these forces overcome the opposing surface tension. The droplets resulted from this disintegration process may undergo further breakup till the surface tension forces are stronger than the external forces [16-17]. It is concluded that the secondary atomization depends on the value of Weber number of the gas phase and Ohnesorge number. In [18] five different mechanisms of secondary atomization are presented based on the Weber number. These regimes are schematically shown in figure 1.5:

- Vibrational atomization ($We_g \leq 12$)
- Bag atomization ($12 < We_g \leq 50$)
- Bag and stamen atomization ($50 < We_g \leq 100$)
- Sheet stripping ($100 < We_g \leq 350$)
- Wave crest stripping followed by catastrophic atomization ($We_g > 350$)

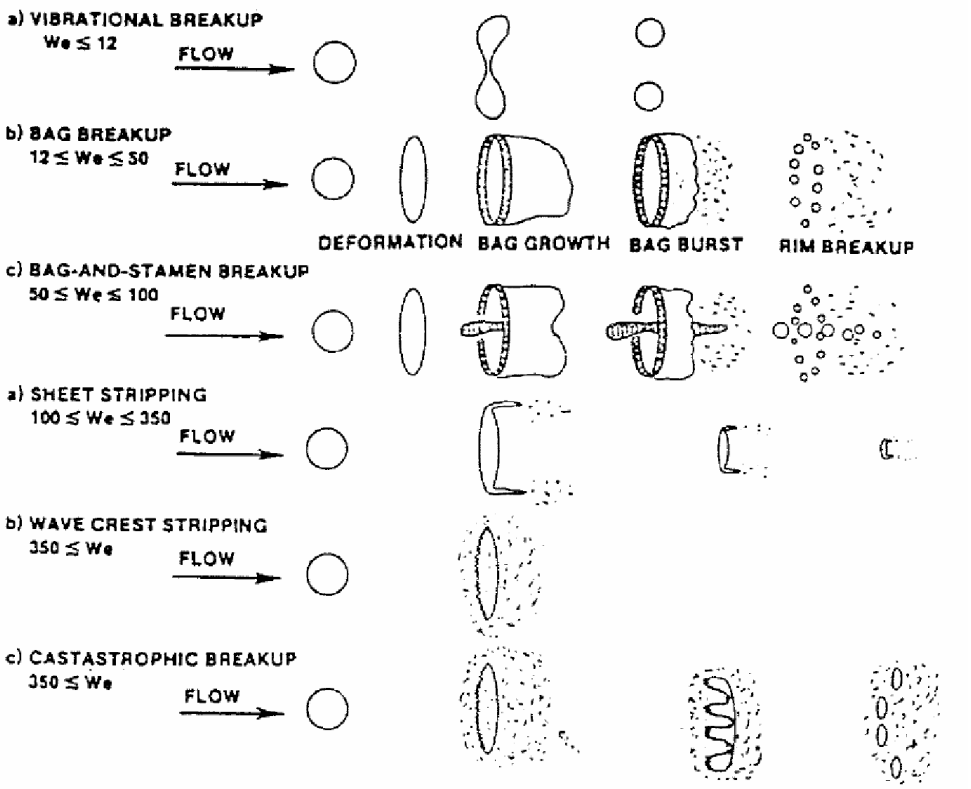

Figure 1.5: Atomization mechanisms of single droplet [17]

The Weber and Ohnesorge numbers are defined as:

$$\mathrm{We_g} = \frac{\rho_g U_{rel}^2 d}{\sigma} \tag{1.2}$$

$$\mathrm{Oh} = \frac{\mu_L}{\sqrt{\rho_L d \sigma}} \tag{1.3}$$

The characteristic breakup time is

$$\tau_{bu} = T_{bu} \frac{d}{U_{rel}} \sqrt{\frac{\rho_L}{\rho_g}} \tag{1.4}$$

where T_{bu} is the dimensionless breakup time and can be determined form the following equations

$$T_{bu} = \begin{cases} 6(\mathrm{We_g} - 12)^{-0.25} & \text{for } 12 \le \mathrm{We_g} \le 18 \\ 2.45(\mathrm{We_g} - 12)^{-0.25} & \text{for } 18 \le \mathrm{We_g} \le 45 \\ 14.1(\mathrm{We_g} - 12)^{-0.25} & \text{for } 45 \le \mathrm{We_g} \le 351 \\ 0.766(\mathrm{We_g} - 12)^{-0.25} & \text{for } 351 \le \mathrm{We_g} \le 2670 \\ 5.5 & \text{for } \mathrm{We_g} \ge 2670 \end{cases} \tag{1.5}$$

The stable diameter at which no further atomization takes place and the corresponding Weber number can be determined by

$$d_{st} = \mathrm{We_{g,crit}} \frac{\sigma}{\rho_g U_{rel}^2} \tag{1.6}$$

$$\mathrm{We_{g,crit}} = 12(1 + 1.007\mathrm{Oh}^{1.6}) \tag{1.7}$$

An estimation of the relevance of the drops secondary breakup is discussed in section 6.1.

1.4 Spray/wall interaction

Spray impact onto surfaces and liquid films is a key phenomenon not only for the spray generation in the airblast atomizers, which is the main subject of this thesis, but also in a wide range of technical and industrial applications. The phenomenon is important in ink-jet printing and painting industries, where the paint drops should stick to the surface without generation of secondary droplets. In gas turbines, high-power electronics and metal industry, spray impact is used for rapid cooling of hot surfaces. On the other hand the effect of spray cooling is not desirable in internal combustion engines, when un-burnt droplets impact on the inner surfaces of the piston and the cylinder, since this leads to higher CO_2 emissions and residual hydrocarbons in the exhaust gases.

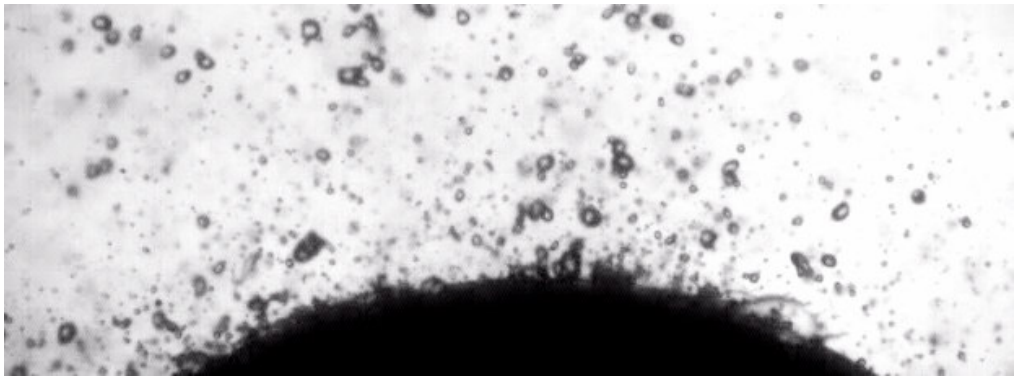

Figure 1.6: Normal spray impact onto a curved surface. Spray impact generates a fluctuating liquid wall film.

Spray impact generates a thin fluctuating liquid film on the substrate surface (see Figure 1.6). This flow is rather complicated and cannot be easily and reliably described using widely accepted approaches, like superposition of single drop impacts or long-wave equation for the evolution of a thin viscous liquid film.

In the airblast atomizer which is used in this work, a primary pressure swirl spray impacts onto the pre-filmer to produce thin liquid film and secondary droplets, then the liquid film breaks up into ligaments and droplets. The thickness of the liquid film along with other parameters (air velocity, surface material, liquid properties) is responsible for the size of the generated airblast spray droplets. Therefore, investigating this phenomenon helps towards a more comprehensive understanding of the airblast atomization mechanism.

The results of the experimental method for the characterization of the film produced by spray impact and its model based on the parameters of the primary spray are given in the section 6.2.

1.5 Fluctuations of a spray generated by an airblast atomizer

The main requirements for clean, stable and efficient combustion are well mixed air-fuel mixture, high volume-mass ratio of the spray and large area to mass ratio of the liquid phase. In different applications, where airblast spray is used, definite spray angle, and stable hollow-cone shape of the spray as well as definite penetration length are important to guarantee acceptable quality of the process as in spray painting for example. In practice, spray generated by an airblast atomizer hardly meet requirements due to different reasons. These reasons can be related to lack of information concerning the mechanisms of spray production inside the atomizer, or due to certain phenomena that exist in two-phase flow in general and in airblast

spray in particular. Thermo-acoustic fluctuations are typical phenomenon related to airblast spray. They appear in swirl flows as a result of pressure variation along flow paths. In the atomizer used in this work, the gas phase is introduced through two levels of radial distributed square holes. These holes are machined tangential relative to the atomizer axis to force the air streams to follow a certain swirl path. This flow geometry yields the so-called precessing vortex core (PVC), which is a widely known phenomenon in pure swirl flow as reported by [19-20]. The PVC can be responsible for combustion instability in gas turbines. Despite extensive efforts in investigating this phenomenon, there is still no universal model to quantitatively predict the frequency of these fluctuations.

Under certain conditions, the thermo-acoustic fluctuations might act as forced oscillations and affect the fundamental properties of the combustion mixture.

In this work, particular attention is paid to investigate both the natural and forced oscillations of the airblast spray, and a new model is presented to estimate the natural oscillation frequency.

1.6 Objectives and contribution of this work

The main aim of this experimental work is the characterization of the spray generated by a MTU airblast swirl atomizer, in particular a description of its atomization, propagation and instability. The research strategy is based on the detailed investigation of the main elements involved in the atomization process in order to validate the numerical tools for the spray prediction and to develop the atomization model:

- Characterization of the main integral parameters of the airblast spray, including the parameters of the liquid drops and the airflow
- Characterization of the instationary phenomena in spray propagation, measurements of the frequency of its natural and forced fluctuations
- Characterization of the primary spray and investigation of its influence on the airblast spray
- Characterization of inclined spray impact in application to the impact of the primary spray on the prefilmer in an airblast atomizer, modeling of the wall film thickness
- Development of a universal atomization model which is able to predict the typical diameter of the drops in the airblast spray on the base of the parameters of the primary spray, wall film thickness, airflow and density.

The experimental data collected in this work describes the steady and unsteady behavior of the airblast spray under various operating conditions. It provides information concerning the effect of the ambient pressure, airflow rate and water flow rate on the Sauter mean diameter of the droplets and their velocity vectors, and their behavior during penetration in the pressure chamber. The experimental data for different operating conditions is presented in several publications [21-23].

The work for this dissertation has been performed as a part of a larger project that focuses on flow and combustion in future gas turbine combustion chambers "SFB 568". The subproject A1 focuses on delivering the experimental data on the droplet size distribution and velocity profile of liquid droplets in an MTU airblast atomizer under isothermal conditions to validate numerical models that are developed by different subprojects (A4). A sample result [21-24] of the comparison between experimental data and numerical simulations performed in the framework of the subproject A4 is shown in figure 1.7.

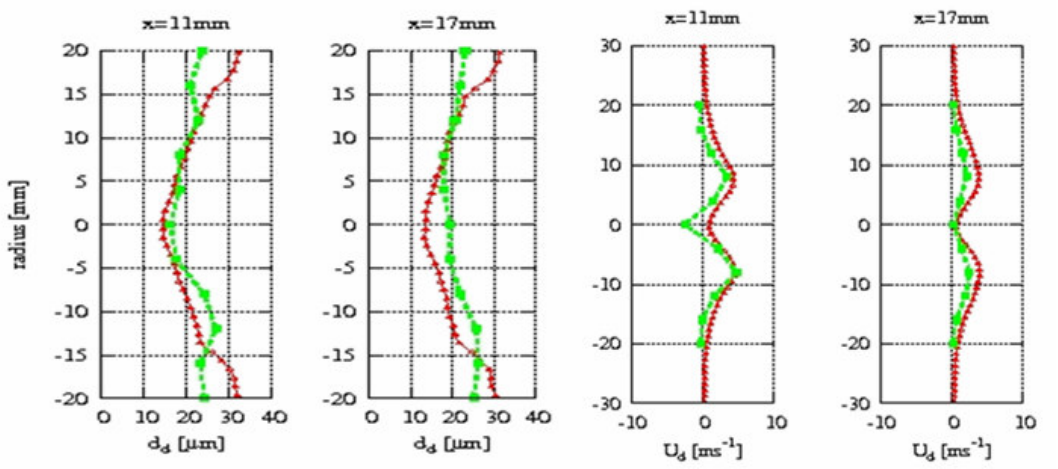

Figure 1.7: Comparison between experimental (-) and numerical (-) results, chamber pressure of 5 bars, airflow rate of 20SCMH and water flow rate of 1.94 l/hr.

In the MTU airblast atomizer used in this study, the airflow follows a swirl path which leads to the precessing vortex core phenomenon. This phenomenon is extensively investigated by different groups, but still a unified scaling of the rate of detachment of the PVC is missing.

Under actual operating conditions of gas turbines, pressure oscillations inside the combustion chamber may occur, which could lead to the combustion instabilities or even to the chamber destruction. These pressure oscillations and their effect on the airblast spray have been investigated by different researchers, where a certain percentage of the incoming air to the atomizer is subjected to pressure oscillations. In this work the airflow is subjected to pressure

oscillations at different frequencies at different chamber pressures which has led to unexpected new results. In this work, a universal scaling for the spray frequency is proposed and validated by the experimental data [25-26].

A significant part of this study is devoted to the investigation of spray impact and the development of the experimental methodology of the characterization of the film created by spray impact. Moreover, a model for the film thickness is proposed based on the analysis of the single drop impact onto a liquid film and scaled by a thickness of the viscous boundary developed during spray impact.

Finally, the experimental data are used to a validate the chaotic disintegration model able to predict the Sauter mean diameter of droplets in the airblast spray based on the energy balance of the two phases of the flow.

1.7 Thesis overview

Literature has been reviewed for each chapter of this thesis and placed in an appropriate order based on the subject and objective of each part.

In chapter 2, the experimental setup and the measurement techniques are described. The capabilities of the pressure chamber, description of the airblast atomizer and the compressed air system are given. Furthermore, basic information concerning the phase Doppler technique, Particle Image Velocimetry and high-speed video system is introduced.

Visualization of spray generated by an airblast atomizer, including the gas-phase, is reported in chapter 3. Moreover, high-speed video images of the primary spray that impacts onto the airblast atomizer pre-filmer are also presented.

Simple scaling analysis of the spray frequency is presented in chapter 4. The effect of different parameters on the spray frequency is also discussed. The results obtained by performing experiments under oscillating pressure conditions are also presented and clarified.

Chapter 5 is devoted to the airblast spray characterization. The effect of airflow rate, water flow rate and chamber pressure on the droplet size distribution and velocity profile in pressure swirl spray and airblast atomizer is performed. Further results concerning the air velocity based on the LDA results and PDA data of the liquid phase is displayed.

A model for estimation of droplet size in airblast spray based on energy balance in the framework of chaotic disintegration of liquid films is presented. In chapter 6 the model is formulated after a thorough discussion of the potential generation of the droplets in the airblast spray. Moreover, an empirical correlation for the film thickness on the pre-filmer of an airblast atomizer is presented.

2. Experimental setup and instrumentation

2.1 Pressure chamber and spray system

Pressure chamber

All the experiments devoted to the characterization of the spray produced by the airblast atomizer have been performed in a stainless steel pressure chamber that can withstand up to 50 bars. This feature allows the isothermal operating conditions of the most advanced aero engine combustors to be simulated. Part of the advantage is given up by using water instead of kerosene as a test fluid. Actual experiments are performed under the chamber pressure up to 15 bar corresponding to the operating range of smaller engines.

The pressure chamber, shown in figure 2.1, has three optical accesses at 0º, 90º and 240º to facilitate the use of PDA, PIV and high-speed video (time resolved) imaging technique.

Compressed air flows to the chamber through two paths. The first one leads to the atomization cup where the airblast atomizer is mounted, and the second one leads directly to the chamber to maintain the pressure within. The source of the compressed air is a compressor that charges a pressure vessel of 18 m^3, which ensures continuous stable airflow. The standard air-mass flow rate to the atomization cup is measured using a CTA based device (KURZ). The pressure drop between the air source and the chamber is regulated by a pressure reducing valve. The pressure and the airflow rate are controlled by means of a system of manual ball valves. To buildup the pressure within the chamber, for example, the BV3 is partially close, and then BV2 is gradually opened until the required pressure is available. Valve BV1 allows a fine adjustment of the airflow rate.

Atomizer

The liquid phase is introduced to the airblast atomizer in the form of a pressure swirl spray, produced using a pressure swirl atomizer. A reciprocating pump provides the pressure swirl atomizer with continuous flow at the specified flow rate, adjusted using the stroke length of the pump's piston. A MTU atomizer is used to produce the airblast spray. The dimensions and the geometry of the airblast atomizer are shown in figure 2.2.

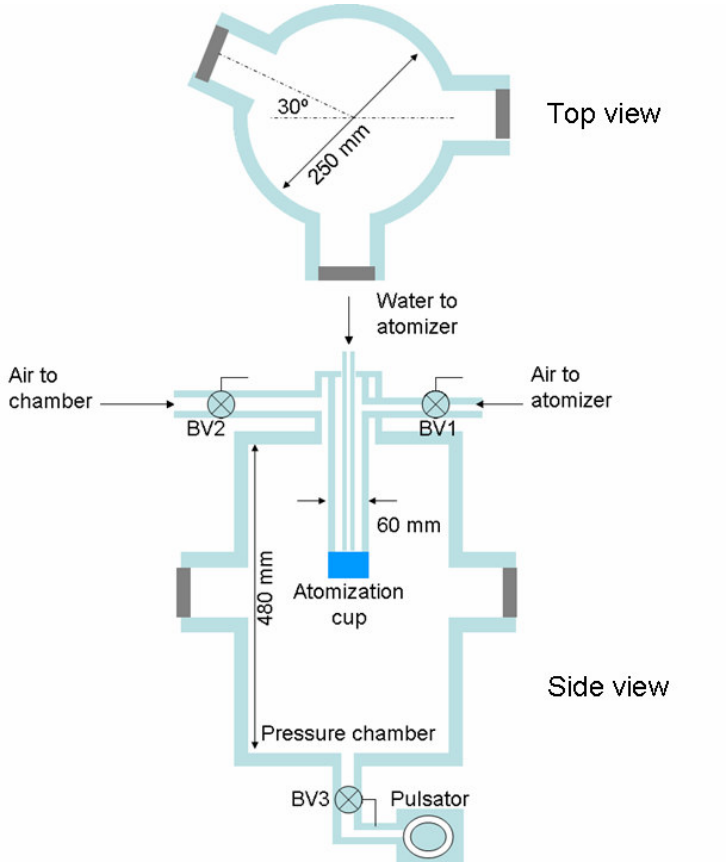

Figure 2.1: Pressure chamber

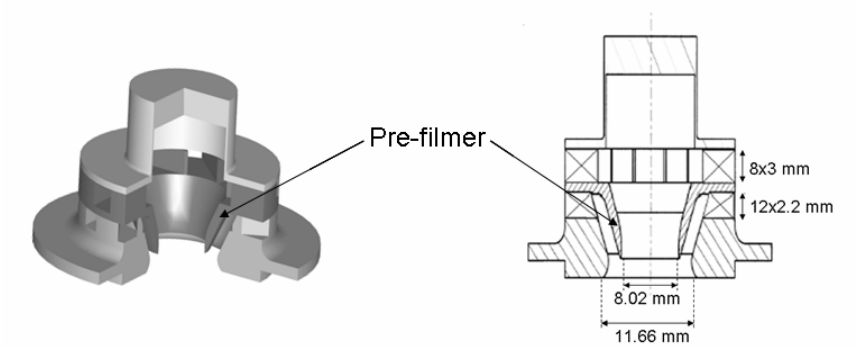

Figure 2.2: MTU airblast atomizer with pre-filmer

Spray impact facility

A spray impact facility is used to simulate the processes taking place inside the airblast atomizer. A simplex nozzle is used to produce a spray that impacts onto a Plexiglas surface mounted with different angles θ, as shown in figure 2.3.

In the case of spray impact onto the Plexiglas surface under atmospheric pressure, a pressure vessel is used to provide the nozzle with continuous water flow. The water flow rate to the simplex nozzle is measured using a commercial flow meter. The angle θ has been changed

between 15, 30, 45 and 60 degrees. PDA measurements are performed to measure diameter and two velocity components of the incoming and the secondary droplets.

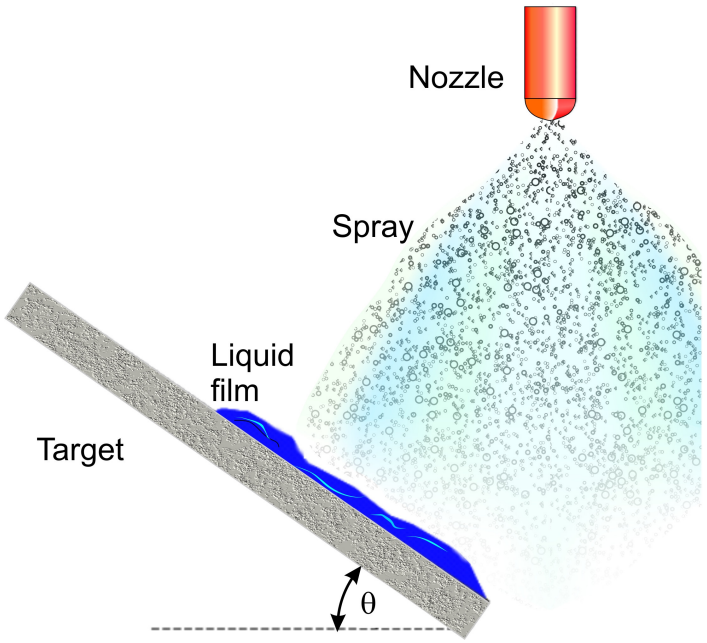

Figure 2.3: Schematic of the spray impact facility

2.2 Laser Doppler/Phase Doppler Techniques (PDA)

The LDA is a non-intrusive point-measurement technique to measure local velocity of droplets, bubbles or particles in the flow. This technique enables remote measurements of up to three velocity components simultaneously with values as high as 1000 m/s depending on the optical configuration of the system. Detailed information of the system and the theory behind it is mentioned in [27].

In this work, a dual Phase Doppler Technique (PDA) is used to measure velocity and diameter of the droplets in the airblast spray, the primary sprays and to characterize the incoming and outgoing droplets in spray-wall interaction experiments. An Argon-Ion, water cooled-laser , which generates power of 10W output, at 514.5 nm and 488 nm wavelengths for the green and blue beams is used.

The PDA system, operated in coincident first order refraction scatter enabled the simultaneous measurement of both axial and vertical velocities. It is able to estimate also some integral and statistical parameters, like volume flux density vector, and 2-D fluctuating velocity correlations. A top view of the pressure chamber and the PDA optics is sketched in figure 2.4.

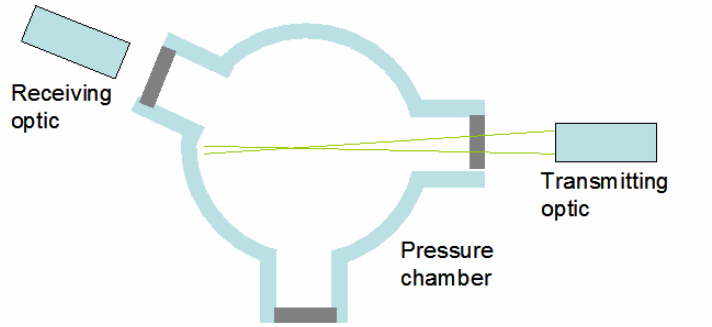

Figure 2.4: Configuration of the PDA optics with the pressure chamber

Table 2.1: Parameters of the transmitting and receiving optics

Transmitting optic		
Beam system	U1	U2
No. of fringes	56	56
Fringes spacing (µm)	5.151	4.886
Beam half angle (deg)	2.862	2.862
Probe volume-dx (mm)	0.292	0.276
Probe volume-dy (mm)	0.291	0.276
Probe volume-dz (mm)	5.830	5.530
Wavelength (nm)	514.5	488
Focal length (mm)	600	600
Beam diameter (mm)	1.35	1.35
Expander ratio	1	1
Beam spacing (mm)	60	60
PDA receiver		
Receiver type	Dual PDA	
Scattering angle (deg)	30	
Receiver focal length (mm)	400	
Expander ratio	1	
Fringes direction	U-/V-	
Scattering mode	Refraction	
Mask (Aperture)	Mask A	
Max. diameter (µm)	294.685	
Eff. slit width (mm)	0.320	

While drop velocity measurements depend strictly on the frequency of the intensity variation of scattered light due to droplet movement and fringe interactions, accurate droplet diameter

measurements depend on the spatial frequency of the scattered light. In essence, the scattered fringe spacing, or phase shift, is determined by the size of the scattering droplet, while the frequency of the scattered light is a measure of the droplet velocity. For this reason, at least two photo detectors are needed to measure droplet diameters. The PDA system used here contains four detectors, allowing two independent measurements to be made simultaneously for the reason of spherical validation. Spherical validation of 15% and 30% are used for the spray characterization and the spray impact experiments respectively. Further details of the PDA system parameters are shown in table 2.1. More details about the PDA technique can be found in [27,28].

2.3 Particle Image Velocimetry (PIV)

PIV is a non-intrusive, whole field, laser optical measurement technique for flow velocity. A pulsed laser (New Wave Solo Nd:YAG), with optical attenuator designed to work at a wavelength of 532 nm is used to illuminate the measurement plane for PIV measurements. The laser beam passes a cylindrical lens with 6 mm diameter and diverges after the lens with 14° to produce a 1.2 mm thick laser sheet. The laser power is 2 x 120 mJ at 532 nm wavelength. The images are captured using a CCD camera (SensiCam) with 1280 by 1024 pixels and an equal number of storage cells at 90° angle. The captured images are processed by Dantec Dynamics FlowManager software, using an interrogation area of 32x32 pixels and an overlap of 50%. The liquid droplets in the spray are used as tracer particles to measure the velocity of the liquid phase, whereas aerosol oil droplets are used to mark the gas phase. These tracer particles are generated by the "home-made" aerosole generator. The generator is described in section 2.5.

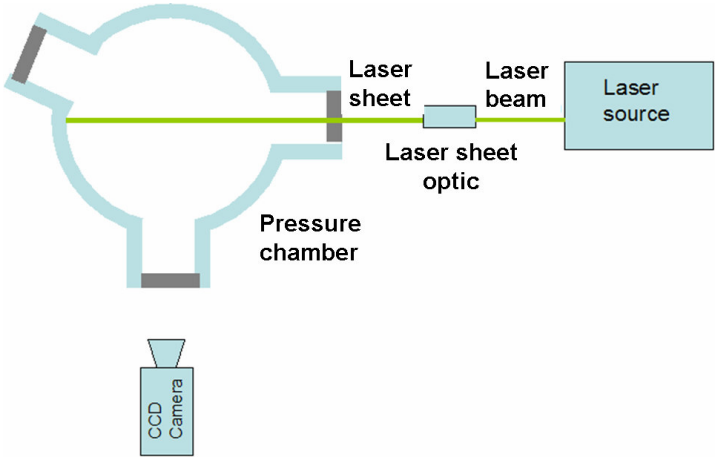

Figure 2.5: Schematic of the PIV system with the pressure chamber

2.4 Time resolved imaging technique

Time resolved images are captured using a high-speed video camera (PHOTRON FASTCAM-Ultima 512 32K) for the spray visualization experiments and for the spray impact set of experiment a (PHOTRON FASTCAM-SA1 650K) camera is used.

To estimate the spray frequency by processing the high-speed video camera images, the images are captured at 30º as shown in figure 2.6. The spray is illuminated by a continuous laser sheet of Argon-Ion laser. The frame rate is varied between 2 kHz and 8 kHz to capture frequencies between 0.2 and 3.2 kHz.

The images that are used for whole field visualization and the near nozzle region are captured at 54 k frames per second with a shutter time of 1/297000 sec.

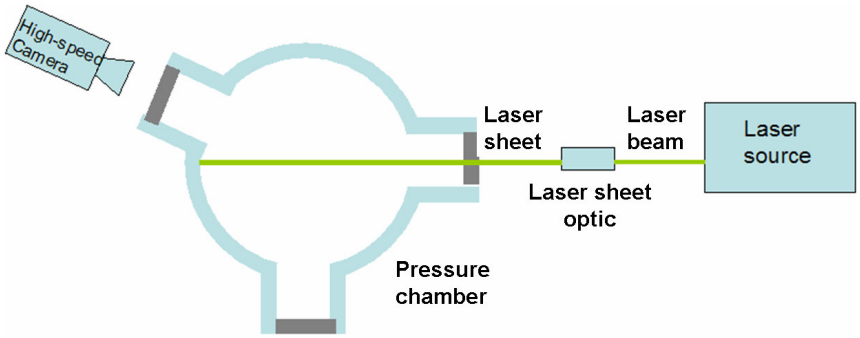

Figure 2.6: Schematic of the high-speed camera with the pressure chamber for the spray visualization measurements

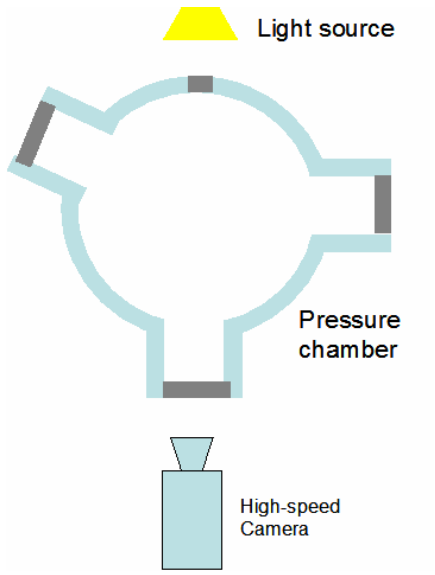

Figure 2.7: Schematic of the high-speed camera with the pressure chamber for the spray impact experiments

A 2 kW light source is used as shown in figure 2.7 with a diffuser sheet between the light source and the spray to uniformly illuminate the background.

2.5 Aerosol generator for the airflow measurements

In order to measure the airflow in the near nozzle region using optical measurement techniques like laser Doppler or PIV, the flow must be marked with tracer particles. There are no available industrial aerosol generators able to create small aerosol particles in a high pressure flow above 10 bar. Therefore, a custom-built aerosol generator has been designed and built with a pressure range of up to 40 bar. The generator consists of the following components and is schematically shown in figure 2.8.

- pressure reducer connected with the high-pressure air line;
- first chamber where the primary spray is created;
- second chamber where the primary spray droplets are separated on an impacting plate and the large inertial drops are deposited and removed from the flow.

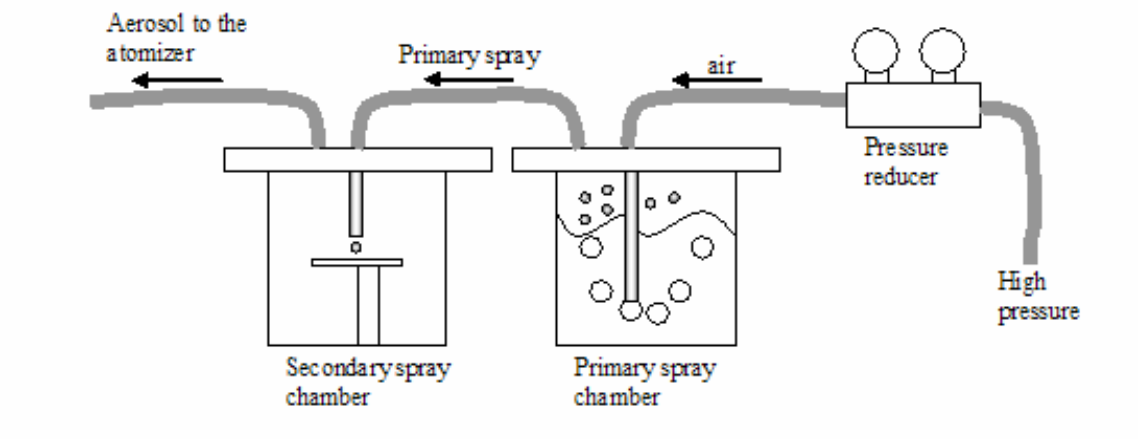

Figure 2.8: Schematic of the high-pressure aerosol generator

The aerosol generator is able to produce small droplets at elevated pressure conditions, but at high airflow rates , the aerosol oil starts to reach the atomizer exit as ligaments due to the high impact velocity on the inner surface of the atomizer. This leads to relatively large tracer particles, which don't follow the airflow due to their high Stokes number. In this case, the qualitative and quantitative analysis of velocity profiles reveals considerable and unjustified diviation from the LDA results, therefore, part of the results that are obtained for the gas-phase velocity is not accepted.

3. Spray generated by the MTU airblast atomizer used in this work

Generation of fine drops with high surface-to-volume ratio is required to ensure good combustion in gas turbines and diesel engines. Various types of airblast atomizers have been designed and tested to match different applications. The most widely used type in aero engines and gas turbines is the airblast atomizer, by which the liquid phase is introduced in the form of a liquid film that breaks up due to the shear forces at the liquid-gas interfaces and due to spray impact onto a pre-filmer.

In order to characterize the atomization process and the features associated with the spray propagation it is important to investigate the phenomena qualitatively through their visualization. In this chapter, a report of the results of visualization of the spray generated by the MTU airblast atomizer described in section 2.1 is presented.

3.1 Airblast spray

In order to better understand the investigated spray and the process of its creation, a series of measurements using the PIV technique and time-resolved high-speed video imaging has been performed. An example of the PIV measurements is shown in figure 3.1.

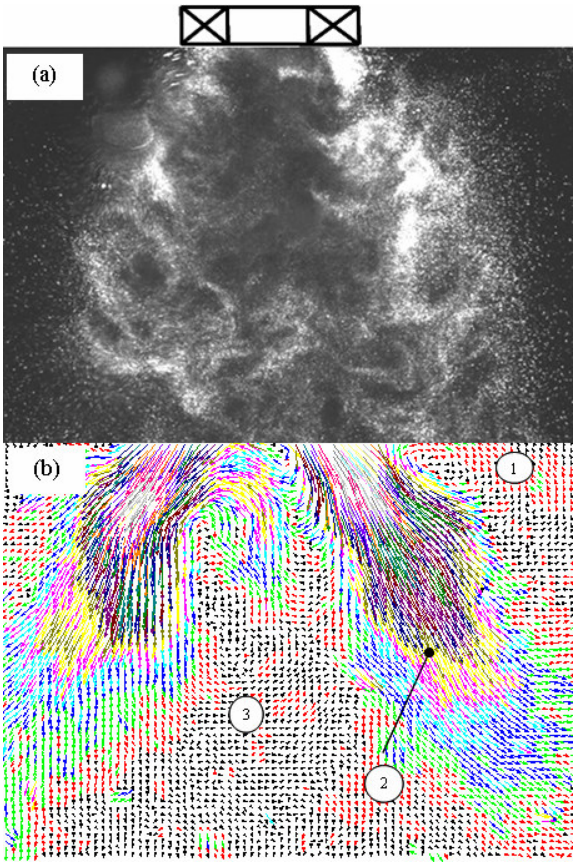

Figure 3.1: (a) Spray image using the planar laser sheet, (b) vector plot of spray using PIV instrument (water flow rate: 2.66 l/hr, air flow rate: 20 SCMH, chamber pressure: 1bar).

In figure 3.1a the spray is illuminated by a planar laser sheet. An example of an average velocity field obtained using the PIV technique is shown in figure 3.1b. In this figure the length and the color of the arrows correspond to the velocity magnitude. The spray droplets have been used as markers for the PIV, therefore, only the average spray velocity has been measured. No explicit information about the air flow can be obtained from these measurements.

Qualitatively, three main regions can be immediately recognized:

- outer region 1 of relatively small droplet velocity;
- main region 2 of relatively high droplet velocity;
- inner region 3 near the axis.

This flow is non-stationary and turbulent. Some vortex structures are often created at the boundary between regions 2 and 3, leading to the typical fir-tree-like instantaneous shapes of region 3.

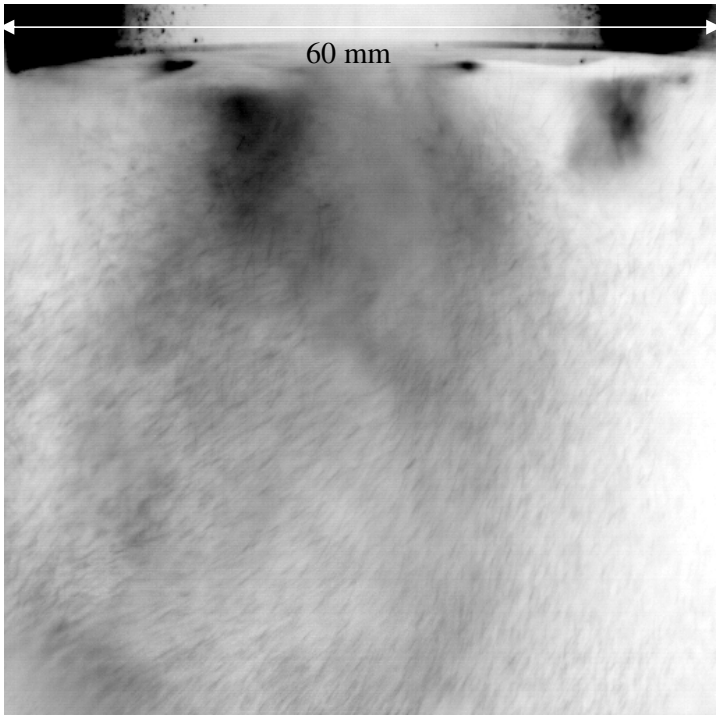

Figure 3.2: Image of airblast spray generated with high-speed video camera (water flow rate: 2.66 l/hr, air flow rate: 20 SCMH, chamber pressure: 1bar, frame rate of 2kHz and shutter time of 1s.)

The motion of single droplets can be clearly seen on the images of spray captured by the high-speed video system. It could be expected that the motion of the relatively large water drops is inertia dominated. However, Straight drop trajectories, typical of inertial drops are not observed. In fact the droplets followed the swirl air flow. In the image in figure 3.2 the shutter time is relatively long such that each drop is shown as a short line directed along the instantaneous drop trajectory. Even in the single image in figure 3.2 the spiral drop trajectories can be recognized. It is also clear that this phenomenon of capturing of droplets by a swirl airflow can only be observed for very large values of the air-to-liquid mass ratio, typical of the present experimental conditions. In this case the momentum of the liquid fraction is small in comparison with the momentum of the air flow.

Using larger magnification, higher frame rates and shorter shutter times at different airflow rates, the high-speed video images provide information concerning the liquid forms that leave the atomizer. In figure 3.3, the airflow rate is varied between 10, 20 and 30 SCMH.

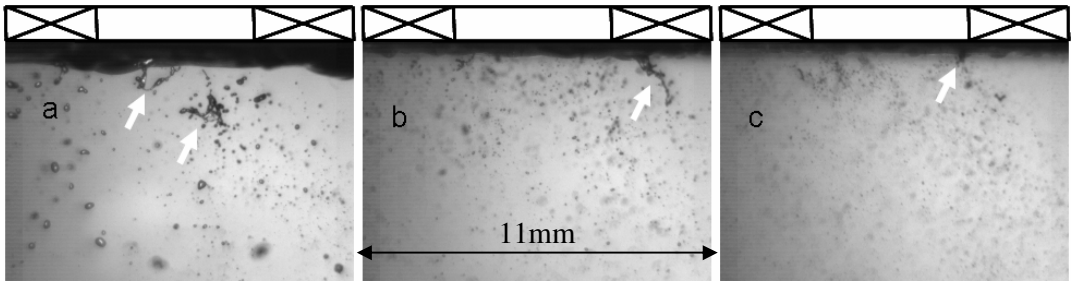

Figure 3.3: Single frames of high-speed video images of airblast spray at the exit of the atomizer at chamber pressure of 1 bar, water flow rate of 3 l/hr and airflow rate of; a) 10 SCMH, b) 20 SCMH, c) 30 SCMH. Frame rate is 54 kHz, shutter time is 1/297000 s

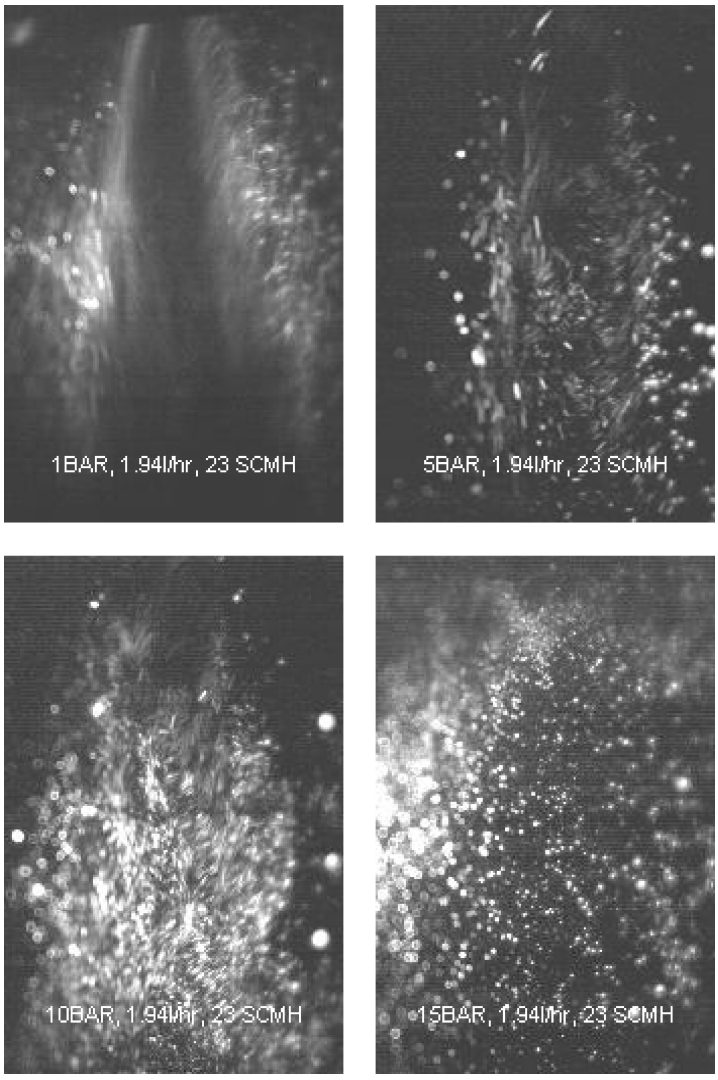

Figure 3.4: Single frames of high-speed video images for airblast spray (liquid phase) at different chamber pressures. Liquid flow rate 2.66 l/h, air flow rate 20 SCMH, frame rate of 2kHz and shutter time of 1 s.

At lower airflow rates, the liquid leaves the atomizer in the form of ligaments and large droplets as pictured in figure 3.3a. The ligaments start to follow the swirl path and become smaller when the airflow rate is increased as shown in figures 3.3b and c.

The effect of increasing chamber pressure while keeping a constant airflow rate can be qualitatively captured by the high-speed video imaging. In figure 3.4, the single frames present the shape of the entire spray at a) 1, b) 5, c) 10 and d) 15 bars. It is shown that the hollow-cone shape of the airblast spray changes as the chamber pressure increases. These images have been taken at 30° angle as per the setup shown in figure 2.6.

3.2 Gas phase

The air flow generated by the atomizer is visualized using the tracers introduced by the aerosol generator. In fig. 3.5 the aerosol flow is illuminated by a planar laser sheet and the images are captured by a high-speed video camera. Single images show different details of the gas phase flow such as; spray cone, and typical vortex structure.

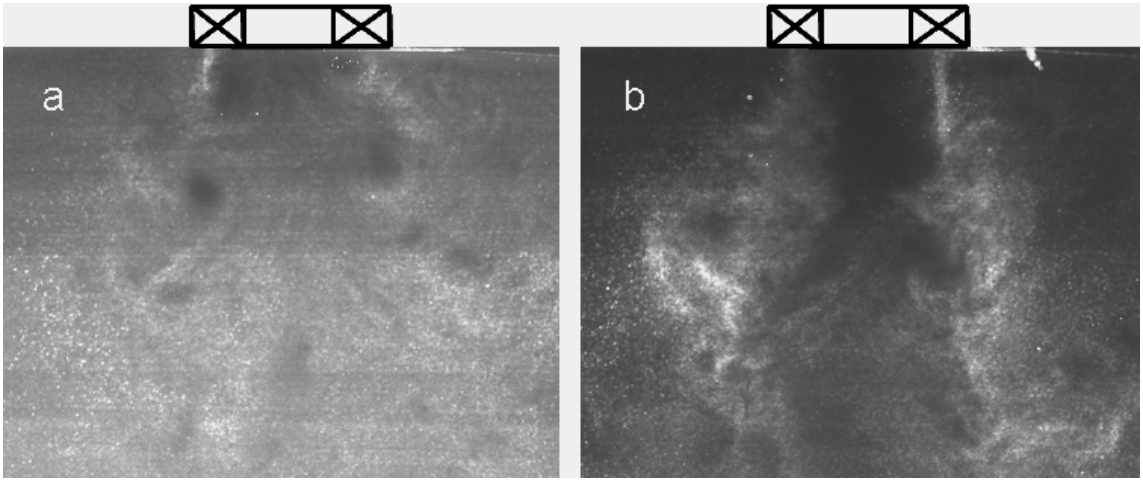

Figure 3.5: Air image using planar laser sheet and oil as seeding particles at chamber pressure of 1 bar and air-mass flow rate of; a) 20SCMH, b) 60SCMH

The vortex structure can be easily seen in figure 3.5a. This phenomenon is known as the Precessing Vortex Core (PVC). The PVC appears to be a mechanism of the rapid transport of fluid from the wall opposite the exit of the swirl device to the downstream end of the Reverse Flow Zone RFZ, or recirculation zone. In figure 3.5b the air entrainment phenomena is observed. In this work, the high-speed images are used to estimate the aerodynamic frequency of the gas phase as discussed later in chapter 4 of this thesis.

.

3.3 Pressure swirl (primary) spray

It is interesting to qualitatively compare the airblast spray (the output from the atomization process) shown in figures 3.1 and 3.2 with the primary spray generated by the pressure swirl nozzle (the input spray to atomizer) shown in figure 3.6. In figure 3.6 these sprays are shown at various ambient pressures while the water flux is constant. The cone angle of the spray slightly decreases when the ambient pressure is higher, and the spray becomes denser. Moreover, some periodic moving structures appear in the spray at a pressure larger than 5 bars. The average spray velocity reduces at higher ambient pressures due to increasing the drag force. This effect can also explain the higher dispersion of the spray region leading to the motion of drops of the main spray region. At high ambient pressures many relatively slow drops can be seen at the spray periphery under chamber pressure of 15 and 20 bars (Figure 3.6). The variation of the primary spray parameters influences the thin film that is generated on the pre-filmer, which is the source of all droplets in the airblast spray.

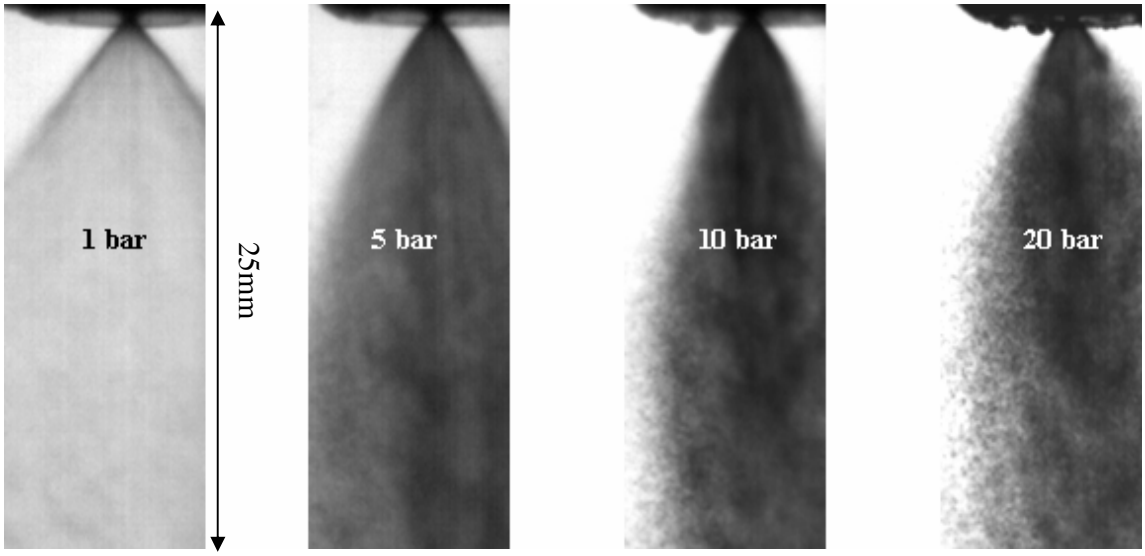

Figure 3.6: Primary spray at various ambient pressures. The liquid volume flux is 2.66 l/hr.

4. Aerodynamic instability of spray generated by an airblast atomizer under steady and forced-oscillating pressure conditions

The geometry of the MTU airblast atomizer allows the gas-phase to create a swirl path. This swirl movement of the air enhances the mixing process between the liquid and the gas phases by gaining an azimuthal velocity component as well as increasing the volume-mass ratio of the mixture. The main application field of such atomizers is in industrial combustors and gas turbines [29]. However, they can also be effectively used in the atomization of complex, non-Newtonian fluids [30-31]. Recently, attention has turned to the possibility of designing airblast atomizers which are able to control the parameters of the generated sprays [32-33] or to suppress the combustion instabilities [34-35]. Furthermore, gas turbine combustion depends on the control of the local air/fuel ratio. Swirl is commonly used to stabilize turbulent flames in regions of low flow velocities. As combustion is driven closer to the extinction limits, it is important to understand not only the mean flow field but also the flow field dynamics [35].

Conical swirl sprays generate natural oscillations which are frequently explained by the appearance of a so-called precessing vortex core (PVC). The precessing vortex core is responsible for establishing the near-field aerodynamic characteristics. They also influence the flame instability and the fuel/air mixing [36]. The velocity oscillations of air and fuel particles in gas turbine applications can lead to the reduction of the combustion effectiveness, increased emissions and in worst case they can destroy the gas turbines.

The main subject of the study presented in this chapter is the investigation of the unsteady characteristics of spray generated by an airblast swirl generator over a co-current variation of air pressure and mass flow with an independent variation of air mass flux and liquid mass flux under isothermal conditions.

This study is focused on the estimation of the typical frequency of the spray oscillations. This unstationary feature of the spray propagation is rather important for many industrial applications, mainly for the design and optimization of the combustion chambers. The values of the typical spray frequency are significant since they can be related to the onset of the thermoacoustic oscillations leading to the appearance of the combustion instabilities and even further destruction of the combustor.

The instationary phenomena involved in spray propagation, spray fluctuations and combustion are extremely complicated. Therefore, since these phenomena cannot be easily

scaled, the usual research approach is based on the achievement of the typical parameters of laboratory sprays generated by industrial atomizers in the ranges relevant to the practical operating conditions. Such studies must be carefully repeated for each geometry of the atomizer and combustor, and must cover the entire range of the operating conditions. It is therefore obvious that the modeling of even one "simplest" element of this process, which is valid in a wide range of parameters, can be very valuable.

In the present study the research is focused only on the onset of the natural oscillations of the isothermal swirling spray. These fluctuations in airblast sprays appear as the result of the instability which has the form of vortices that leave the atomizer in a swirl motion.

Spray fluctuations at various chamber pressures are measured using two techniques, namely; proper orthogonal decomposition of time-resolved images and fuzzy slotting technique of laser Doppler velocity data. The estimated frequencies obtained using the both techniques match each other closely. This result indicates that the local spray frequency (measured using the LDA technique) is equal to the frequency of the fluctuations of the spray shape (observed using the high-speed video system).

The spray frequency is measured in a wide range of operating conditions: at various ambient pressures, volumetric fluxes of the fluid and air velocities. Two atomizer sizes are used in the experiments keeping its form constant: full scale nozzle and the scaled model. The scaled atomizer is used to study the airflow in the mixing chamber without spray.

The measurements are performed at two spray propagation modes: at lower ambient pressures and higher air velocities the typical hollow-cone airblast spray is created, whereas at the elevated ambient pressures and lower air velocities the spray breaks up and propagates in almost radial direction along the upper wall of the chamber where the atomizer is installed. At these conditions the droplets can be so large, that they miss the first turn of the gas flow around the recirculation zone and similarity to the other conditions at higher air velocities can be lost.

Nevertheless, scaling analysis of the spray frequency, described in section 4.3, demonstrates that it depends only on the average air velocity at the nozzle outlet and on the atomizer geometry. The main result of this study is that this scaling can be successfully applied to all the sprays or mixing flows, independent of the nozzle size, ambient pressure, volumetric flux of the liquid or even of the spray propagation mode. This result can thus be directly applied to industrial sprays operating at the real combustion chamber conditions.

The next topic considered in this chapter is the description of the forced spray oscillations generated by the fluctuations of the ambient pressure in the chamber. One surprising result is

that the pressure oscillations of even relatively small amplitude lead to significant change in the spray shape and its strong fluctuations with the same frequency.

4.1 Data analysis techniques

4.1.1 Fuzzy Slotting Technique (*FST*):

To analyze the characteristic frequencies from randomly sampled laser-Doppler data the fuzzy-slotting technique suggested by [37-39] has been applied to the acquired data for the droplet axial velocity and the arrival time acquired by the phase Doppler instrument. The basic idea is to estimate the auto-correlation function *(ACF)* R_{11} by correlating the data pairwise and prorate the correlation value $u_j u_i$ in the best fitting slot of equidistant arrival time difference $k\Delta\tau$ in comparison to the measured inter-arrival time $\Delta t = t_i - t_j$.

$$(k-0.5)\Delta\tau < \Delta\tau < (k+0.5)\Delta\tau \tag{4.1}$$

$$R(k\Delta\tau) = \frac{\sum u_j u_{i\,(k\Delta\tau)}}{H_{(k\Delta\tau)}} \tag{4.2}$$

In equation (2) $\sum u_j u_{i\,(k\Delta\tau)}$ is the sum of all correlation values and $H_{(k\Delta\tau)}$ is the number of correlations falling into the k^{th} slot. The power spectra density (PSD) E_{11} can be estimated using the Fourier transformation of the auto-correlation function.

4.1.2 Proper Orthogonal Decomposition (POD):

It was suggested by [40] that the coherent structure in a turbulent flow could be identified by the representation of the flow that has the largest projection onto the flow, and the coherent structures are the primary eigenmodes that make significant contributions to the turbulent kinetic energy. [41] implemented the POD analysis to reveal coherent flow structures from PIV data transferring the original dataset into a new base (modes). [20,42] showed that this technique is also suitable to analyze the intensity variations or combinations of velocity and intensity data.

Using the POD on the time-resolved high-speed images, the intensity of every image $\psi(t)$ could be reconstructed using the new Modes $\phi^{(m)}$ and corresponding coefficients $a^{(m)}(t)$.

$$\psi(t) = \overline{\psi} + \sum_{m=1}^{N} a^{(m)}(t)\phi^{(m)} \tag{4.3}$$

To identify these Modes, the eigenvalue equation (4.4) has to be solved.

$$(R - \lambda I)\phi = 0 \tag{4.4}$$

Here I represents the unit matrix and R the averaged covariance matrix of the intensities as shown in equation (5).

$$R = \overline{(\psi - \overline{\psi}).(\psi - \overline{\psi})^T} \tag{4.5}$$

The eigenvalue λ can be interpreted as energy of the fluctuations, so dominant characteristic fluctuations with high energy can be found by the first mode. The time-resolved series of coefficients of equation (4.3) can be analysed for dominant frequencies and characteristic phase relations deriving the power spectra density E_{mm} from the coefficients $a^{(m)}(t)$ and $a^{(n)}(t)$ of Modes m and n.

4.2 Measurements of the frequencies of spray fluctuations

Both PDA and PIV measurements have been used to investigate the droplet size distribution in an airblast spray (liquid phase) and the velocity profiles for both gas and liquid phases.

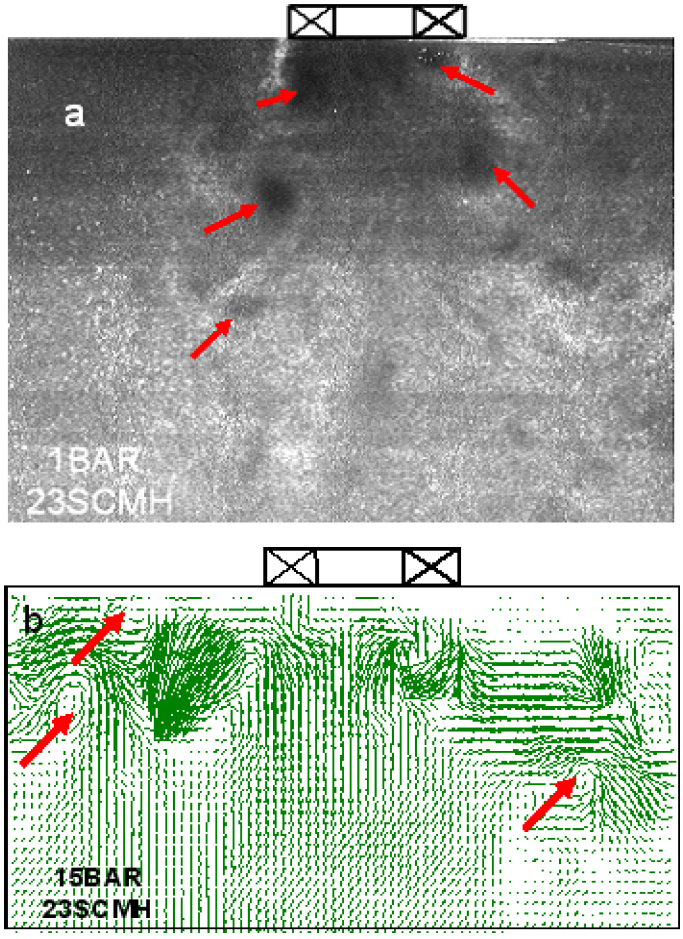

Figure 4.1: a) PIV image of gas phase at 1 bar pressure and 23 SCMH (b) Velocity vectors at 15 bar pressure and 23 SCMH.

The resulting velocity profiles show an asymmetrical distribution with respect to the spray axis. These results can be related to the vortex structures that are formed within the spray, Figure 4.1.

It is shown in both figures 4.1a and 4.1b, that the vortex structure can be captured at low and high pressures. The Fuzzy Slotting Technique analysis has been applied to the data (200k samples) for the axial velocity component of the drops in the spray. The autocorrelation function R_{11} and the power spectral density E_{11} are computed for different chamber pressures, as shown exemplarily in figure 4.2. At 1 bar chamber pressure, 20 SCMH airflow rate and 1.92 l/h water flow rate, the spray has a frequency of 2960 Hz. This frequency decreases to 1090 Hz at 3 bars and 680 Hz at 5 bars.

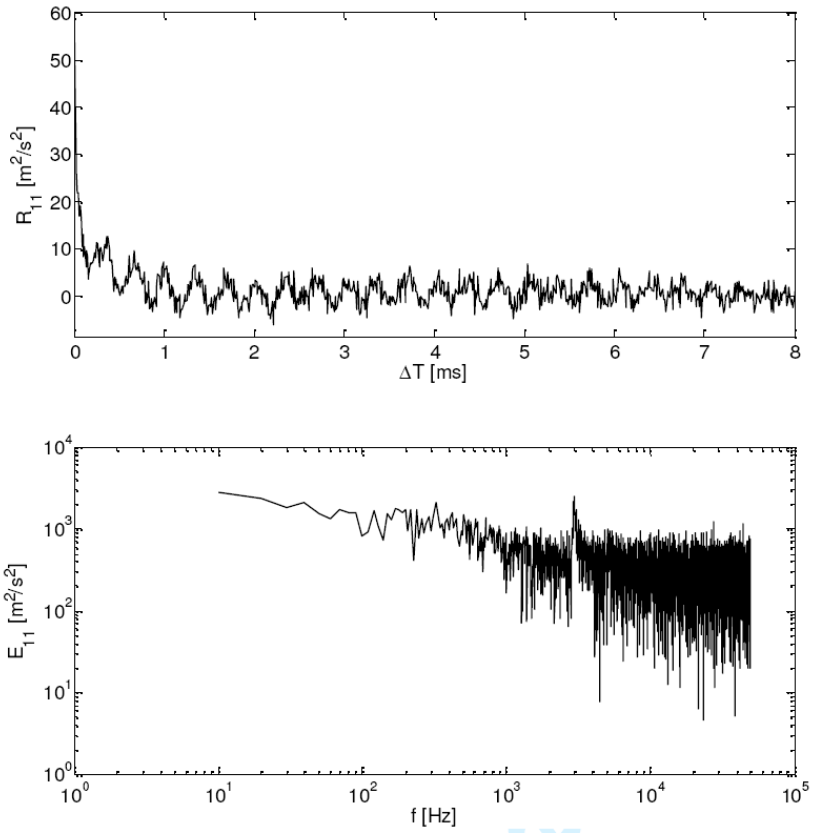

Figure 4.2: Autocorrelation function R_{11} and power spectral density E_{11} of the phase Doppler data at a chamber pressure of 1 bar and airflow rate of 20 SCMH

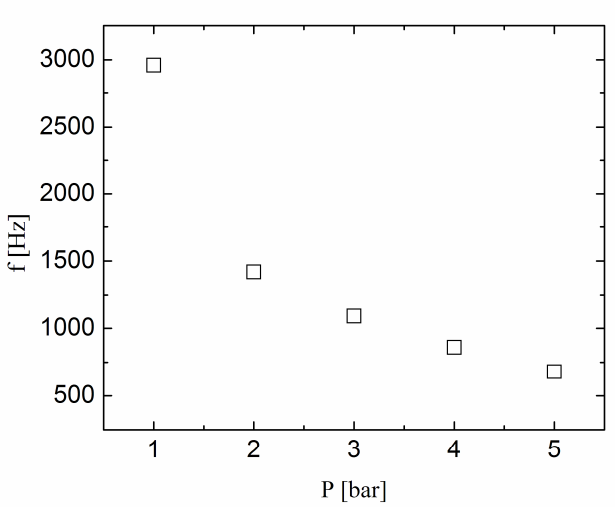

Figure 4.3: Frequency at 20SCMH airflow rate and variable chamber pressures determined from the phase Doppler velocity measurements

The processing of the phase Doppler data revealed a strong periodic fluctuation of the axial velocity component at frequencies inversely proportional to the chamber pressure, indicating a helix vortex which is typical of a swirl spray (Figure4.3).

The phase Doppler technique provides also information about the distribution of the drop diameters. However, no evidence has been found that the value of the drop diameter also oscillates or that there is any diameter dependence on the phase of the spray oscillations.

Conducting phase Doppler measurements at high liquid flow rates becomes problematic because the optical accesses become wetted, which reduces the data rate and the validation ratio. The use of a high-speed video camera then helps to obtain enough images that contain satisfactory information about the oscillations of the spray shape. However, it is not a priori clear whether the frequency of the local velocity fluctuations (measured using the phase Doppler instrument) will coincide with the global frequency of fluctuations of the spray shape, as observed by the high-speed camera.

Therefore, an initial set of high-speed video camera images has been performed at the same conditions to check the validity of the POD analysis and the resulting frequencies. The results of this comparison are presented in figure 4.4 indicating good agreement between the frequencies determined using a spectral analysis of the velocity fluctuations and the POD analysis of the high-speed images.

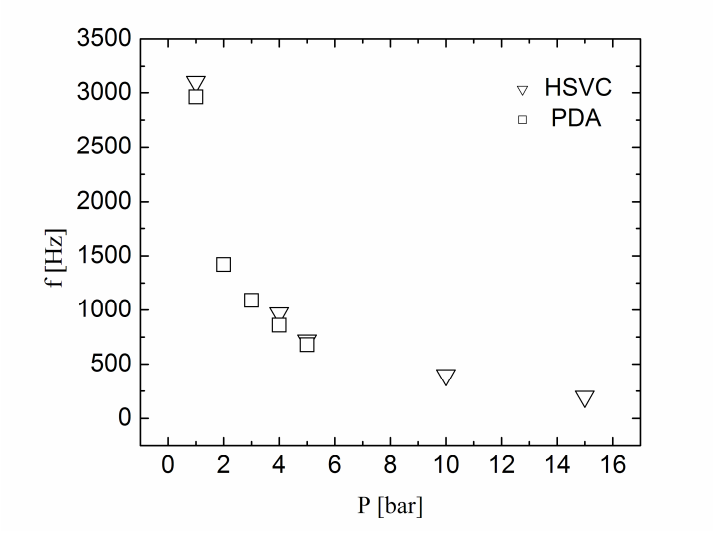

Figure 4.4: Frequency at 20SCMH airflow rate and variable chamber pressures determined from the phase Doppler velocity measurements and the high-speed video images

The POD analysis of time-resolved images provides also the possibility of separating the different modes of oscillation. In Figure 4.5 for example, the POD is used to separate modes 1 and 2, which in this case, have the maximum energy.

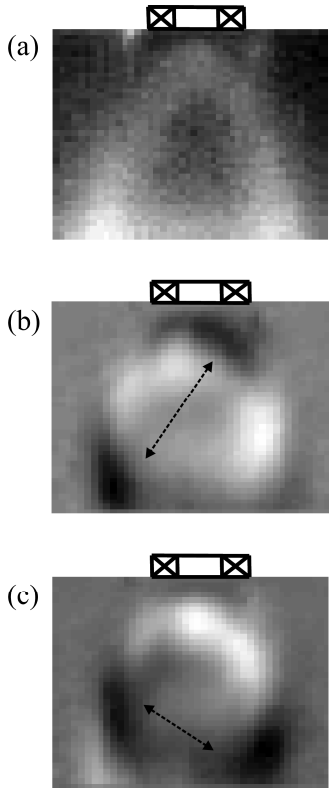

Figure 4.5: POD obtained from the analysis of the spray images captured by the high-speed video system for 1bar and 20 SCMH case: Mode 0 (a), Mode 1 (b), Mode 2 (c). The arrows show the similar vortex structures.

The spectra of these Modes could again reveal a distinct frequency which matches the corresponding frequency of the Phase Doppler velocity measurements. The cross-correlation function of Modes 1 and 2 shows a phase-shift of 90° Figure 4.6 indicating a downstream translation of the vortex structures. In figure 4.5 these structures are marked by dashed arrows.

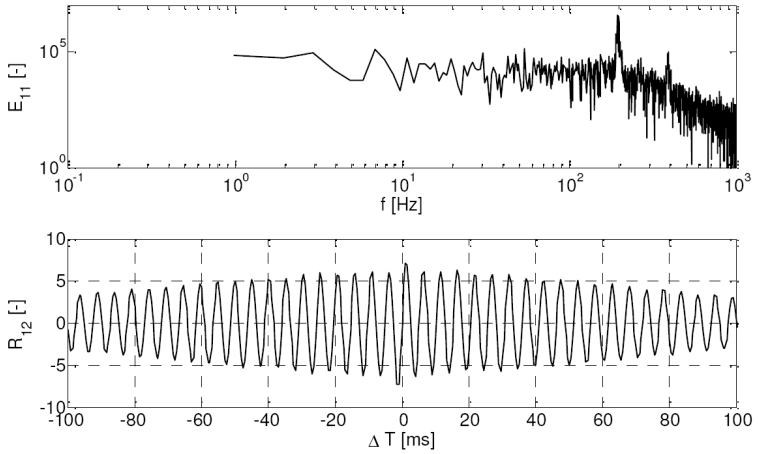

Figure 4.6: Power spectra density and cross-correlation-function of Modes 1 and 2 at an ambient pressure of 15 bars

Furthermore, the effect of the gas-phase flow rate on the spray frequency has been investigated. It is expected that the spray frequency increases when increasing the gas flow rate, which leads to the need of higher frame rates. Since the available high speed video camera is limited by 32000 fps and at such high frame rates, the field of view is very small, a chamber pressure of 10 bar is fixed while studying the effect of the gas-phase flow rate on the spray frequency, which minimize the needed frame rates and leads to a larger field of view. Volumetric flow rates of 20, 30 and 58 SCMH at 1.94 l/h water flow rate are used at a chamber pressure of 10 bar. As shown in figure 4.7, the spray oscillation frequency increases when increasing the gas-phase flow rate.

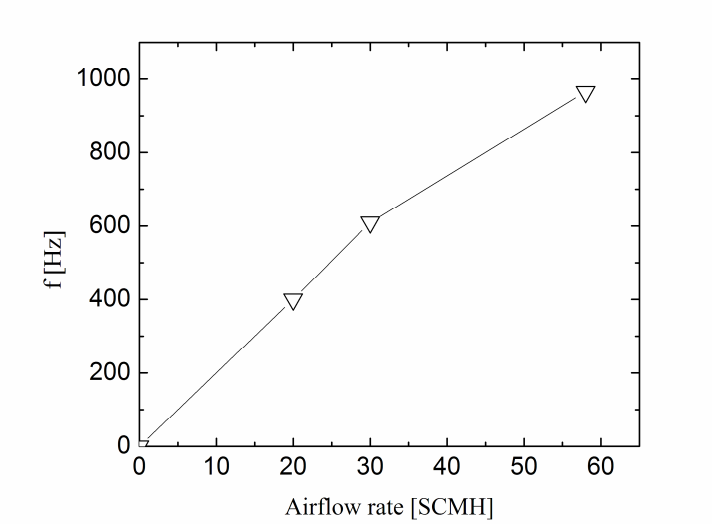

Figure 4.7: Spray frequency as a function of the air flow rate at 10 bars chamber pressure

To study the effect of liquid-phase flow rate on the spray frequency, flow rates of 1.92, 2.54 and 3.24 l/h are used at 20 SCMH gas-phase flow rate and 4 bar chamber pressure. The POD analysis shows that the spray frequency is independent of the liquid-phase flow rate (figure 4.8).

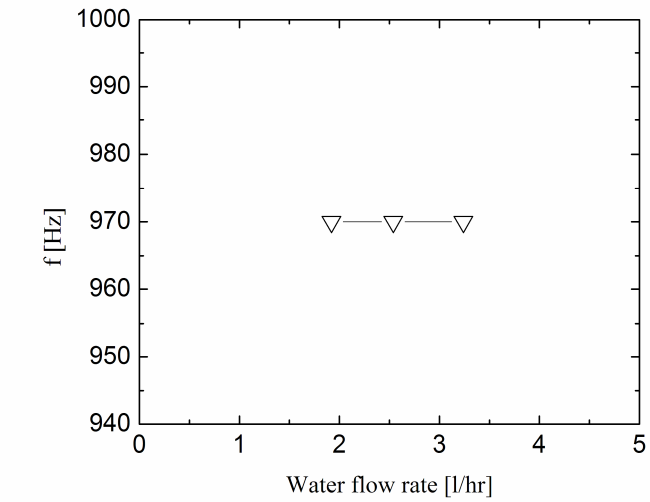

Figure 4.8: Spray frequency as a function of the water flow rate at 4 bars chamber pressure.

4.3 Scaling analysis of spray oscillations

In order to model the frequency of spray oscillations it is necessary first to consider the possible factors influencing the phenomena. In our case the liquid-to-air mass flow ratio is very small. Therefore, the influence of the momentum of the liquid phase on the spray dynamics is negligibly small. This assumption is confirmed by the results shown in figure 4.8.

Since the airflow velocity is rather high, the viscosity is also not a significant factor. The main parameters determining the spray frequency are therefore, the typical air velocity and the geometry of the atomizer. The characteristic frequency of spray fluctuations can be thus estimated using equation (4.6)

$$f_c = \frac{\overline{U}_\varphi^*}{\pi D} \tag{4.6}$$

The characteristic tangential velocity $\overline{U}_\varphi^*$ is estimated from the axial velocity $\overline{U}_{ax}$ using the swirl number S (equation (4.7)) which is defined by equation (4.8).

$$\overline{U}_\varphi^* = S\overline{U}_{ax} \text{ with } \overline{U}_{ax} = \frac{4\dot{m}}{\rho\pi D^2} \tag{4.7}$$

$$S = \frac{\int_0^{r_0} U_{ax}(r)U_\varphi(r)r^2 dr}{r_0 \int_0^{r_0} U_{ax}^2(r)dr} \tag{4.8}$$

where $\dot{m}$ is the mass flow rate of the air, U_{ax} and U_φ are the averaged axial and tangential velocities of the air at the outlet, D and S are the averaged diameter and the swirl number, respectively. The magnitude of the ambient pressure does not appear explicitly in the expression (4.7). Nevertheless, the ambient pressure (or more precisely the air density) determines the value of the averaged air velocity if the mass flow rate is given.

Table 4.1 shows the different settings and the calculated frequencies which is plotted against the measured frequency in figure 4.9. Hereby the data of measurements with pure air performed by [6] in an isobaric mixing chamber using the same type of swirl nozzles scaled up by the factor of 2 was added for comparison. It can be seen, that all data points can be approximated using a linear regression. This result supports our assumption that the spray frequency is proportional to the characteristic frequency determined in equation 4.6. It also demonstrates that both techniques used to estimate spray oscillation frequency provide very similar results.

Table 4.1: Characteristic frequencies f_c at various operational conditions

$D[mm]$	$p[bar]$	$\overline{U}_{ax}[m/s]$	$f_c[Hz]$
11.6	1	52.05	1422
11.6	2	26.03	711
11.6	3	17.35	474
11.6	4	13.01	355
11.6	5	10.41	284
11.6	5	15.62	427
11.6	5	23.42	640
11.6	10	5.21	142
11.6	10	7.81	213
11.6	10	15.10	412
11.6	15	3.47	95
23.2	1	46.85	640
23.2	1	70.27	960
23.2	1	93.70	1280
23.2	1	117.27	1600
23.2	1	140.55	1919

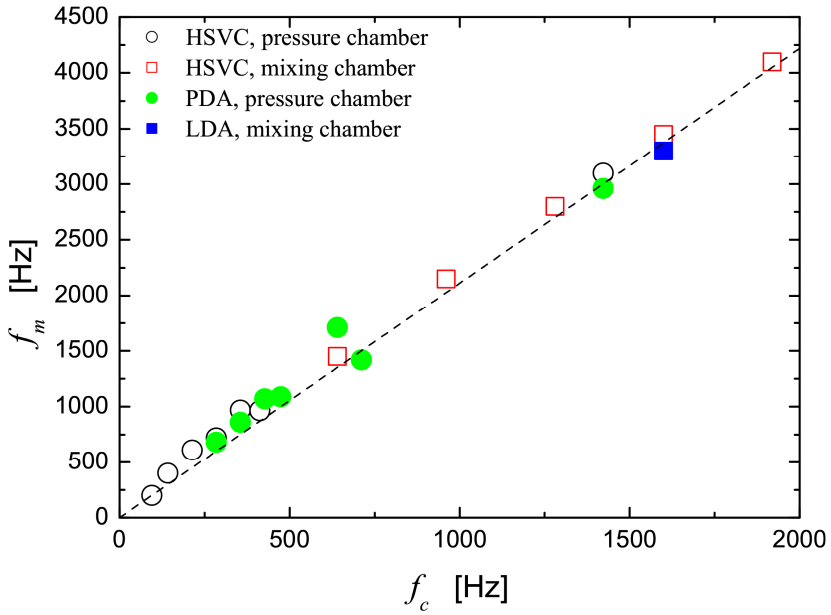

Figure 4.9: Measured frequency f_m as a function of the calculated characteristic frequency f_c

Alternatively a specific Strouhal number of the nozzle can be introduced:

$$St = \frac{f_m D}{\overline{U}_{ax}} \tag{4.9}$$

Figure 4.10 shows this Strouhal number for all measurements.

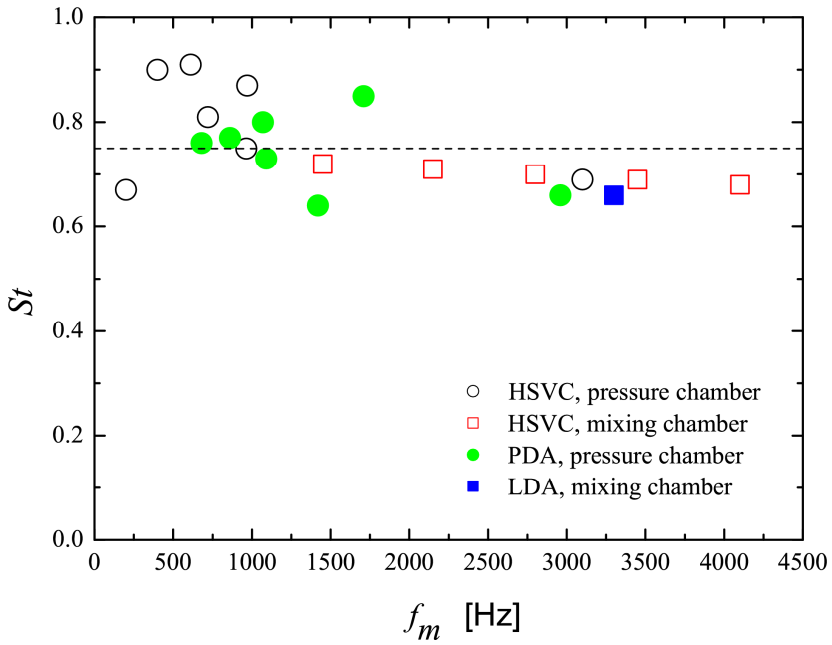

Figure 4.10: Strouhal number for the measured data

The measurements show an average Strouhal number of $St = 0.75 \pm 0.8$. It is obvious that the value of the Strouhal number depends on the geometry of the atomizer. However, once determined for a specific atomizer it should be valid for a range of ambient pressures and airflow rates.

4.4 Forced-pressure oscillations

The aim of this part is to experimentally investigate the sensitivity of spray generated by an airblast atomizer to ambient pressure fluctuations. The pressure fluctuations are meant to emulate conditions occurring due to combustion instabilities, albeit without combustion or droplet evaporation. The study concentrates primarily on the behavior of liquid phase as a function of ambient pressure. The important factor is the pressure dependency of spray behavior.

The existing experimental setup is modified by installing a pulsating valve (pulsator) at the exhaust side of the pressure chamber as shown in figure 4.11. The pulsating valve consists of two main parts; rotating cylinder (marked as 1 in figure 4.11) and the A/C motor (marked as 2 in figure 4.11). The rotating cylinder has 4 circular openings. These openings generate on-off effect. This on-off effect imparts pressure oscillations onto the ambient chamber pressure. The valve is driven and controlled by the A/C motor that controls the frequency of the rotating cylinder, which dependently generates the oscillations in the chamber. The system generates frequencies up to 400 Hz.

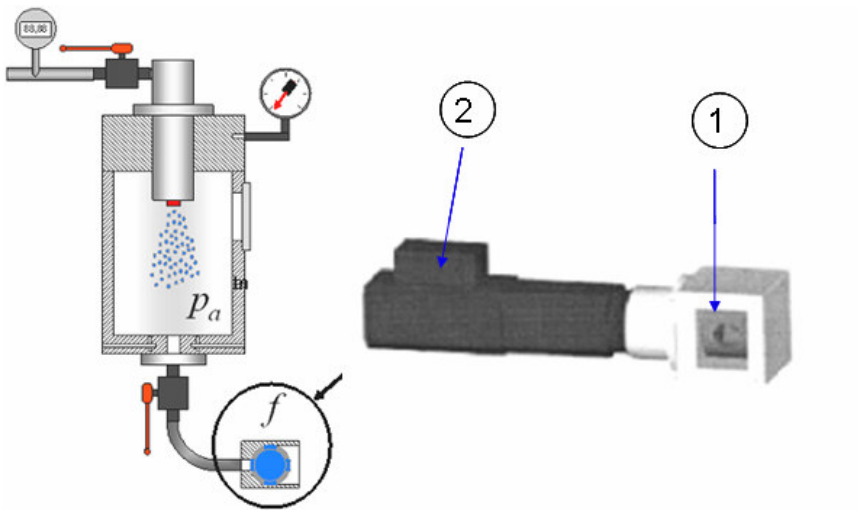

Figure 4.11: Schematic drawing of the pressure chamber and the pulsator.

4.4.1 Measurements of pressure oscillation magnitude

The pressure oscillation amplitude is a function of the chamber pressure and the pulsator frequency. The values of the instantaneous ambient pressure is measured using a set of the dynamic pressure sensors installed in the wall of the pressure chamber. The results of the pressure measurements are shown in figure 4.12 while the parameters of the experiments reported in this work are listed in table 4.2. Two graphs are shown in figure 4.12. The left graph shows one example of the pressure fluctuations inside the chamber as a function of time. The frequency of the pressure oscillations coincides with the frequency of the pulsator. The right graph in figure 4.12 shows the dependence of the amplitude of the pressure oscillations as a function of the average pressure in the chamber at various frequencies of the pulsator.

It should be noted that the amplitude of the spray oscillations is rather small. Although some change of ambient pressure at stationary conditions would lead to only very minor changes of

the main spray parameters, it will be shown below that such small pressure fluctuations lead to the significant changes in the spray behavior which indicates the importance of the instationary effects on the spray dynamics.

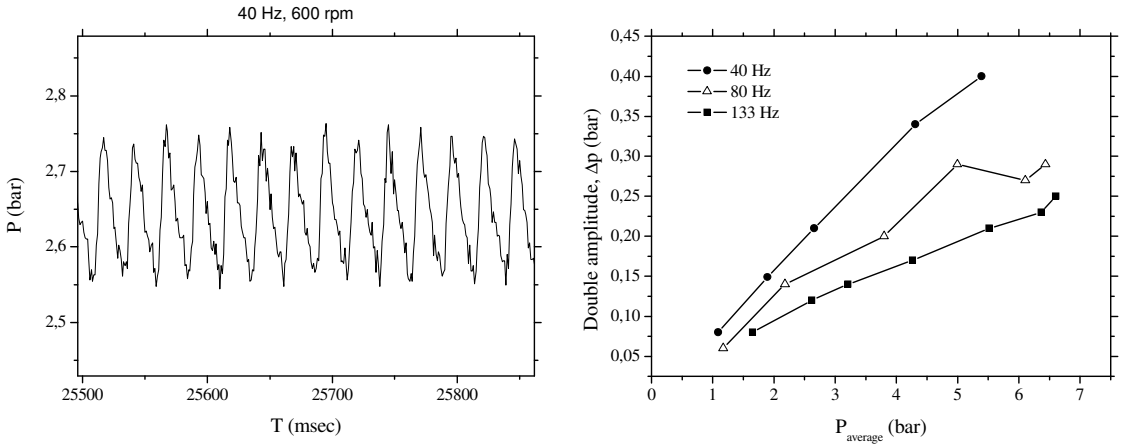

Figure 4.12: Pressure oscillation amplitude (P\) at different chamber pressures and oscillation frequencies.

Table 4.2: Peak-to-peak pressure-oscillation amplitude measured at different chamber pressures and oscillation frequencies (experiment parameters).

f (Hz) / P(bar)	36	48	63	80
2	0.17	0.15	0.14	0.13
3	0.24			
4				0.23
5	0.36			0.28

The pressure oscillation magnitudes are relatively small, for example; at 2 bars chamber pressure and 36 Hz oscillation frequency, the maximum achievable magnitude is 0.17 bar. This value increases when increasing the chamber pressure and decreases when increasing the oscillation frequency.

4.4.2 Visualization of spray behavior under oscillating pressure conditions

A comparison between single frames of the high-speed images at the same time but at different chamber pressures and the same pressure oscillation frequency shows the different behavior of spray penetration as a function of the chamber pressure. Figure 4.13 for example, presents single shots of high-speed images at 2, 3 and 5 bars at same frequency of 36 Hz. This figure gives an indication about the general spray behavior at different chamber pressures. At 2 bars, the spray has the form of a fully developed spray once it exits the nozzle.

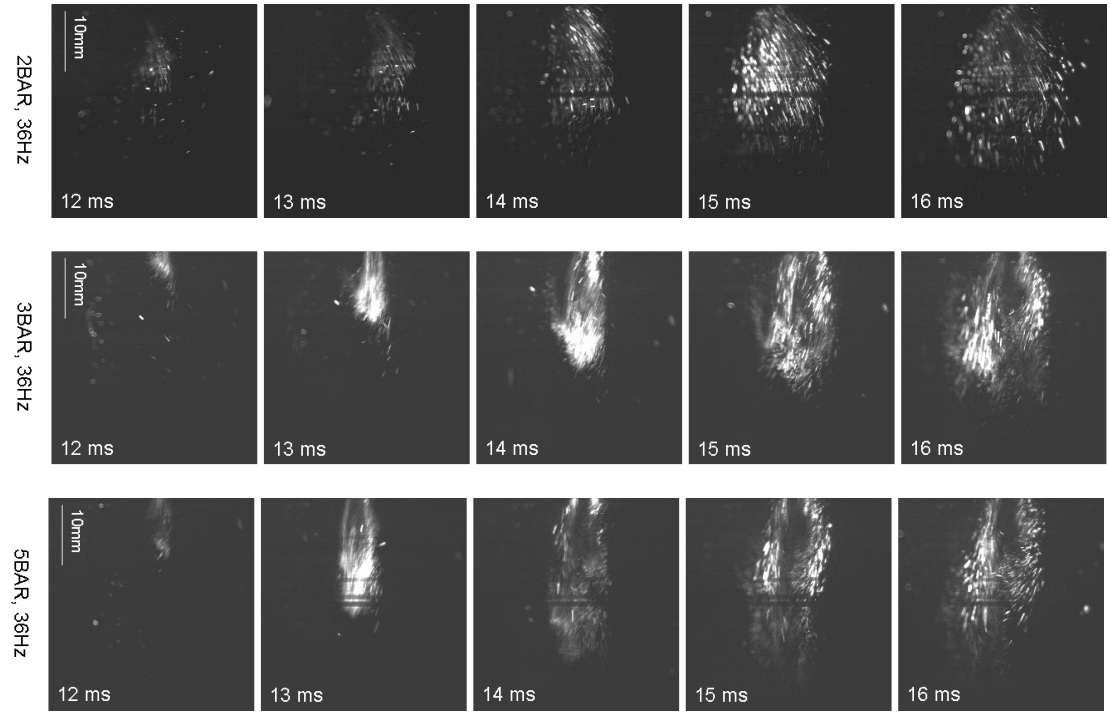

Figure 4.13: Single frames of the high-speed video camera images at constant pressure oscillation (36 Hz) frequencies and different chamber pressures

This spray penetrates further and keeps the same form till it reaches its maximum length. Whereas the same spray has completely different shape at higher chamber pressure, 5 bars for example. It starts the penetration process as a jet, then after a certain time, the spray neck starts to disintegrate and this disintegration process moves toward the spray front, and once the spray reaches the maximum length, it starts to have the fully developed, hollow cone spray shape. The spray keeps oscillating; therefore, it doesn't show a perfect hollow cone spray shape.

Figure 4.14 shows different frames of different videos at constant chamber pressure and different pressure oscillation frequencies. It is also obvious that the general penetration behavior is the same, but the magnitude is different.

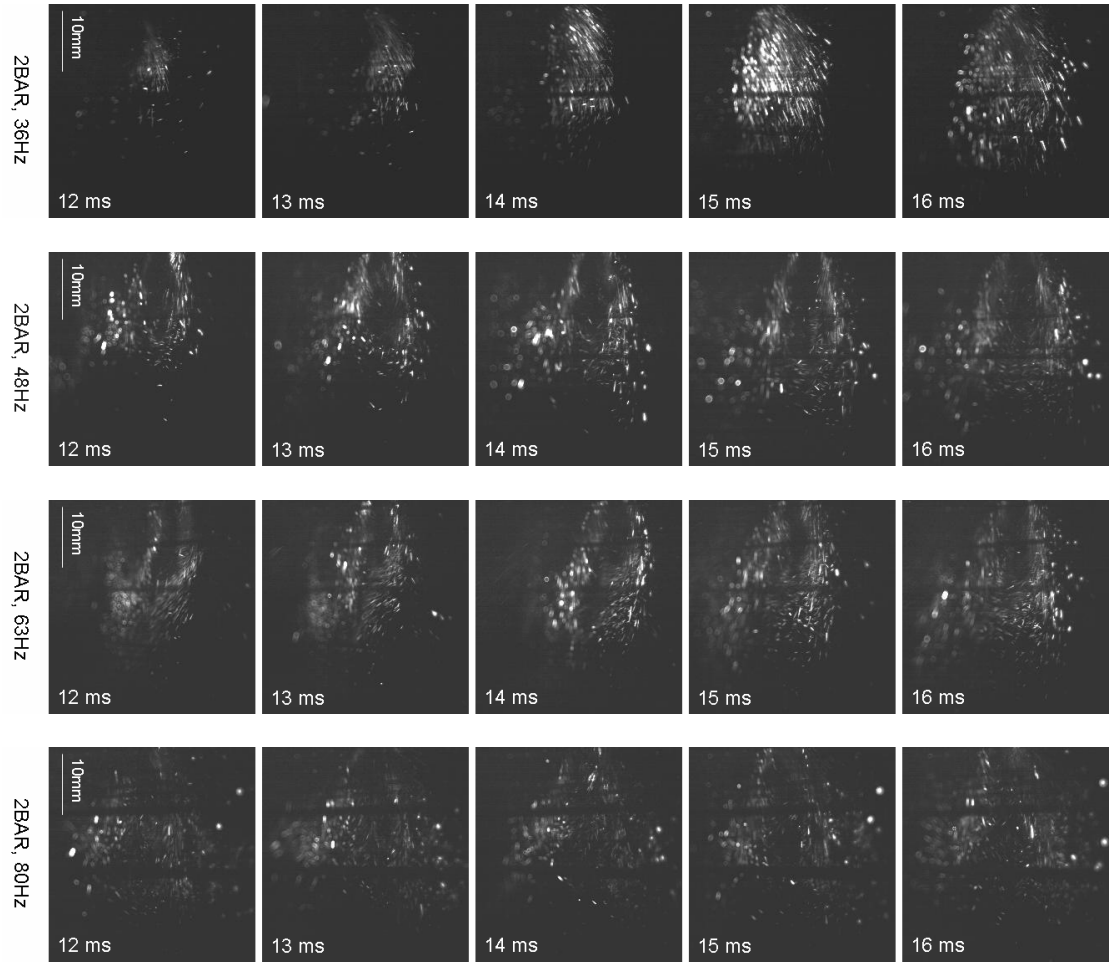

Figure 4.14: Single frames of the high-speed video camera images at constant chamber pressure (2bar) and different pressure oscillation frequencies

4.4.3 Estimation of penetration velocity

The single frame images provide information concerning the penetration velocity of the spray in the pressure chamber. This phenomenon of spray oscillation occurs due to the interaction of the spray with the pressure waves that are excited as a result of the pulsator valve movement. The velocity of the spray is calculated by processing two consecutive images of the high-speed movies for different operating conditions. In figure 4.15, the penetration velocity against the pressure oscillation-peak-to-peak magnitude at different chamber pressures is plotted. It shows that at a constant chamber pressure, the penetration velocity of the spray declines when the oscillations magnitude increases. The effect of the oscillating frequency on the penetration velocity of the spray is shown in figure 4.16. The figure shows that the penetration velocity increases as the oscillation frequency increases.

The variation in spray penetration velocity can be understood as a result of the pressure variation in the pressure chamber. As the pulsating frequency increases, the pressure

oscillation magnitude decreases. This leads to larger pressure difference between air-source and the chamber pressure. This increase in the pressure difference cause the higher penetration velocity of the spray.

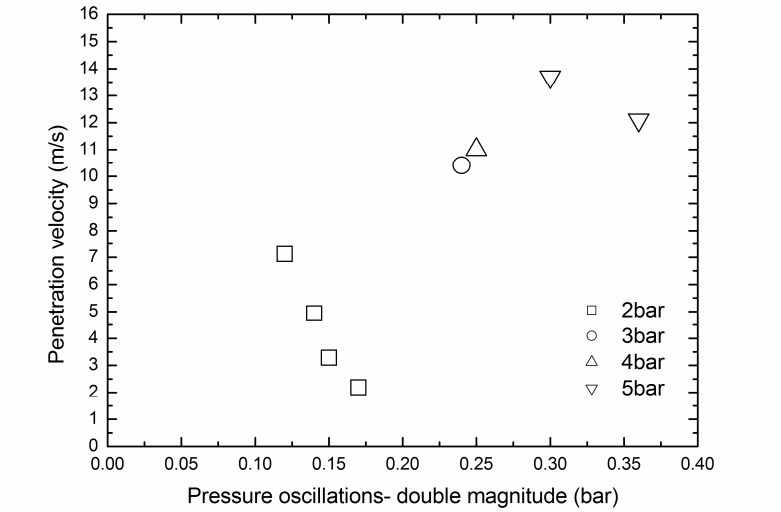

Figure 4.15: Penetration velocity of the spray as a function of the pressure oscillation double magnitude.

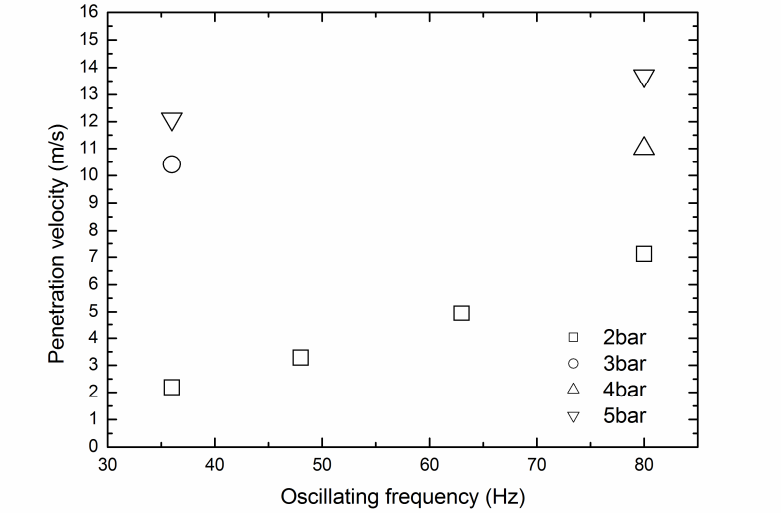

Figure **4.16**: Penetration velocity of the spray as a function of the pressure oscillation frequency.

4.4.4 Estimation of spray frequency

POD analysis of the spray images captured by the high-speed video system is a method allowing separation of the different modes of frequency based on the energy content of each mode. As a result of this technique, the frequency at which each mode occurs is obtained from the FFT analysis. In general, three oscillating modes are dominant (figure 4.17). Mode 1 represents the oscillation of the spray angle, mode 2 represents the generation of the PVC and mode 3 occurs due to the oscillation in the spray length.

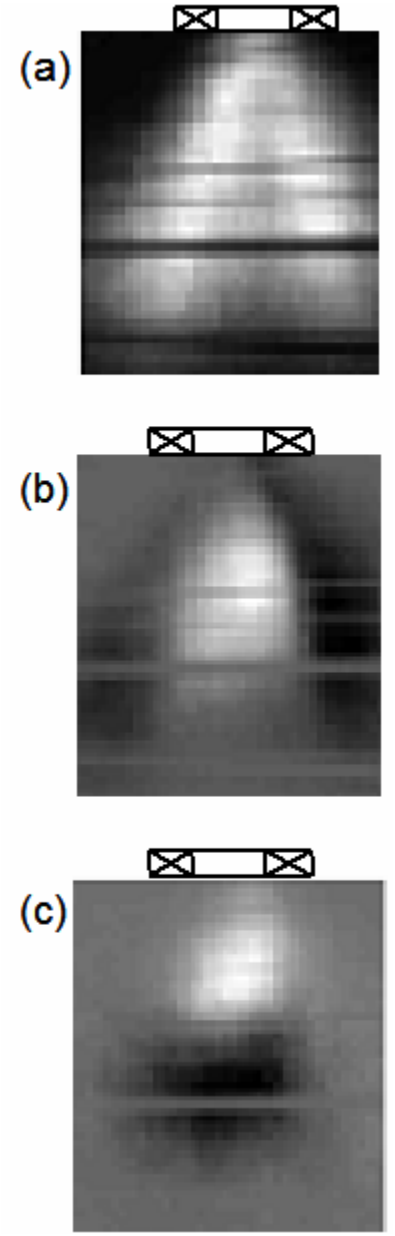

Figure 4.17: POD of spray visualisation, Modes: 1 (a), 2 (b), 3 (c)

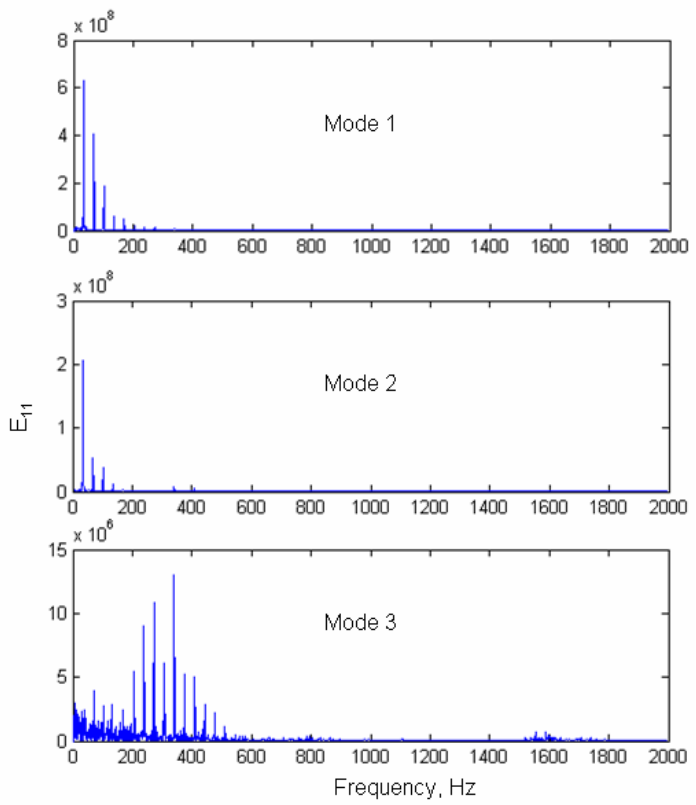

Figure 4.18: Modes frequencies at 2 bar, 20 SCMH and 36 Hz

Modes 1, 2 and 3 are observed in the entire range of the experimental parameter, however mode 3 becomes dominant only at high pressure and low frequency conditions. In all cases, all the oscillation modes happen at frequencies equal to the pressure oscillation frequencies or at multiplications of these frequencies, (figure 4.18).

The frequency values of modes 1 and 2 under free oscillation conditions are much higher than the values at forced frequency conditions at the same chamber pressure and air flow rates. For example, mode 1 occurs at a frequency of 1400 Hz at 2 bars chamber pressure and 23 SCMH air flow rate, whereas it occurs at 36 Hz and at multiplications of this value up to 108 Hz at the same conditions with forced pressure oscillation of 36 Hz.

5. Spray characterization using the phase Doppler technique

In this chapter, a parametrical study is made to investigate the effect of the chamber pressure, airflow rate and liquid flow rate on the droplet size distribution and velocity profiles of the droplets in airblast and pressure-swirl sprays. The PDA data of the smallest droplets is used to estimate the gas-phase velocity distribution. Furthermore, a novel scaling analysis of the droplet size based on the energy balance of the liquid-phase and the gas-phase is derived and validated by the experimental results.

5.1 Measurement grids

Our two-velocity components PDA instrument is used to measure the droplet size and two velocity components (axial and transverse) in the primary and the airblast sprays. Figure 5.1 shows a schematic of the measurement planes, coordinate system and the corresponding components of the velocity vector. The values of the measured transverse component of the drop velocity at the plane y-z yield the magnitude of the radial velocity component. On the other hand, the values of the transverse component coincide with the azimuthal spray velocity if the measurement volume is located in the plane x-z.

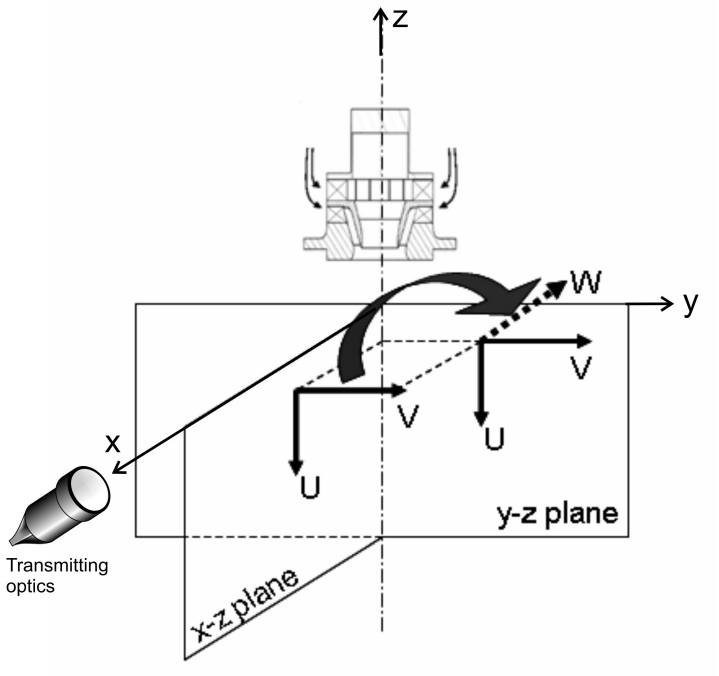

Figure 5.1: Measurement planes and the corresponding velocity components

As the dual PDA technique is equipped with four detectors, it is able to measure two velocity components (U and V) in the measurement plane simultaneously. Then measuring the same velocity components in the perpendicular plane at the same radius enables the estimation of the third velocity component (W).

For the primary spray (the spray that impacts onto the pre-filmer), the PDA data is collected at different radial positions at z = 5, 7, 9 and 11 mm downstream at steps of 1 mm. The reason behind choosing the 5 mm distance is that the primary spray impacts onto the pre-filmer in the airblast atomizer at 5 mm axial distance downstream. While in the case of airblast spray, different downstream distances are used (z = 3, 7, 11, 15 and 19 mm). Figure 5.2a and 5.2b show the measurement points for both cases.

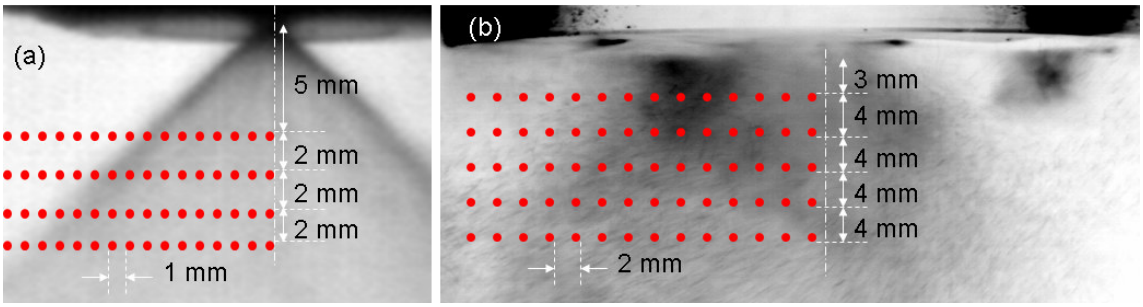

Figure 5.2: Measurements grid (a) pressure swirl atomizer; (b) airblast atomizer

The chamber pressure and the liquid flow rates are changed to study their effects on the pressure swirl (primary) spray and the airblast spray. Also, a coaxial airflow is applied at different flow rates in order to study its effect on the droplet size and velocity in the primary spray before the impact onto the pre-filmer in the airblast atomizer takes place.

5.2 Characterization of the primary spray

In order to understand the mechanism of spray formation in the airblast atomizer the detailed information on all the influencing factors is necessary. One of the important factors determining the atomization process is the primary spray generated by the pressure swirl atomizer.

Table 5.1: Operating conditions of the pressure swirl atomizers

Chamber pressure	Stroke length	Atomizer 1 (D_{PN} =0.40 mm)		Atomizer 2 (D_{PN} =0.25 mm)	
		P_L	Flow rate	P_L	Flow rate
Bar	mm	Bar	l/hr	Bar	l/hr
1	2.5	6	2.66	20	2.23
1	3.5	9	4.61	48	4.02
1	4.5	17	6.37	68	4.71
5	2.5	10	2.66	24	2.23
5	3.5	13	4.61	52	4.02
5	4.5	21	6.37	72	4.71
10	2.5	15	2.66	29	2.23
10	3.5	18	4.61	57	4.02
10	4.5	26	6.37	77	4.71

Two different pressure swirl atomizers are used to produce the primary spray. Table 4.1 shows a comparison between the two atomizers at different operating conditions.

The difference in the SMD between nozzle 1 and nozzle 2 is shown in figure 5.3. Despite the same stroke length used to provide both nozzles with liquid, nozzle 2 produces droplets almost 50% smaller than nozzle 1.

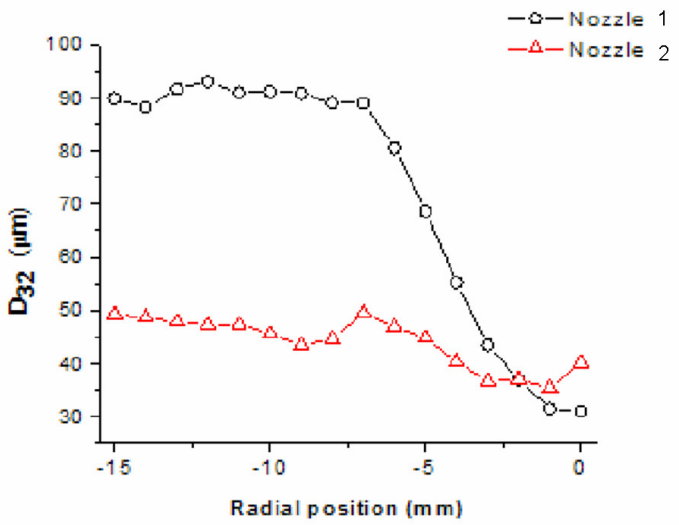

Figure 5.3: SMD distribution of nozzle 1(- ◦ -) and nozzle 2 (- Δ -)

This difference in the droplet size is expected as per the empirical correlation in [1] due to the change in the liquid-side pressure and the change in the flow rate.

$$SMD = 2.25\sigma^{2.25}\mu_L^{0.25}\dot{m}_L^{0.25}\Delta P_L^{-0.5}\rho_A^{-0.25} \quad (5.1)$$

Figure 5.4 shows the effect of the different studied parameters on the Sauter Mean Diameter of the pressure swirl spray. In figure 5.4a the change in the SMD of the droplets at different

radial positions and at different axial positions downstream is plotted. There is no significant change of the SMD during the penetration of the primary spray in the pressure chamber. This is due to the isothermal conditions of the experiment as well as the absence of secondary atomization in this case. The liquid flow rate in this case is 2.66 l/hr and the chamber pressure is 1 bar and there is no coaxial air flow.

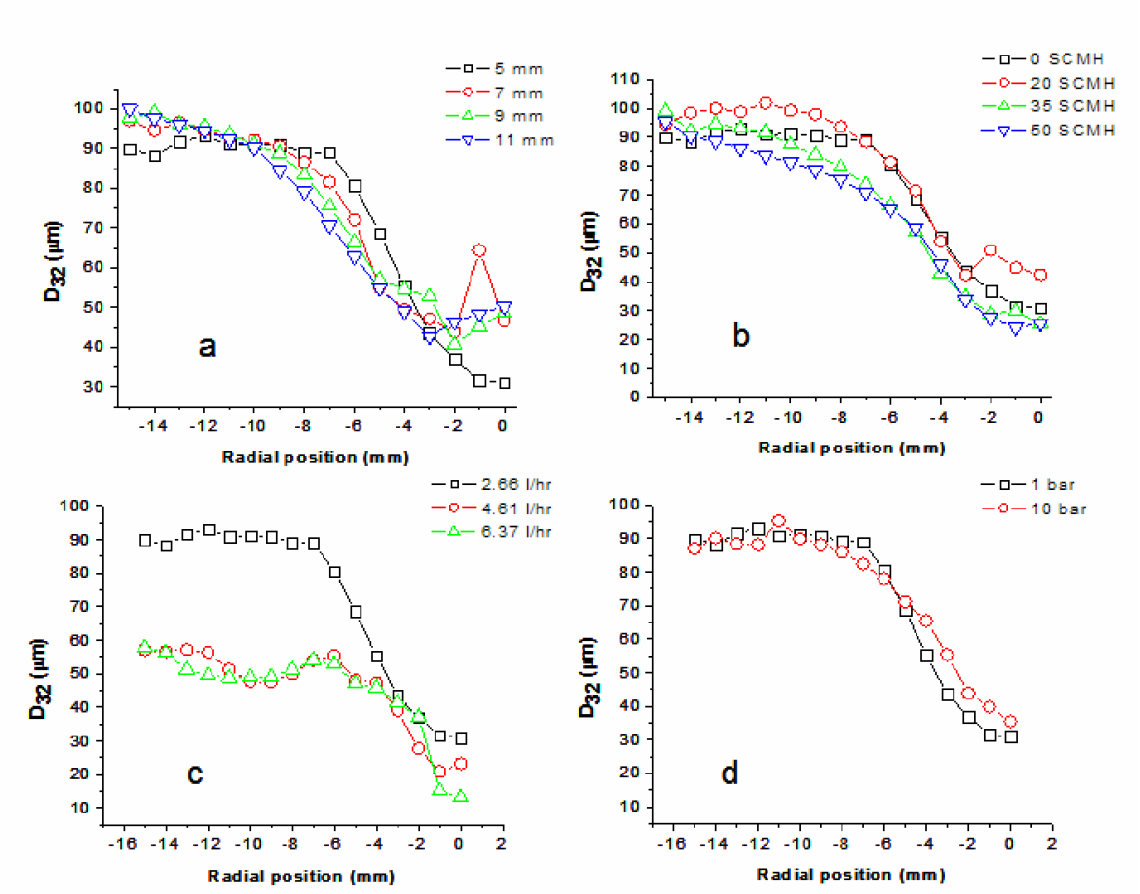

Figure 5.4: Effect of various parameters on Sauter Mean Diameter of pressure swirl spray (Nozzle 1), the chamber pressure in a, b and c is 1 bar.

The coaxial air flow has no dramatic effect on the SMD of the droplets within the pressure swirl spray as shown in figure 5.4b. The mentioned mass flow rates of air in figure 4.11b are correspond to average air velocities of 0, 2.34, 4.09 and 5.85 m/s respectively. This result confirms the argument that no secondary atomization process takes place after the atomizer orifice under isothermal conditions, even in the presence of coaxial airflow. Different is the effect of the liquid flow rate. In figure 5.4c the black line shows the radial SMD distribution of the droplets in the pressure swirl spray at 2.66 l/hr liquid flow rate, 1bar chamber pressure and without coaxial air flow. The red and the green lines represent the same but at 4.61 and 6.37 l/hr of liquid flow rate respectively. The PDA results show a drop in the SMD values

when increasing the liquid flow rate between 2.66 and 4.61 l/hr and almost no change between 4.61 and 6.37 l/hr.

The chamber pressure has no effect on the SMD of the droplets in the primary spray, despite the fact that the air density in the chamber is almost 10 times higher when increasing the chamber pressure from 1bar to 11 bars as figure 5.4d shows.

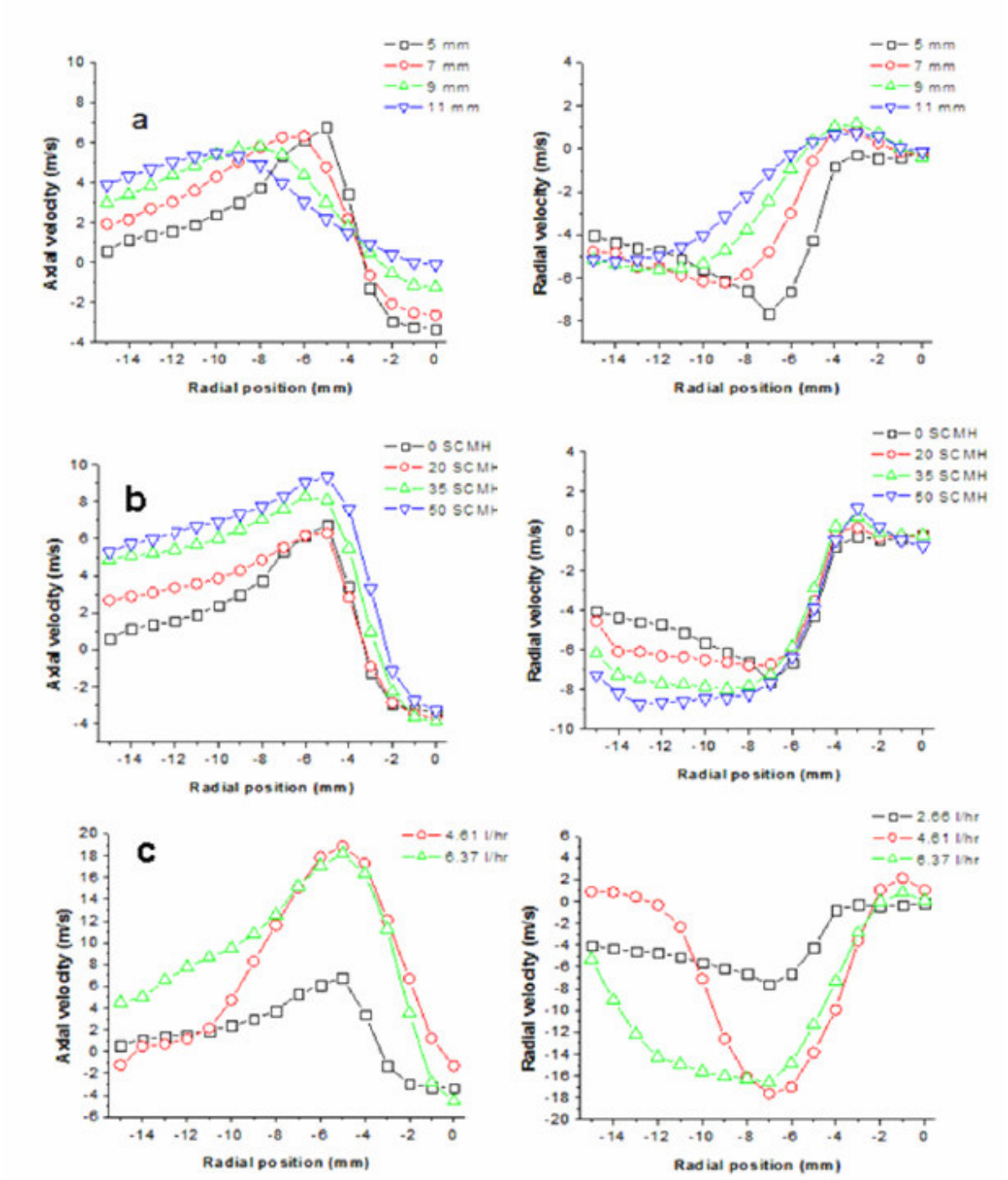

Figure 5.5: Velocity of water droplets in a pressure swirl atomizer (nozzle 1) at 1 bar chamber pressure, 2.66 l/hr. Liquid flow rate in figure a and b is 2.66 l/hr. Measurement in figures b and c are performed at z=5mm.

In figure 5.5, two velocity components of the droplets in pressure swirl spray is plotted at different operating conditions. Figure 5.5a shows the variation of the axial and radial velocity profile as a function of the spray radius. Both the axial and the radial velocities of the droplets

decrease during the penetration in the pressure chamber due to the air resistance in form of drag force. This figure shows also the increasing radial velocity and shifting of the peaks towards sprat axis with increasing z distance. In the airblast atomizer, the primary spray is subjected to a coaxial airflow before its impaction on the pre-filmer. The effect of this coaxial airflow on the droplet velocity is presented in figure 5.5b. The droplets gain part of the air momentum, and they maintain higher velocity during the penetration as in the case without coaxial airflow. This higher velocity affects the Re and We of the droplets and directly affects the film characteristics and the output of the spray-wall interaction process. The change of the liquid flow rate also affects the droplet velocity as shown in figure 5.5c.

Nozzle 2 generates droplets at higher velocity than nozzle 1. The velocity profile of the droplets as a function of the radial positions and at different chamber pressures for nozzle 2 is shown in figure 5.6. The axial and radial velocities reach 35 m/s and 25 m/s at 1 bar chamber pressure. This maximum velocity reduces when increasing the chamber pressure as shown in figure 5.6.

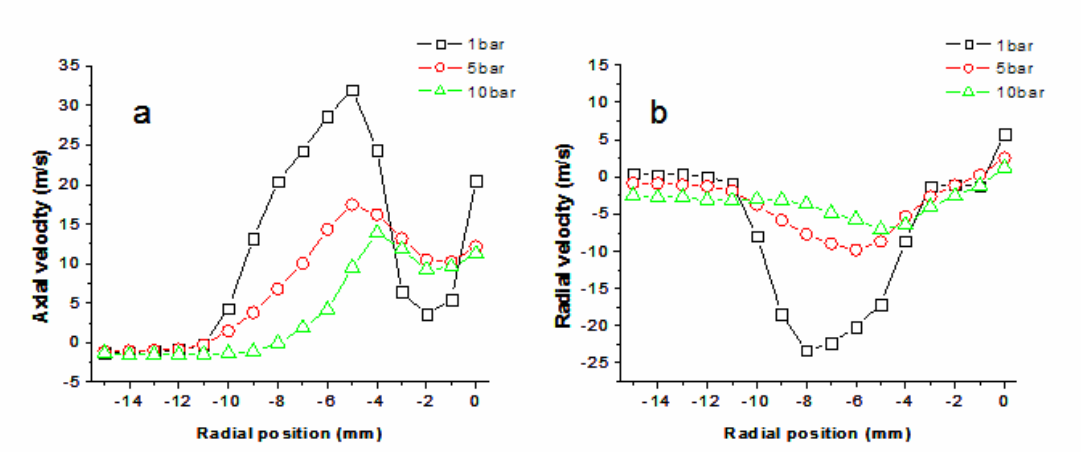

Figure 5.6: Velocity of water droplets in a pressure swirl atomizer (nozzle 2) at different chamber pressures and water flow rate of 2.23 l/hr.

The droplets in nozzle 2 break when penetrating in the pressure chamber and the peaks of both the axial and the radial velocities decline as figure 5.7 shows. The average values of the droplet diameter and velocity can be used to calculate the average Re number for the droplets at Z=5 mm. The calculations reveal values between 757 and 1423 for nozzle 1 and between 796 and 4420 for nozzle 2.

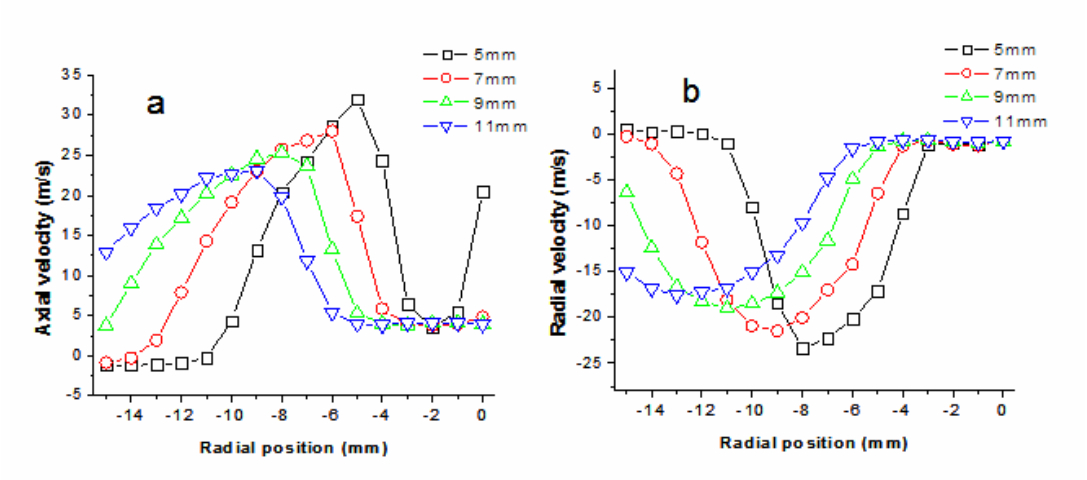

Figure 5.7: Velocity of water droplets in a pressure swirl atomizer (nozzle 2) at chamber pressure of 1 bar and water flow rate of 2.23 l/hr.

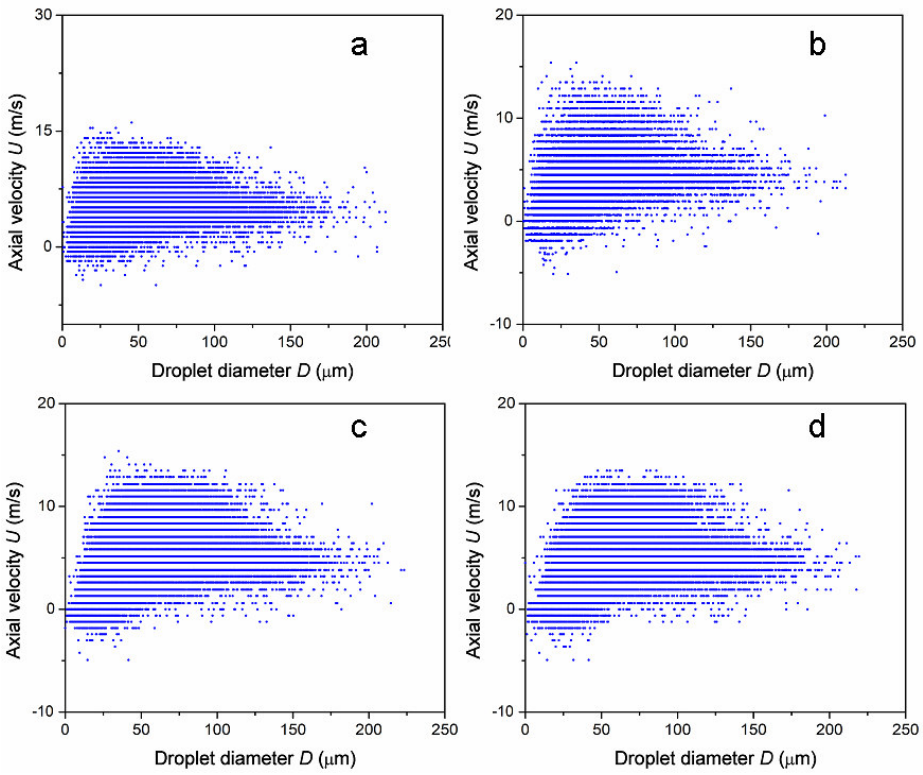

Figure 5.8: Correlation between droplet diameter and u(x) in primary spray at different measurement points: a) 0, -7,5; b) 0, 11, 7; c) 0, -11,9; d) 0, -13, 11. Chamber pressure is 1 bar, liquid flow rate is 2.66 kg/hr.

Figure 5.8 displays correlations between droplet velocity component U and its respective diameter at different radial and axial positions. During the penetration of the pressure-swirl spray in the chamber pressure, the large droplets maintain their velocity whereas the small

droplets breakup. The size distribution of the droplets in the measurement positions remains unchanged as shown in figure 5.9.

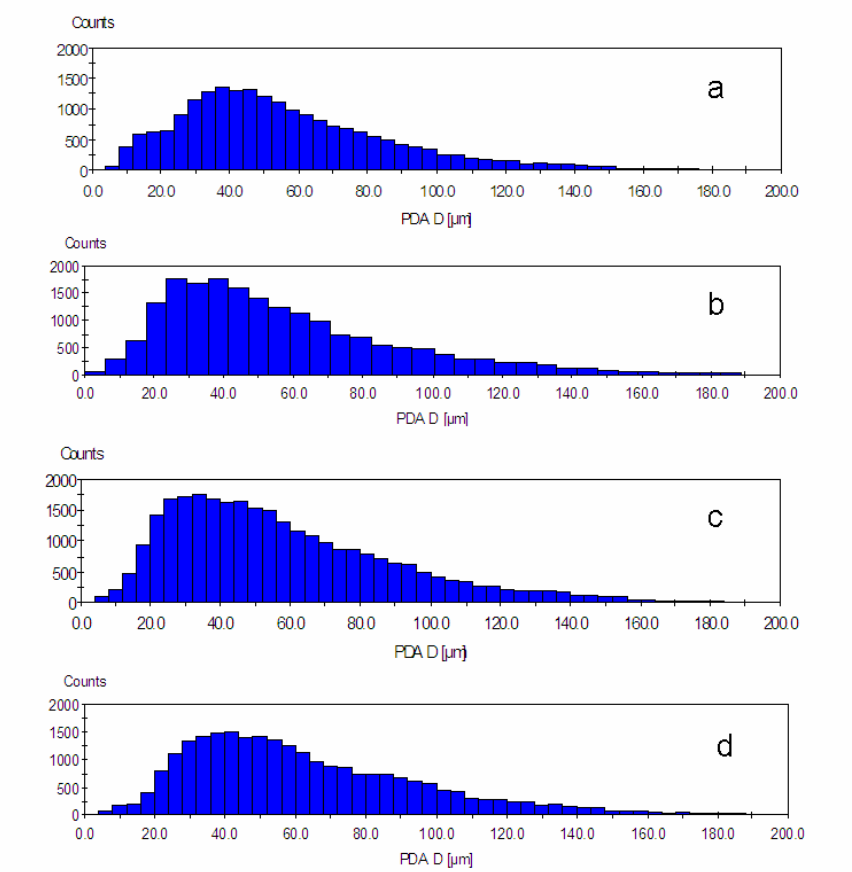

Figure 5.9: Droplet counts at different positions; : a) 0, -7, 5; b) 0, 11, 7; c) 0, -11, 9; d) 0, -13, 11. Chamber pressure is 1 bar, liquid flow rate is 2.66 kg/hr.

5.3 Characterization of the airblast spray

A parametric study has been performed to investigate the effect of the air-mass flow rate, water flow rate and the chamber pressure on the distribution of the droplet diameter and three velocity components of the airblast spray. The operational parameters are listed in table 5.2.

Under isothermal conditions the droplet size doesn't change significantly during the penetration into the pressure chamber since the effect of evaporation is relatively small. At the same downstream axial distance, the SMD of the droplets increase with distance from the spray axis. Also, there is very limited change in the SMD when moving downstream at the same radial position. This behavior of the SMD can be related to the isothermal conditions of the experiments, where both phases of the flow have the same room temperature. Also, secondary breakup of the droplets doesn't occur in this case, because We_g takes values less than 12 in most cases.

Table 5.2: Characterization of the airblast spray: list of operating conditions.

Primary Nozzle	Chamber pressure	Liquid flow rate	Air mass flow rate	AFR
	Bar	kg/hr	SCMH	
1	1	2.66	20	8
	1	2.66	35	13
	1	2.66	50	19
	1	4.61	20	4
	1	6.37	20	3
	5	2.66	20	38
	5	2.66	35	66
	5	2.66	50	94
	10	2.66	20	75
	10	2.66	35	132
	10	2.66	50	188
2	1	2.23	20	9
	1	2.23	35	16
	1	2.23	50	22
	5	2.23	20	45

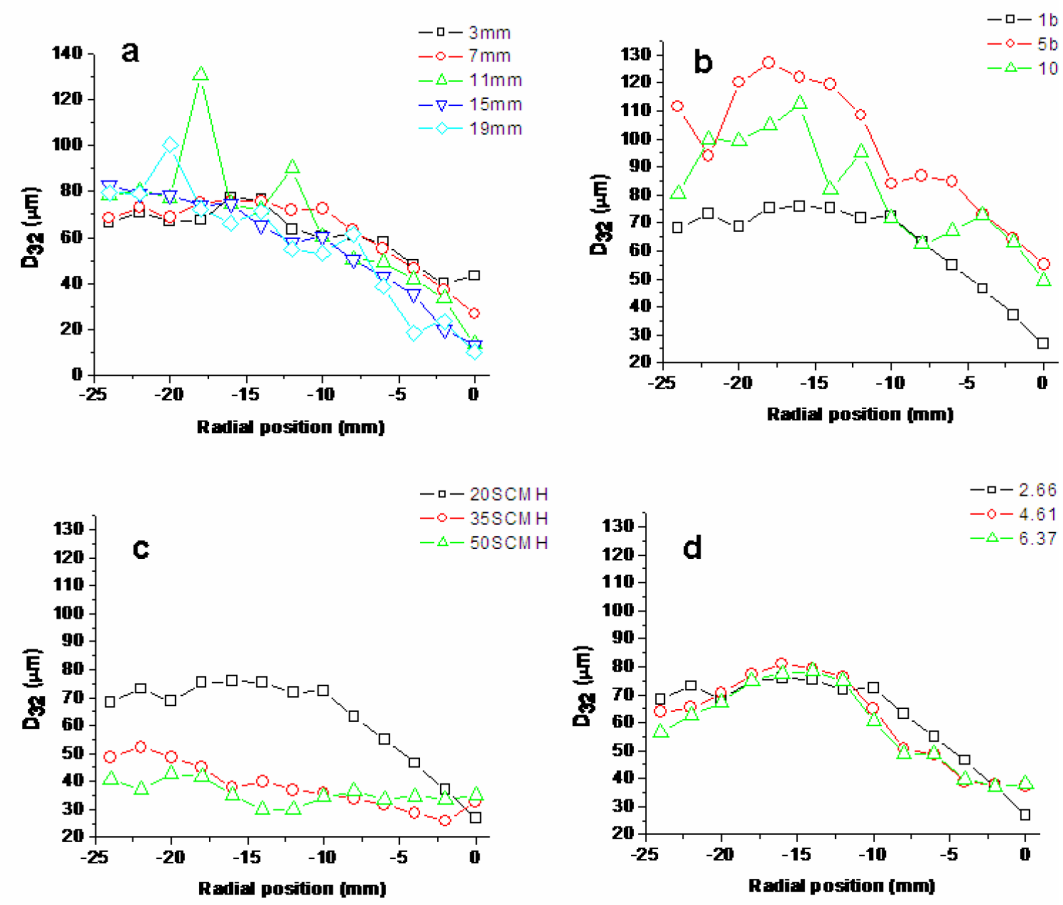

Figure 5.10: Droplet diameter distribution of airblast spray at different working conditions. a) P=1 bar, Q_L = 2.66 l/hr. Q_A = 20SCMH, b) Q_L = 2.66 l/hr. Q_A = 20SCMH, c) P=1 bar, Q_L = 2.66 l/hr, d) P=1 bar Q_A = 20SCMH,

The results obtained by the PDA measurements are processed to calculate the SMD and the average velocities at different measurement points as mentioned in 5.1.

Figure 5.10a shows the SMD of the droplets at radial positions between 0 and 24 mm and at axial distances (z= 3, 7, 11, 15 and 19 mm).

The effect of the chamber pressure, or more exact, the air density in the pressure chamber is shown in figure 5.10b. The droplet size increases when increasing the air density in the pressure chamber.. In this work, the air velocity also decreases when increasing the pressure chamber since the air-mass flow rate is kept constant at different chamber pressure values, which leads to a remarkable increase in the droplet diameter. Comparing figure 5.10b and 5.10 c shows the opposite effect of the air velocity and the air density on the droplet size. In figure 5.10c, the air mass flow rate is increased between 20, 35 and 50 SCMH which causes a decrease in the droplet size as increasing the air-mass flow rate is increased. The air velocity affects also the film thickness on the pre-filmer, which plays an important role in determining the droplet diameter after the breakup takes place. The effect of the liquid flow rate on the droplet size distribution is limited, despite the fact that the flow rate increases by double and triple, as illustrated in figure 5.10d.

The droplet velocity slightly changes during the penetration in the pressure chamber. The axial velocity component at different axial distances downstream in figure 5.11a shows almost the same maximum of around 80 m/s at z = 3, 7, 11 and 15 mm whereas, this maximum drops to 32 m/s at z = 19 mm. Also, it shows that in the region close to the axis, the droplet velocity decreases as z value increases until it reaches values in minus at z = 15 and 19 mm, which indicates the recirculation in this zone. More complicated is the behavior of the radial velocity components of the droplets. In figure 5.11b the radial velocity increases when moving from the spray axis towards its periphery, it reaches maximum at the radius r = 6 mm for z = 3, 7 and 11 mm and at r = 8 mm for z = 15 and 19 mm. Then the radial velocity decreases to reach its minimum at the periphery. The high drop in the radial velocity at z = 3 and 7 mm is due to the fact that in the region where r > 10 mm, there are almost no droplets available, as indicated by the very low PDA data rate.

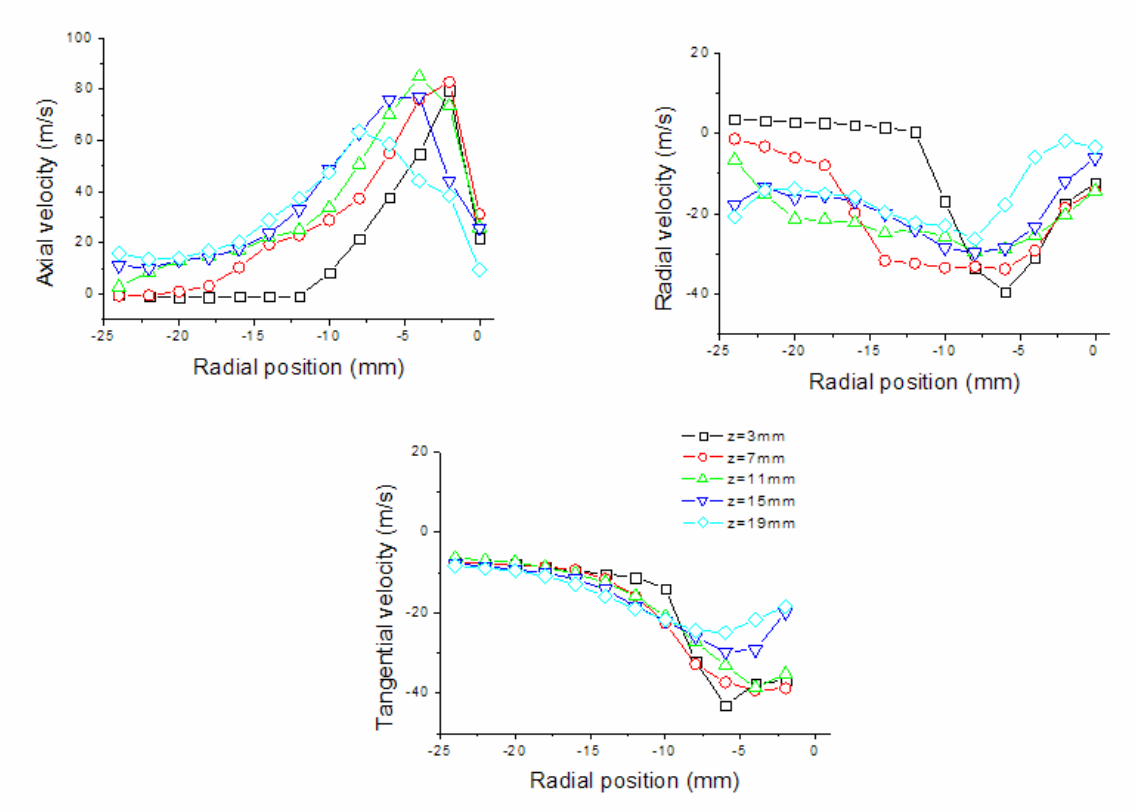

Figure 5.11: Droplet velocity components at chamber pressure of 1 bar, liquid flow rate of 2.66 l/hr and 20 SCMH air mass flow rate. Avg. PDA data rate is 0.9 kHz.

The droplets keep their tangential velocity during the penetration as shown in figure 5.11c. The droplets which are close to the spray axis gain higher azimuthal velocity than those which are close to the spray borders.

The correlations between the droplet axial velocity and size in different measurement points provide a deeper understanding of the behavior of the small and the large droplets in the spray. Figure 5.12a shows that the small droplets oscillate and follow the turbulent fluctuations while the large droplets follow their own tracks. This behavior indicates that the small droplets in this position have smaller Stokes-number. As shown in 5.12b at the cross-section 2 mm closer to the spray axis, at z =3 mm, the small droplets follow their own track with high velocity as the large droplets do but with lower velocity. This fact indicates high Stokes number for both the small and the large droplets.

At other positions the correlation indicates also large Stokes number for both the small and the large droplets, despite the fact that the small droplets are slower as in figure 5.12 for example. In positions far from the nozzle, the small droplets keep oscillating and following the turbulent as shown in figure 5.12d.

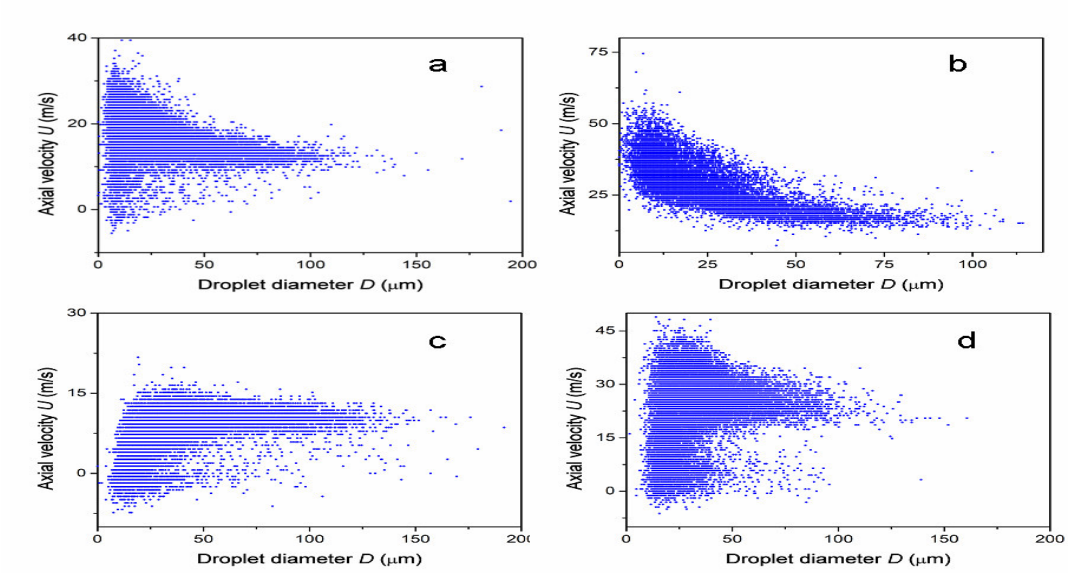

Figure 5.12: Correlation between droplet diameter and $u(x)$: a) 0, -6, 3; b) 0, -4, 3; c) 0, -12, 7; d) 0, -10, 19. Chamber pressure is 1 bar, air mass flow rate is 20 SCMH, liquid flow rate is 2.66 kg/hr.

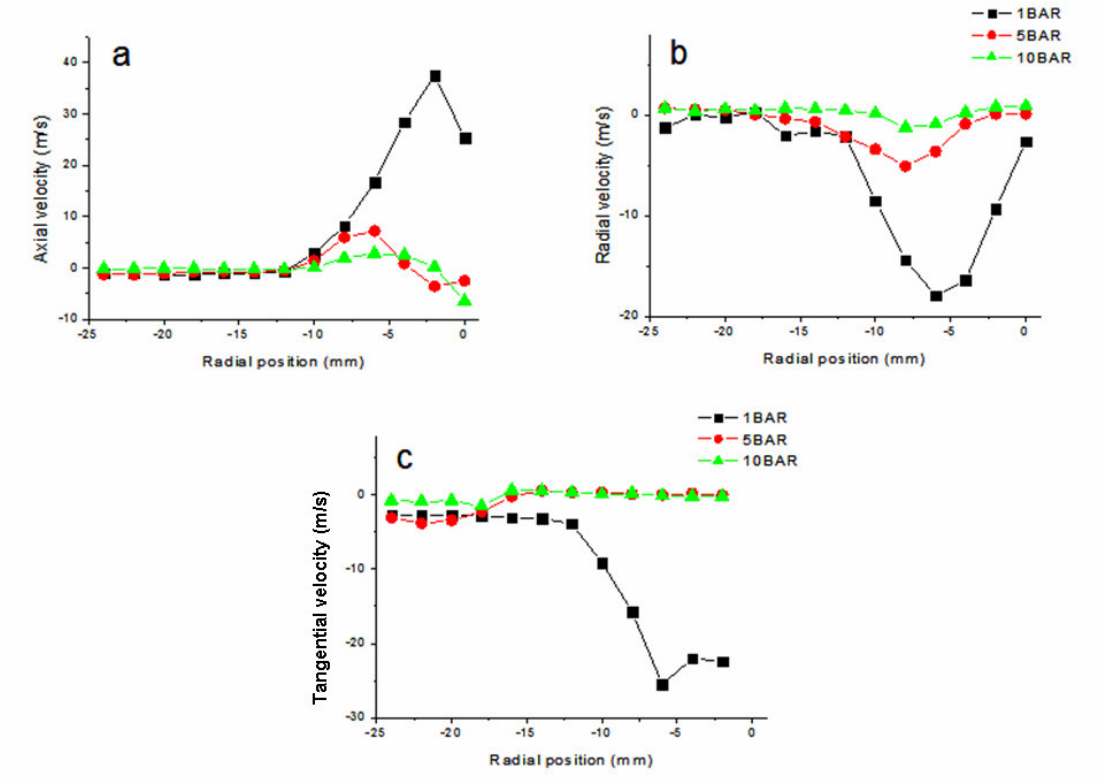

Figure 5.13: Droplet velocity components at different chamber pressures, liquid flow rate of 2.66l/hr and 20 SCMH air mass flow rate, z = 3mm

In figure 5.13 three velocity components are plotted at different radial positions and at different chamber pressures. The air density linearly increases when the pressure increases. This change in the air density leads to a decrease in the three velocity components. In this experiment the air-mass flow rate is kept constant, which results in a reduction of the air velocity as the air density increases. This reduction in the air velocity is responsible for the decrease of the droplet velocity components.

Increasing the air-mass flow rate at constant chamber pressure leads to an increase in the air velocity. The higher the air velocity is the faster are the droplets. This can be seen in figure 5.14. The three velocity components and the absolute velocity are plotted against the radial position at 3 mm downstream and at 1 bar chamber pressure.

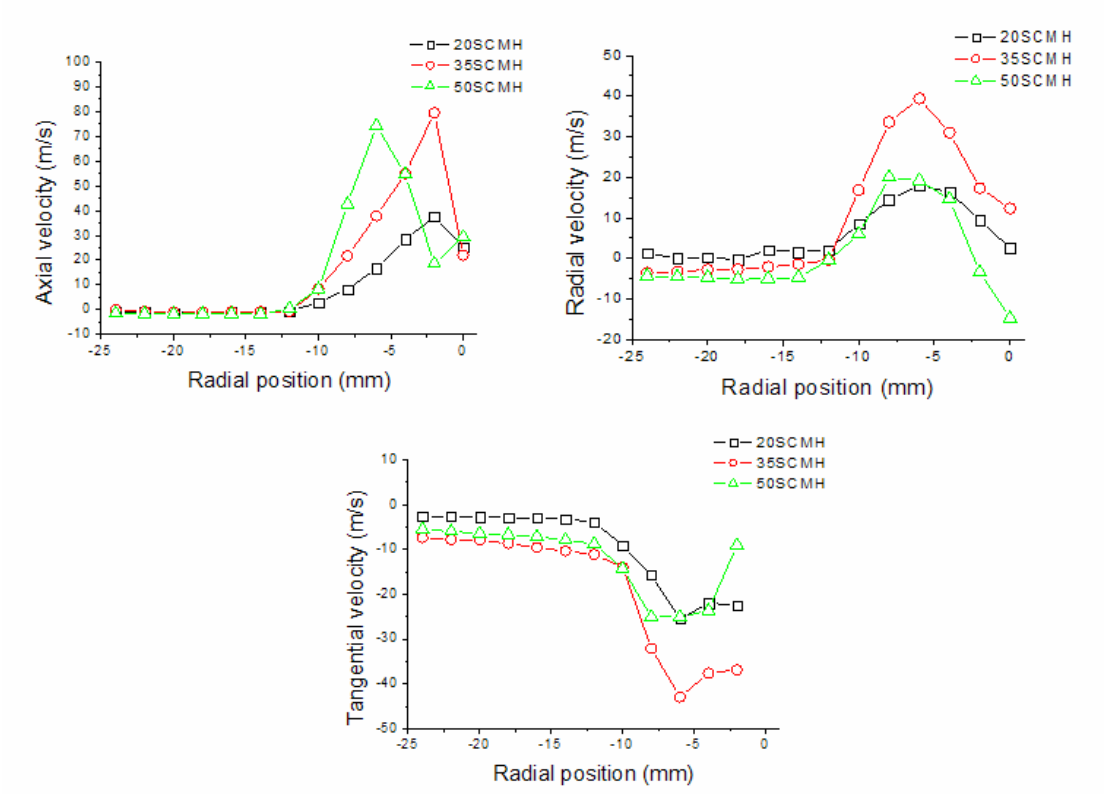

Figure 5.14: Effect of air mass flow rate on the droplet velocity components, liquid flow rate is 2.66 kg/hr, chamber pressure is 1bar.

The change in the air mass flow rate leads to noticeable changes in the droplet velocity. In the region close to the spray axis, a strong recirculation takes place, as seen in the axial velocity plot. The maximum droplet velocity occurs at 6 mm radial distance, far from the spray axis. This maximum doesn't change even when the air mass flow rate is changing. It is also meaningful to mention that the magnitude of the droplet velocity in the recirculation zone reaches abou 30% of the maximum droplet velocity in the main flow region at 50 SCMH.

At this stage, one can compare three typical sprays, which helps one to understand the mechanisms of atomization inside the airblast atomizer:

- primary spray generated by the pressure swirl nozzle, (*spray 1*);
- spray generated by the airblast atomizer but without the air flow. This spray is the combination of the drops from the primary spray and the secondary spray formed by spray-wall interaction inside the atomizer (*spray 2*);
- spray generated by the airblast atomizer at relatively low flow rate, 20 SCMH, of the air (*spray 3*).

Measurements for primary spray have been performed in the range of the radial coordinate $-15 < r < 15$ mm at a distance 5 mm downstream of the pressure swirl nozzle. The zero air flux spray has been characterized in the range of the radial distances $-10 < r < 10$ mm at 5 mm from the atomizer cup exit in the axial direction, whereas measurements for the atomized spray have been performed at the radial distances $-24 < r < 24$ and 5 mm from the atomization cup in the axial direction.

The result of the comparison is shown in figure 5.15. The velocity of the *spray 2* is much smaller then the velocity of two other sprays. This is caused by the kinetic energy dissipation of droplets during their impact onto a wall of the atomizer. The velocities of the *sprays 1* and *2* are comparable at the given conditions. It is interesting that the diameter of droplets in *spray 2* has the same order as the drop diameter of *spray 1* and *spray 3*. This result can be related to the spray/wall impingement process, since the secondary droplets have the same order as the primary droplets. This proves that the main goals behind using the airblast atomizer are to achieve better mixing and higher volume mass ratio.

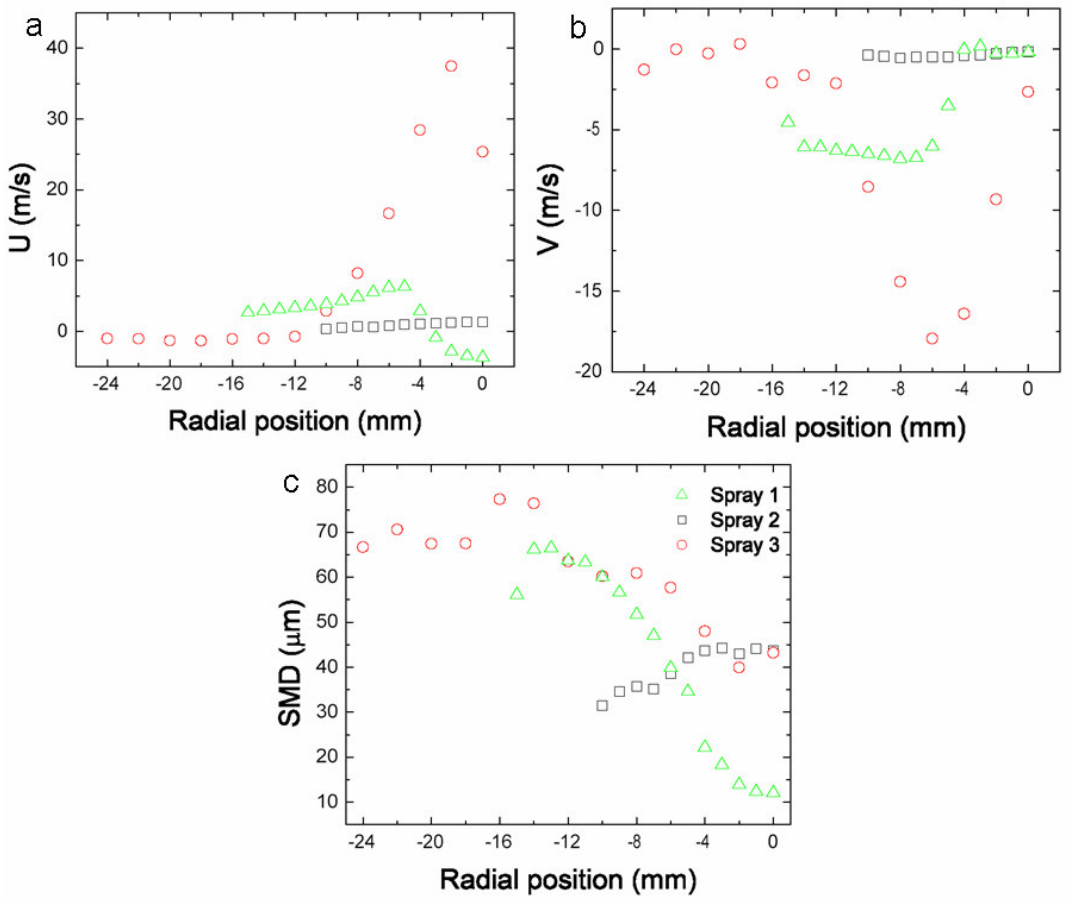

Figure 5.15: Comparison of three typical sprays at 1 bar chamber pressure and 2.66 l/hr water flow rate: a) axial velocity, b) radial velocity and c) droplet diameter.

This comparison revealed the main influence of the airblast process on the primary spray, in which the spray gains larger volume/mass ratio, and the droplets gain a tangential velocity component that enhances the mixing. Furthermore, the air entrainment close to the spray axis and the recirculation zone outside the spray boundaries enhances the mixing, but also introduces new aerodynamic phenomenon that influences the combustion quality and the lifetime of combustion chambers.

5.4 Estimation of air velocity in airblast spray

Injection of seeding particles in the air path to measure the air velocity is complicated in the available setup due to high atomization pressure inside the aerosole generator. Therefore, the PDA data for liquid phase measurements are used to estimate the air velocity distribution of the gas phase. The validated liquid particles that have diameter equal or smaller than 10 µm

are considered to be representative of the gas-phase velocity. The data presented in figure 5.16 is this estimated velocity at 5 mm downstream.

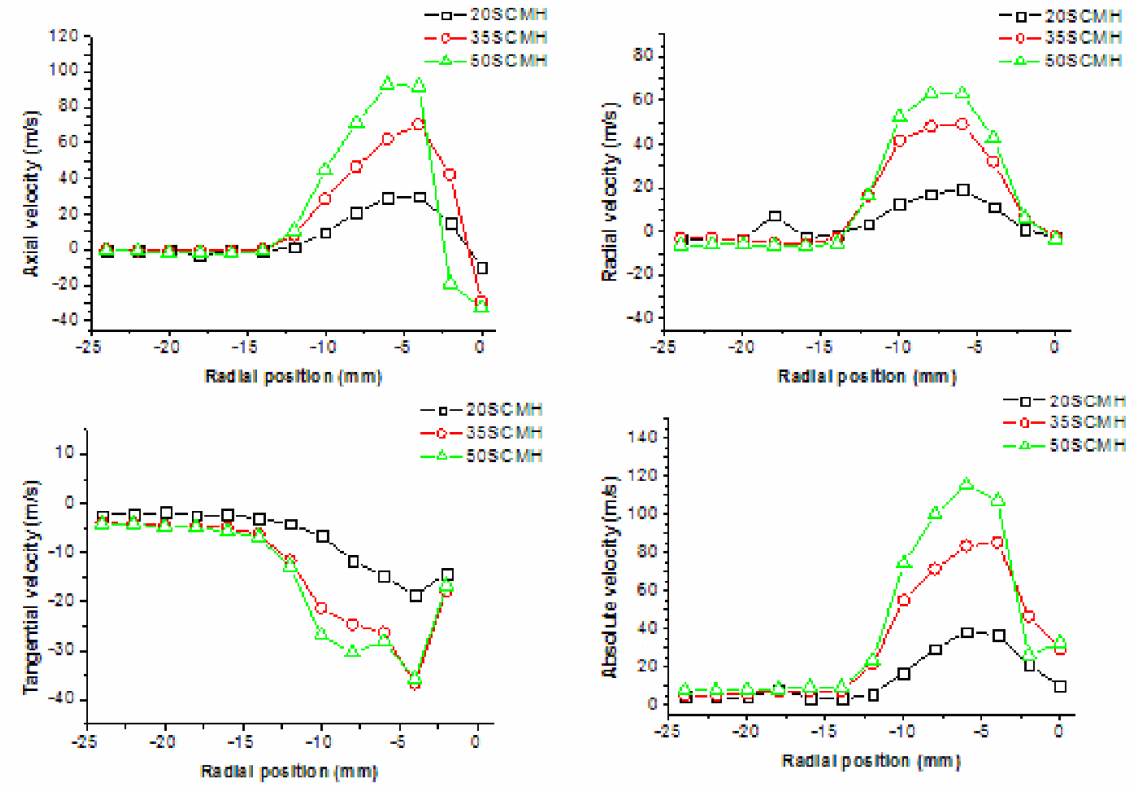

Figure 5.16 : Estimated air velocity at 5 mm distance downstream, chamber pressure is 1 bar.

Another method to estimate the maximum air velocity at the exit of the airblast atomizer is to simply average the air volumetric flow rate to the exit area of the airblast atomizer. Doing so results in 52, 91 and 130 m/s for 20, 35 and 50 SCMH flow rates respectively.

Comparing the maximum estimated velocity at 5 mm downstream with the calculated velocities at the exit of the airblast atomizer shows good agreement taking into consideration the decrease of air velocity over 5 mm downstream distance. Based on these procedures, the values of the air velocity at the exit of the airblast atomizer are given in table 5.3.

Table 5.3: Estimated air velocity at exit of airblast atomizer

Chamber pressure Bar	Airflow rate SCMH	Estimated velocity m/s	Calculated velocity m/s
1	20	38	52
1	35	86	91
1	50	116	130
5	20	9	10
5	35		18
5	50		26
10	20		5
10	35		9
10	50		13

The normalized axial velocity component of the droplets under 1 bar chamber pressure at different air mass flow rates is plotted in figure 5.17. Droplet velocity is normalized to the average air velocity in the same measurement position. In the previous section, droplet size is plotted against the radial position in the spray. Linking the previous results of the droplet size with the normalized velocity mentioned here, one can notice that the droplets with relatively small size are in the region close to the spray axis. As the droplet size in this region is small, this reveals a small drag force, which result in higher velocity and therefore higher normalized velocity. The droplets with the highest velocity at 20 SCMH air mass flow rate gain maximum 60% of the air kinetic energy, whereas the droplets has almost 90% of the air velocity at 50 SCMH air mass flow rate.

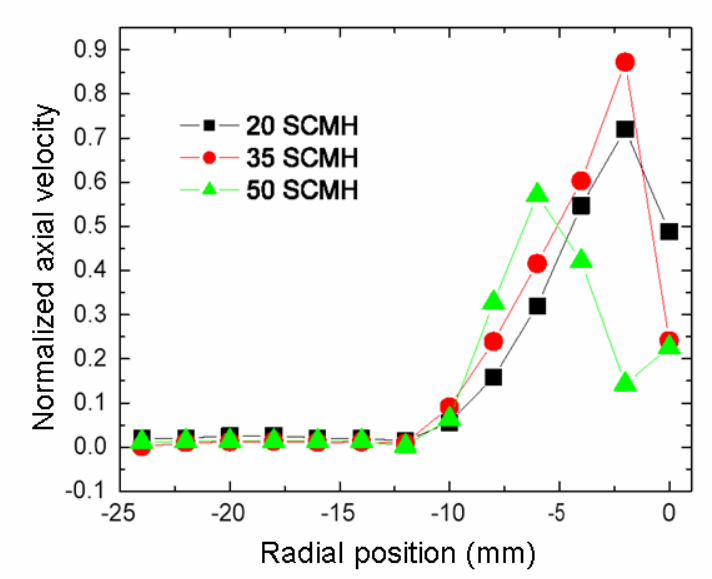

Figure 5.17: Normalized droplet axial velocity at 1 bar chamber pressure and 2.66 l/hr water flow rate

6. Modelling of atomization

One of the important parameters characterizing the performance of the atomizer is the average diameter of the liquid droplets in the spray. A weighted averaged Sauter Mean Diameter (SMD) of the drops is defined by

$$SMD = \frac{\sum_{i=1}^{n} N_i D_{32i}}{\sum_{i=1}^{n} N_i} \tag{6.1}$$

Since the 1960's the basic knowledge provided by early work has been used to develop airblast atomizers of aero engines and gas turbines. Major contributions have been made by Lefebvre and his group [43-59], as summarized in [1,53]. The effect of different parameters; air pressure and velocity, liquid flow rate, temperature, viscosity and surface tension, atomizer design and geometry on the droplet size distribution and on the atomization efficiency has been experimentally investigated. Empirical correlations concerning discharge coefficient, film thickness, droplet size as well as the flow number for pressure swirl atomizer are given. The mechanism of liquid sheet breakup in airblast atomizers is also discussed. For example, empirical correlations for the drop size are reported [44-47]:

$$D_{32} = 0.95\frac{(\sigma \dot{m}_L)^{0.33}}{\rho_L^{0.37}\rho_A^{0.30}U_A}\left(1+\frac{\dot{m}_L}{\dot{m}_A}\right)^{1.7} + 0.13\left(\frac{\mu_L^2 d_o}{\sigma\rho_L}\right)^{0.5}\left(1+\frac{\dot{m}_L}{\dot{m}_A}\right)^{1.7} \quad [44] \tag{6.2}$$

$$D_{32} = 0.48 d_o\left(\frac{\sigma}{d_o\rho_A U_R^2}\right)^{0.4}\left(1+\frac{\dot{m}_L}{\dot{m}_A}\right)^{0.4} + 0.15\left(\frac{\mu_L^2 d_o}{\sigma\rho_L}\right)^{0.5}\left(1+\frac{\dot{m}_L}{\dot{m}_A}\right)^{1.0} \quad [46] \tag{6.3}$$

$$D_{32} = 3.33x10^{-3} d_o \frac{(\sigma\rho_L d_o)^{0.5}}{\rho_A U_A}\left(1+\frac{\dot{m}_L}{\dot{m}_A}\right) + 13.0x10^{-3}\left(\frac{\mu_L^2}{\sigma\rho_L}\right)^{0.425} d_o^{0.575}\left(1+\frac{\dot{m}_L}{\dot{m}_A}\right)^{2.0} \quad [45] \tag{6.4}$$

$$D_{32} = 0.33 d_o\left(\frac{\sigma}{d_o\rho_A U_R^2}\right)^{0.6}\left(\frac{\rho_A}{\rho_L}\right)^{0.1} d_o\left(1+\frac{\dot{m}_L}{\dot{m}_A}\right) + 0.068\left(\frac{\mu_L^2 d_o}{\sigma\rho_L}\right)^{0.5}\left(1+\frac{\dot{m}_L}{\dot{m}_A}\right) \quad [47] \tag{6.5}$$

These correlations differentiate between two main parameters that play an important role in the formation of the droplets in: surface tension and viscosity.

In [60], the diameter of droplets generated by breakup of liquid film under high pressure air flow has been correlated in the form

$$D_{32} = (2.67\text{x}10^4 U_L P_A^{-0.33} + 4.11\text{x}10^6 \rho_A U_A P_A^{-0.75})^{-1} \tag{6.6}$$

These correlations indicate that the study of the spray generated by airblast atomizers remains highly empirical. These empirical correlations are only valid for specific designs of the airblast atomizers and can only poorly estimate the droplet size for different atomizer models or operating conditions.

Previous work in [29] report on measurements under cold and hot conditions performed on the original MTU atomizer as well as on an improved atomizer with different pre-filmer design. The pre-filmer could be improved by using a sharp trailing edge instead of a rounded one. This improvement in the design leads to better mixing and significant reduction of the NO_x. Similar work has been carried out by the DLR group in Cologne [15, 29, 61]. In [15], the effect of using a pre-filmer in a 2-D atomizer model on the mechanism of the droplet generation in airblast spray under isothermal conditions has been investigated. The high-speed video images show that the mechanism of the film breakup significantly differs in the presence of the pre-filmer on the atomization lip in comparison with the case without pre-filmer. The result of the 2-D spray generated by the atomization lip with pre-filmer is better than that generated in its absence. The authors recommend the use of airblast atomizers with pre-filmer rather that without pre-filmer, since the droplet size is smaller and the 2-D air/liquid ratio is higher.

In [61] the effect of the counter-swirl in double-annular air flows on the mixing of the small droplets and the air is investigated. It was found that the small droplets generated at elevated pressure follow the streamlines of the airflow and remain trapped in the inner annulus, preventing the formation of homogenous fuel-air mixture in the annular flow.

The MTU atomizer used in this work has been also used by [29, 62] to generate an airblast spray at varies boundary conditions. Under isothermal conditions, increasing the ambient pressure and keeping a constant AFR leads to production of larger droplets and a decrease in their velocity. The results showed typical phenomena for turbulent swirled flow fields such as coherent structures and recirculation zones.

In the present work the effects of the drop aerodynamic breakup and of spray/wall interaction on the final droplet size in the airblast spray are investigated. Finally, the drop size is estimated using the theory of chaotic disintegration.

6.1 Secondary breakup in the airblast spray

In order to model the atomization process it is neseccary to determine what is the dominant mechanism of atomization among the aerodynamic film breakup, spray/wall atomization or secondary (aerodynamic) drop breakup. Some existing correlations for the secondary atomization of a single drop are given in the section 1.3.3. These correlations are used to estimate the importance of the secondary drop breakup under the current experimental conditions.

As exhibited in the introductory part of this chapter, the Weber number We_g, defined in (1.2), is a measure for the secondary atomization regimes. Another measure is the stable diameter (d_{st}) of the droplets defined by (1.6). First the values of d_{st} for nine cases are calculated and compared with the average SMD of the measured droplets to determine the cases where secondary atomization is possible.

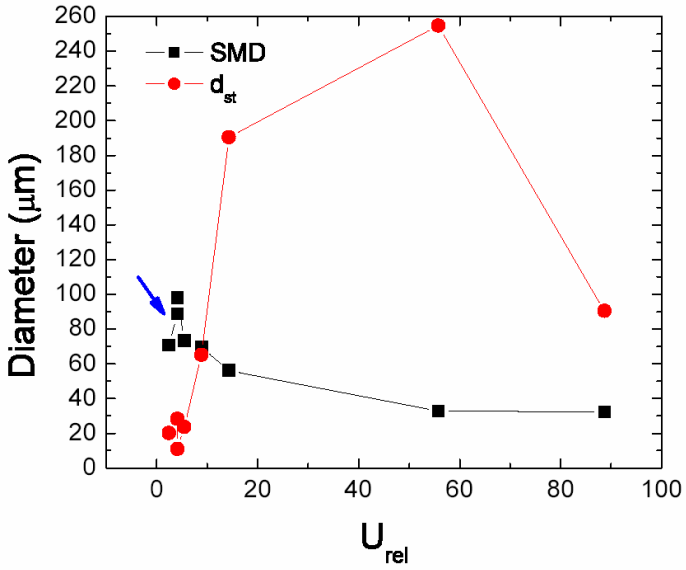

Figure 6.1: Comparison of SMD and the stable diameters of the droplets

In Fig. 6.1 the stable diameter of the spray is calculated for the different operating conditions. In the same plot, the measured droplet diameter of the spray is also plotted. It is shown that in some cases the droplets have the possibility to go through secondary atomization process, since the stable diameter is smaller than the measured diameter. The cases where secondary atomization very potentially takes place are marked by an arrow in the plot. Therefore, further control is needed by calculating the relevant We_g. Knowing the average droplet velocity and the average air velocity, the We_g can be calculated and compared with the criterion mentioned in [16-18]. Despite the fact that the measured SMD is larger than the stable diameter in some

case, no secondary atomization is taking place since We_g in all cases is smaller than 12, which is the minimum limit for the vibrational atomization as shown in figure 6.2.

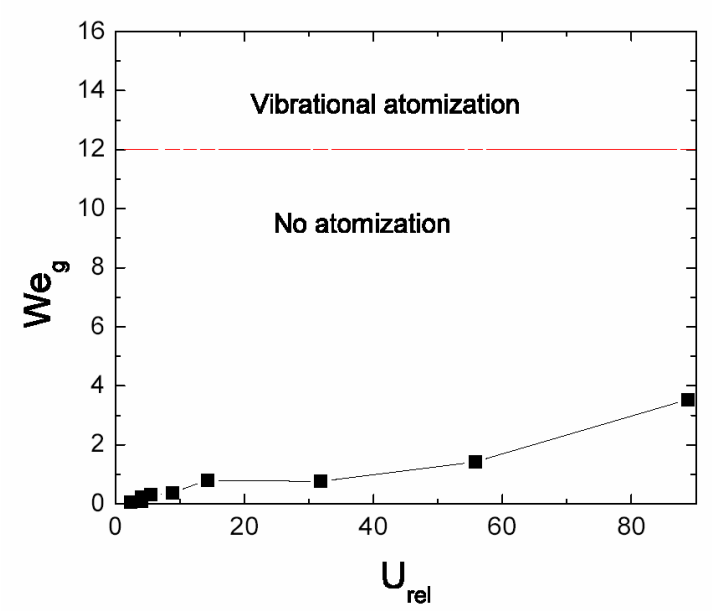

Figure 6.2: We_g of the measurement cases compared with the minimum value required for vibrational atomization mode

The above analysis indicates that secondary atomization of the droplets in the airblast spray is not a major source of small droplets in the spray, since the droplets have either a diameter below the stable diameter or low We_g number (which is below the breakup threshold), or a combination of both.

6.2. Spray impact onto an inclined wall

When a spray impacts onto a solid surface a thin liquid film and secondary spray may be generated, depending on the impaction conditions. This phenomenon is of great interest for a wide variety of industrial and processing applications. In spray coating, for example, a well defined liquid film is needed to ensure uniform distribution of the paint without generating secondary spray, so as to minimize over spray [63-64]. The aim in spray cooling of hot surfaces may be different, where preferably no formation of liquid film is required to avoid any decrease in heat transfer rate, which might occur when a liquid film is generated on the hot surface. The same is required in internal combustion engines where the fuel, injected into the cylinder, can strike cylinder walls, combustion chamber walls, or walls of the intake valve

[64]. In these cases, fuel deposition on the wall can cause adverse effects by developing a liquid film on the wall, which leads to unburned hydrocarbons emissions.

Spray impact investigation is a relatively new research field. This is due to the large difficulty in extracting detailed data from experiments [65] and their interpretation. Recently, the use of several advanced technologies has allowed experimental analysis of the phenomenon to be performed. The use of the phase Doppler technique [64, 66-69] or laser Doppler technique [70] has enabled rather exact characterization of the primary spray and the secondary spray. Another technique is high-speed video , which quantitatively facilitates the examination of individual droplet impacts [71]. In the studies [64, 67] the images of spray impact are shown only to describe the behavior of the spray. In the work [72] two CCD cameras and a PDA system are used to investigate the effect of interactions of impacting neighboring drops on a single droplet impact outcome. The images were processed to extract diameters and velocities of the droplets, which resulted in an acceptable accuracy.

Different models can be found in the literature that attempt to capture the phenomenon qualitatively. Basically two modeling strategies are presented. The first approach is based on the representation of spray impact as a simple superposition of single drop impact events. The second approach is a statistical one that based on a large number of spray impact measurements and data analysis to model the phenomenon under predefined parameters.

Study [73] has reported a comparison between six of single-drop empirical models for spray impact onto solid walls [65-66, 74-77] It is shown in [78] that these single droplet impaction models are inadequate due to unaccounted for interactions between drops which arise during spray impact. This also result in inadequate prediction of the amount of liquid deposited on the surface, as shown by [78-79]. In [78] an alternative model has been developed, taking into consideration the interaction of the neighboring droplets by introducing a statistical parameter to account for droplet interactions. Furthermore, in [80] the interaction of two droplets impacting onto a surface has been experimentally investigated. The goal of this study is the modeling of the polydisperse spray impact.

Most of the models in the literature are developed based on data obtained from spray impact onto spherical or horizontal targets, which is difficult to be used in estimating the film thickness on the pre-filmer in the atomizer under consideration.

Understanding and modeling of the phenomenon have consumed time and efforts from researchers and investigators worldwide, yet no universal model is claimed to be achieved. This is due to the extreme complexity of the phenomenon and the numerous variables envolved. In this work, the efforts are oriented to achieve a scaling criterion for the film

thickness on inclined surfaces that is generated as a result of the impact of water sprays. For this purpose, a new spray impact facility is designed and fabricated to simulate the conditions in the airblast atomizer as previously shown in section 2.1.

6.2.1 Observations of spray/wall interaction

In this section some series of single frame images are presented to establish the fact that the phenomenon is complicated enough that makes its modeling through a basic understanding of the underlying physics a very difficult task.

The effect of the target inclination on the film thickness and on the secondary spray ejected from the impingement process can be seen in figure 6.3. In general, splashing takes place in almost all cases and the output from the interaction varies between a clean lamella breakup, fingering breakup, sliding lamella and more chaotic behavior. A detailed description of some sources of complexity is given with images in the following paragraphs.

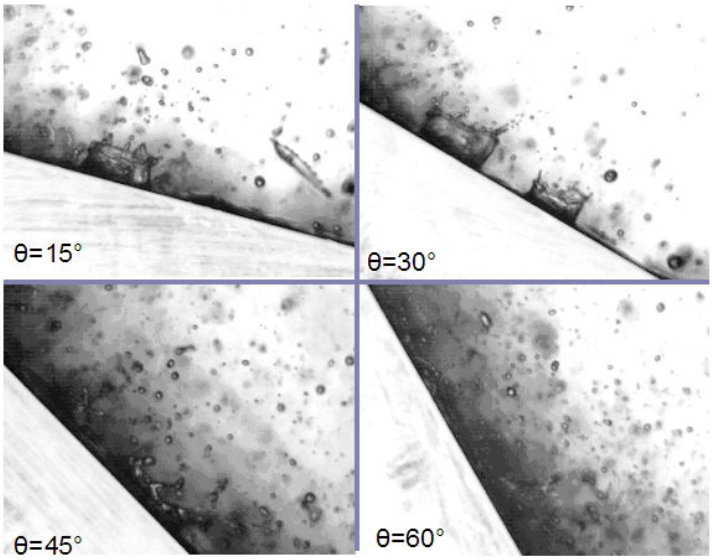

Figure 6.3: Single frames of spray impact onto targets with different angles

Figure 6.4 shows the process of impacting droplets within the spray onto a 15° inclined target. In figure 6.4 (1), one of the droplet impacts, yielding a rising lamella that breaks up to the fingering stage and before the process ends, one of the secondary droplets is encapsulated by another incoming droplet as shown in figure 6.4 (2) to (5). Then this droplet impacts onto the target yielding again a lamella and then somewhere close to this region, another droplet collides with a rising droplet and breaks up before reaching the target and disturbing the liquid film.

Different effects can be observed when analyzing the impact of a spray onto a target of different inclination angle, 45° for example as shown in figure 6.5. In this case, one can observe the creation of the lamella after the impact of the droplets onto the liquid film. Then the lamella starts to slide downwards and before the breakup phase, another primary droplet impacts onto the lamella, complicating further the whole phenomenon.

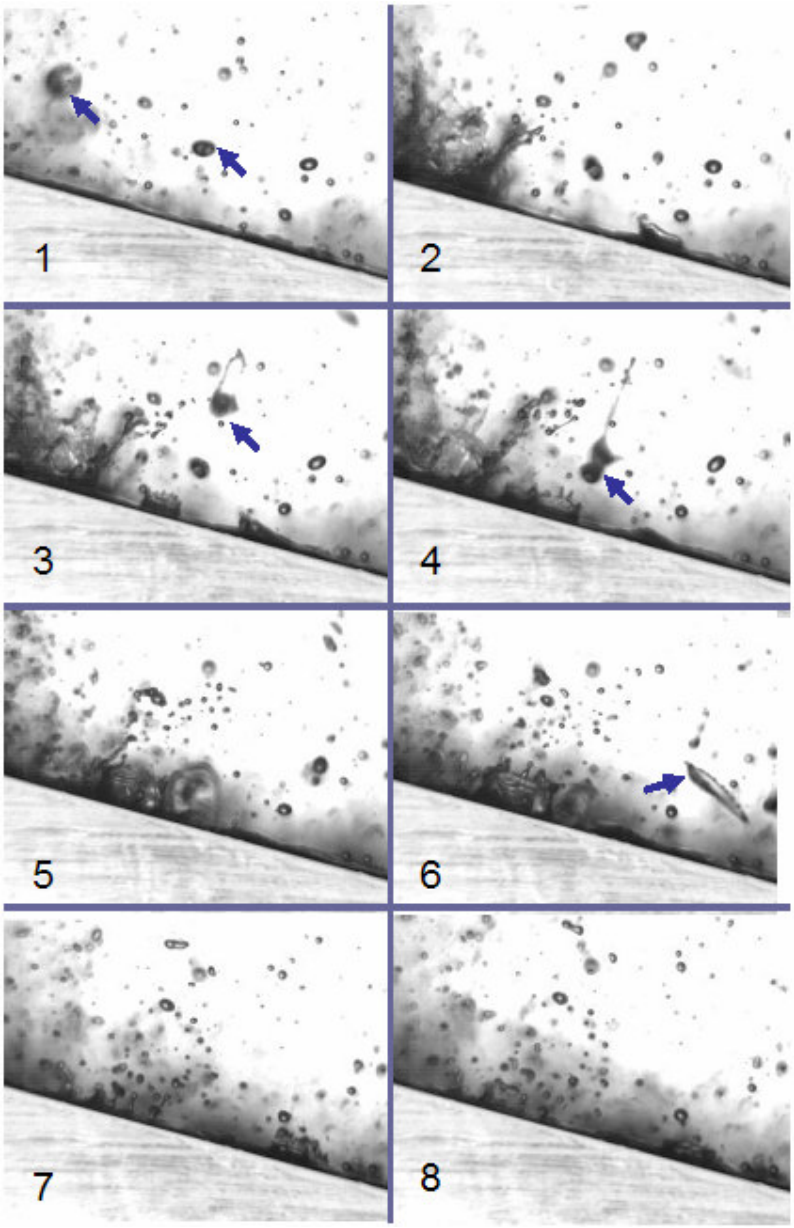

Figure 6.4: Spray impact onto 15° target

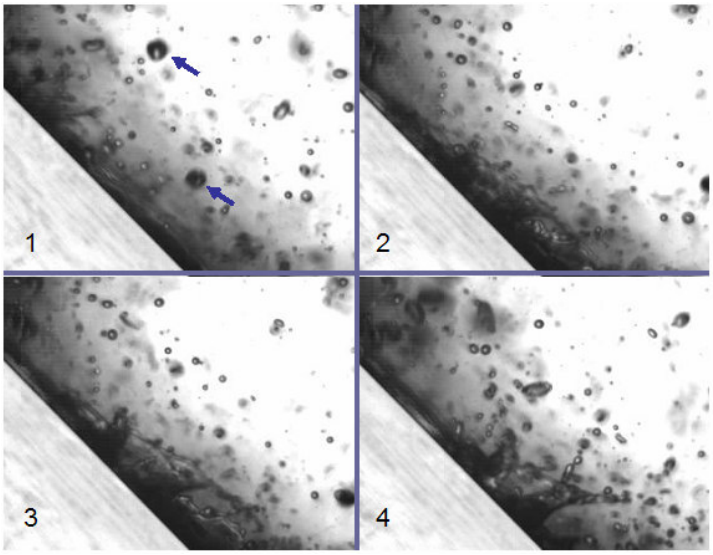

Figure 6.5: Spray impact onto 45° target

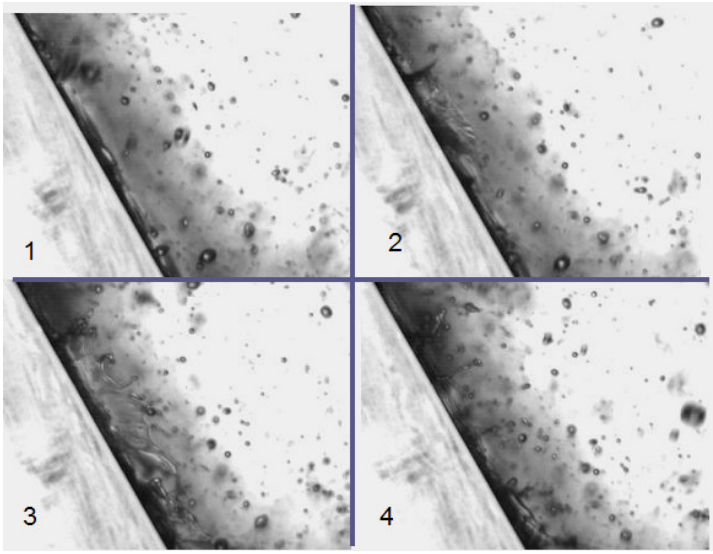

Figure 6.6: Spray impact onto 60° target

If the inclination angle increases, as shown in figure 6.6 and 6,7, the secondary droplets of the impact on the upper part of the target might impact again onto the target again at different positions . The static images presented here don't prove this process, but they are clear in the animated high-speed movies.

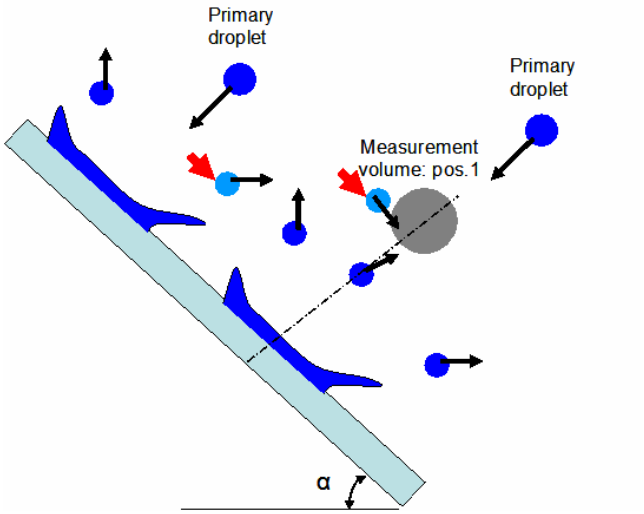

Figure 6.7: schematic of spray impact (Primary and secondary droplets)

6.2.2 Estimation of film thickness using high-speed video images

The high-speed video images provide qualitative information concerning the spray behavior and these images can also be processed to quantitatively estimate the film thickness. Images were captured using a Photron® (FASTCAM-SA1) high-speed video camera at 54k frames per second and shutter speed of 1/101000 s, from which 3k frames are saved to be processed.

A customized Matlab® routine [84] is used to process the high-speed video images in order to estimate the film thickness on the target for each saved image. The images have gone through a process of filtering so as to minimize the error in the estimated film thickness. An example result for each step is shown in figure 6.8.

In step (I), original images are recognized by the routine and the intensity in every pixel averaged with the value of the neighboring pixels in step (II). In step (III), the average pixel value is compared with a reference image (the target without spray). Then the images went through filtering processes (IV-V) to eliminate any deposits in the image and to intensify the black part of the image. The result image (VI) is used to find the contour of the liquid film, and finally the contour image is compared with the dry target image.

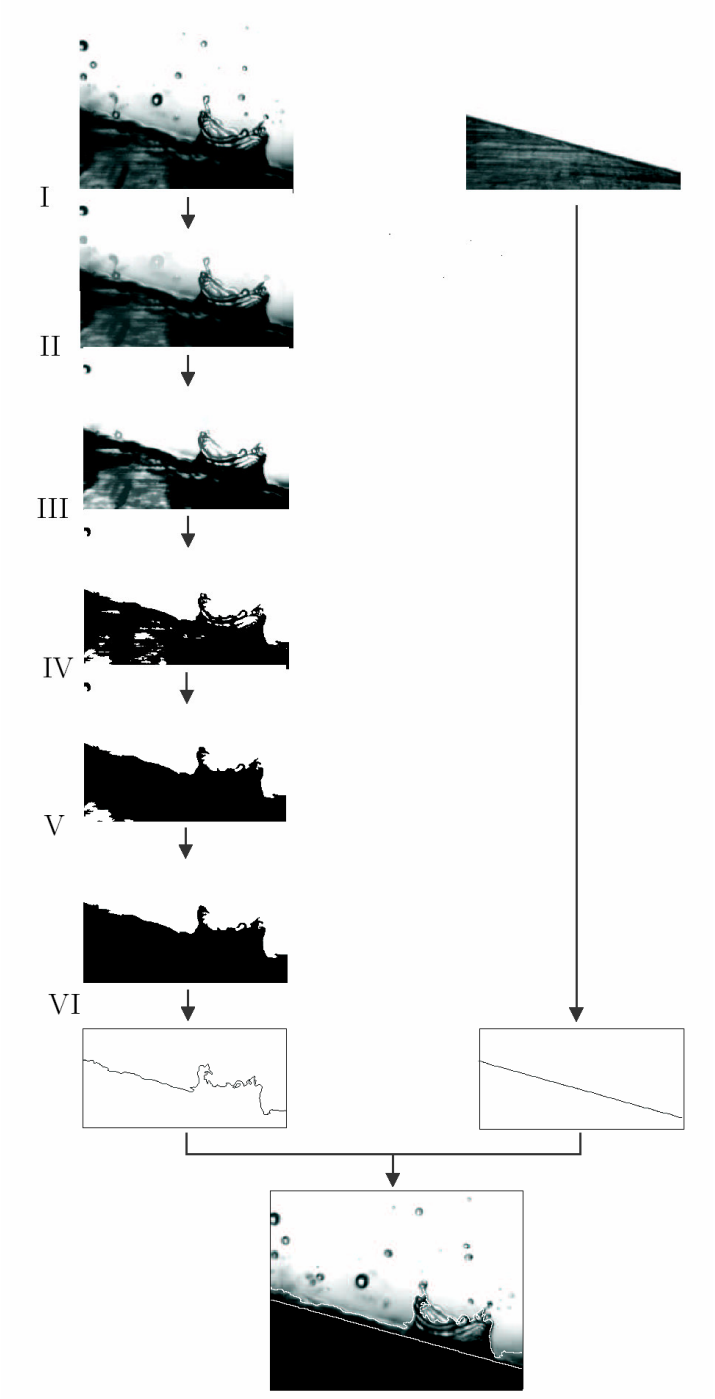

Figure 6.8: Flow map of image processing procedures

The minimum value of the film thickness along the target for each image is considered for further analysis as shown in figure 6.9. The reason behind this is that the use

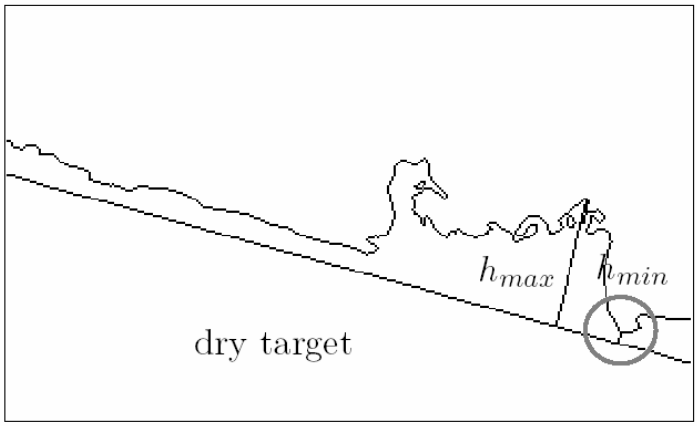

Figure 6.9: Results of the image processing routine

of the average film thickness can lead to exaggerated value since the splashing takes place in almost all images, which means that the lamella height could be considered as a film in the calculations.

Then, the most probable film thickness is estimated by examining the probability distribution of the minimum film thickness over all captured images. This distribution is treated as Gaussian and all samples that do not lie between 95% of $H_{\min}$ +/- 1.96σ, where σ is the variance and $\overline{H}$ is the mean value of $H_{\min}$ are eliminated. For this approach, distances of every pixel of the contour line of every image over the whole set of images are recorded, and then plotted in a histogram to reveal its characteristic distribution. Then using the kernel density smoothing method and its continuous probability density function which is determined by equation (6.7) the accuracy of the results is imroved. The resulting histogram of the thicknesses and its probability density function is shown in figure 6.10.

$$pdf(H) = \frac{1}{nb}\sum_{i=1}^{N} K\left(\frac{H - H_i}{b}\right) \tag{6.7}$$

where n is the total number of observations $H_1 \ldots H_n$, b is the bandwidth of a single bar in the histogram, K is a curve weighting observations close to H higher than those far away from H.

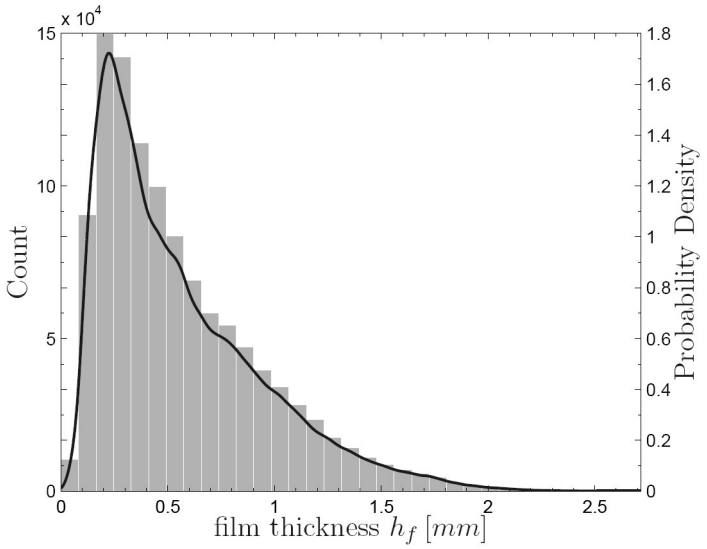

Figure 6.10: Histogram of the measured H_{min} and its probability density distribution

6.2.3 Phase Doppler measurements

Measurement grids and experimental parameters

Measurements in three directions are used to capture the incoming and outgoing droplets of the impacting spray. In the normal direction to the target, the first measurement plane is 2 mm above the target and then measurements in two further planes at 3 and 4 mm above the target are made. In the plane which is parallel to the transmitting optic lens, the measurement grid is 2 mm high and 12 mm long as schematically shown in figure 6.11.

Two parameters are changed in this set of experiments; first the angle of inclination of the target is varied between 15º, 30º, 45º and 60º, whereas the mass flux through the nozzle is

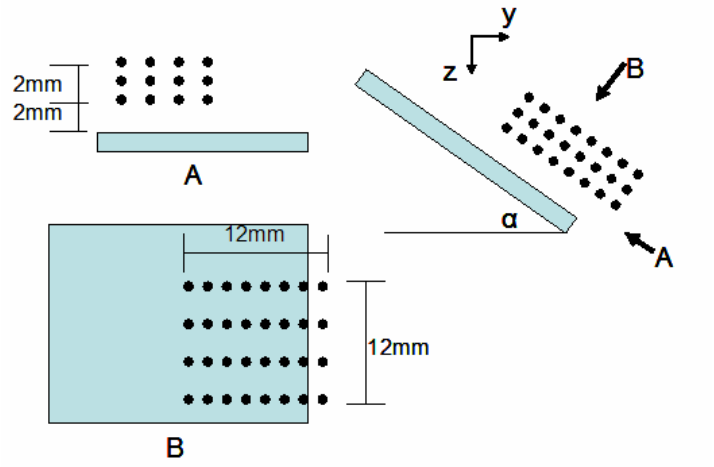

Figure 6.11: Schematic drawing of the measurement grids

varied between 0.35, 0.45, 0.55 and 0.65 l/min for each target inclination. The spray is injected through a simplex nozzle that generates a full-cone spray of 80º angle. The principles of the phase Doppler system and the optical configuration are presented in section 2.2.

To optimize the quality of the results, the minimum number of the collected samples needed for reliable results can be calculated as the PDA data are discrete and independent. Let φ be the typical measured quantity (for example the velocity component or diameter) of the droplets, and the variance of its mean value is $\sigma_{\bar{\varphi}}^2$, which can be calculated by $\sigma_{\bar{\varphi}}^2 = \frac{\sigma_\varphi^2}{N}$, where N is the number of collected, independent samples. Normalizing this expression yields the relative normalized variance $\varepsilon^2 = \frac{\sigma_{\bar{\varphi}}^2}{\bar{\varphi}} = \frac{\sigma_\varphi^2}{N\bar{\varphi}}$.

From preliminary measurements, the values for *U, V* and *D* are known. Demanding a value of 1% for ε yields 5800 as a minimum required number of samples. Since the data rate and the validation ratio are relatively high, the maximum data acquisition time for each measurement position is set to be 20 seconds, which yields more than 17000 samples.

Characterization of spray impact

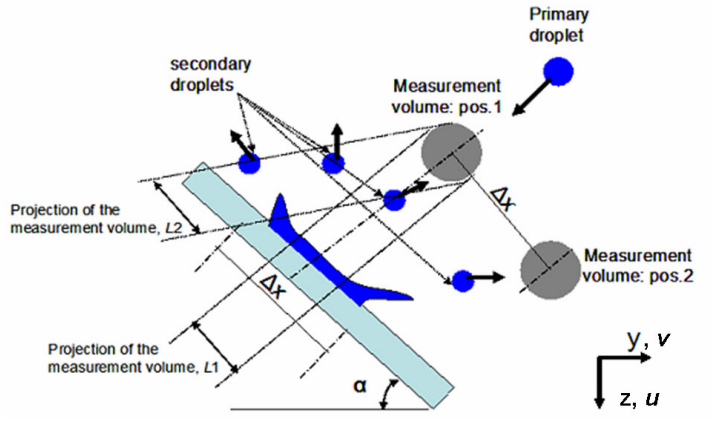

Figure 6.12: schematic of measurement positions

In [70] the procedures of spray impact measurements using the PDA instrument are explained in detail. The experimental setup and the position of the measurement volume is shown in figure 6.12. The original coordinate system {*x, y, z*} is related to the optical configuration of the PDA instrument with the x-axis being the axis of the transmitting optics. Two components

of drop velocity (u and v) and the diameter D are measured above the target surface as schematically shown in figure 6.12.

The geometry of the detection volume must be accurately determined in order to calculate correct local flux density and the droplet distributions in sprays [70]. The length of the measurement volume is determined by the scattering angle Φ and the projected thickness of the slit L_s of the receiving optics [81]. The effective diameter of the measurement volume, d_t, depends on the laser beam intensity, system configuration and the drop diameter. Analyzing the statistics of the burst lengths of detected droplets allows the evaluation of the effective diameter of the measurement volume.

The formulas for volume flux measurements are presented on [70] and for a 2-D system are summarized in [28]. Knowing that the trajectory of each droplet passes through the detection volume, the volume flux in both z and y directions can be calculated using equations 6.8 and 6.9

$$f_u = \frac{\pi}{6\Delta t}\sum_{i=1}^{n}\frac{D_i^3 \cos\psi_i}{A_z(D_k)} \tag{6.8}$$

$$f_v = \frac{\pi}{6\Delta t}\sum_{i=1}^{n}\frac{D_i^3 \sin\psi_i}{A_y(D_k)} \tag{6.9}$$

where D_i and ψ_i are the diameter and the trajectory of individual particles whereby the reference area A_k is taken as a function of the respective size class D_k. In this expression, particles passing through the reference area with a negative velocity will be subtracted from the total mass flux; i.e. when $\cos\psi$ or $\sin\psi$ becomes negative.

Then the normal-to-the-wall velocity component of the incoming and the outgoing droplets is calculated by introducing a vector ($U_n = u\cos\alpha + v\sin\alpha$) as this normal velocity is responsible for the process of the droplet impact and partially for the film generation. The sign of the normal–to-the-wall U_n velocity allows primary drops before wall interaction ($U_n>0$) to be distinguished from secondary droplets ($U_n<0$). The same vector is also introduced to calculate the normal-to-the-wall flux density.

The size-velocity correlation of the droplets measured at 2 mm above the target is shown in figure 6.13. In the present case the impingement distance is 70 mm and the volume flux through the nozzle is 0.45 l/min. The spray exhibits primary impacting droplets with a positive size-velocity correlation. Figure 6.13 (a) shows the raw PDA data before calculating

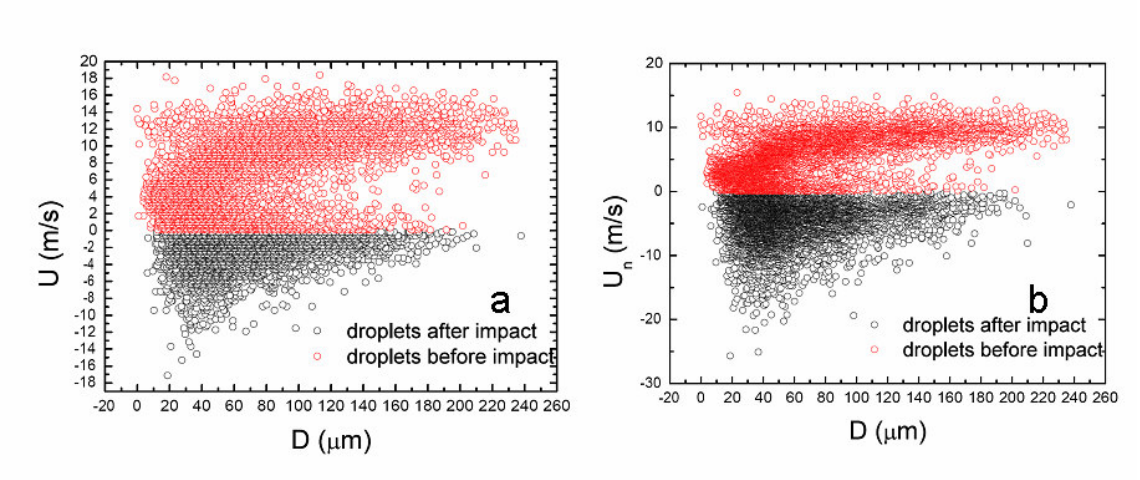

Figure 6.13: Correlation of the drop diameter and velocity for 15° target, 0.45l/min water flow through the nozzle at a selected position 2 mm above the target surface: a) before , b) after coordinate transformation

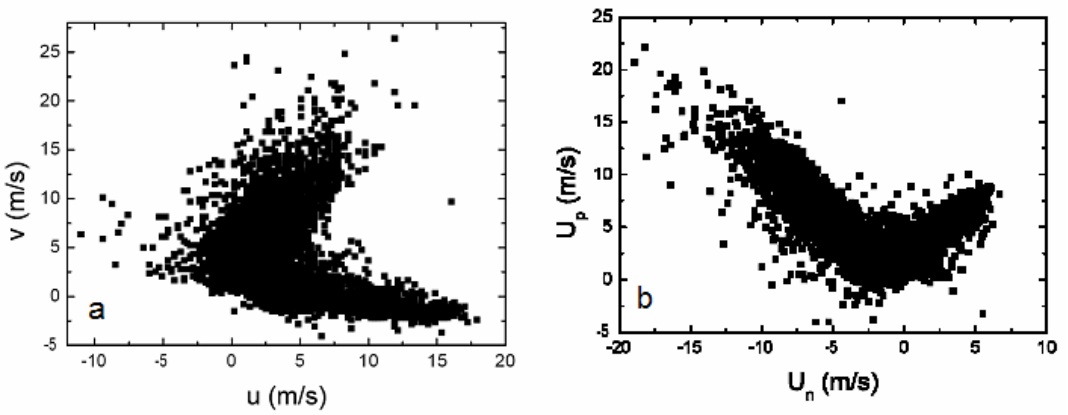

Figure 6.14: Correlation of the drop diameter and velocity for 15° target, 0.45l/min water flow through the nozzle at a selected position 2 mm above the target surface: (left) before, (right) after coordinate transformation

the normal velocity component and figure 6.13 (b) after the data transformation. Applying the coordinate transformation showed a change in the average velocity component and the average droplet size of the secondary droplets.

In figure 6.14, the correlation between the *u* and *v* velocity components before coordinate transformation (left) and after coordinate transformation (right) for a sample case is shown. The correlation of the normal-to-target and the parallel-to-target velocity components show a linear relation between them before and after the impact.

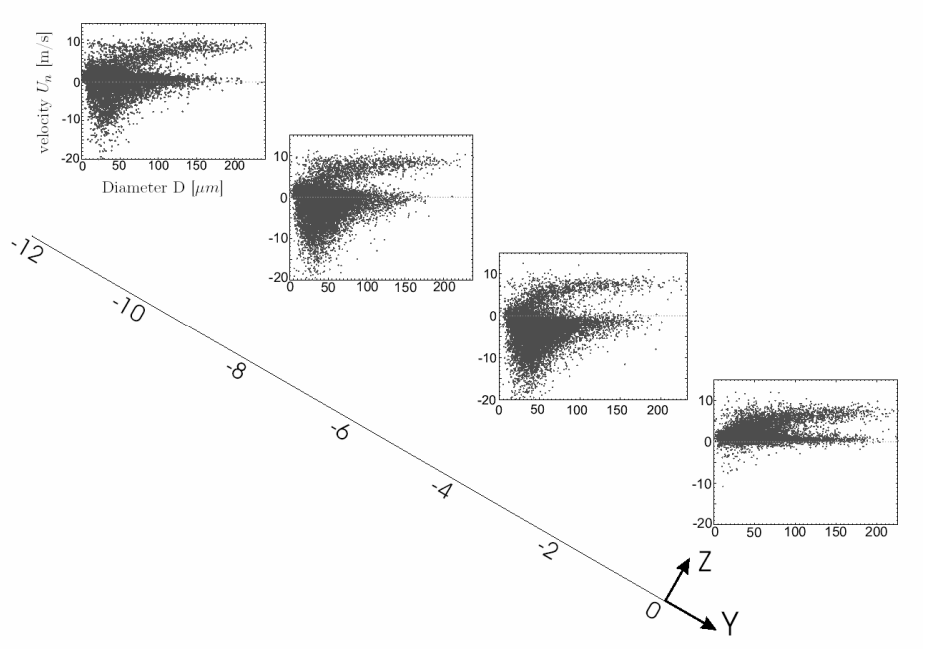

Figure 6.15: Diameter vs. normal-to-target velocity correlation for selected positions on the target surface (30 degrees, 0.45 l/min at z=2mm)

The correlation of droplet diameter and the normal-to-target velocity component depends on the measurement position as shown in figure 6.15. In this figure the correlation is shown in different position on the target at 2 mm above its surface. The plots indicate a change in the secondary droplet velocity-size correlation, close to the lower edge of the target. The plot shows almost no secondary droplets, whereas in the middle of the target the secondary droplets are plentiful.

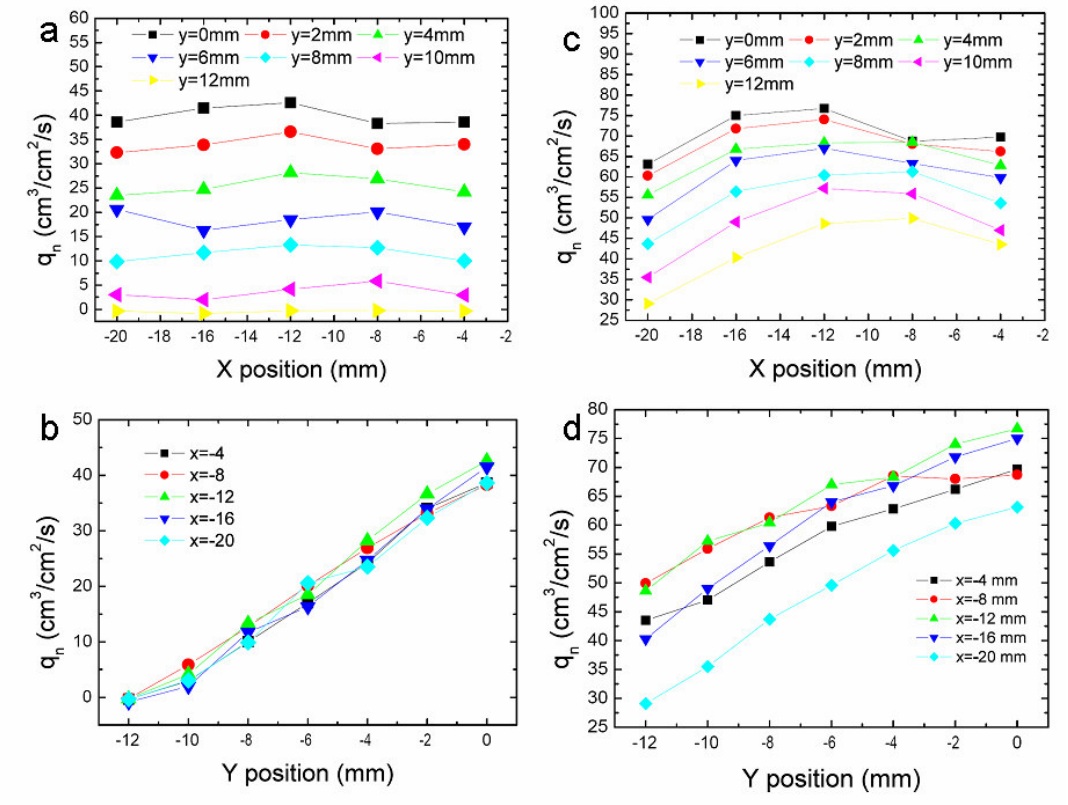

Figure 6.16: Flux density distribution on two different targets

Figures 6.16 (a) and (c) show the net local flux density calculated based on the normal velocity component of the incoming and outgoing droplets along the *x*-direction, and figures (b) and (d) along the y direction for the spray impingement on the targets of 30º and 45º. The total flux through the nozzle in both mentioned cases is 0.45 l/min. These figures show the effect of the target inclination on the local flux distribution. It shows that the local flux is decreasing when moving towards the upper part of the target (or far from the spray axis), which indicates that the secondary droplets ejected by the droplets impingement on the upper part contribute as primary droplets in the lower part. This leads to an increase in the local net flux density. This effect does not appear in the net flux distribution along the *x*-direction as shown in figure 6.16 (a) and (c).

A group of dimensionless numbers is usually used to describe the effect of different factors on the spray impingement phenomenon, namely; Reynolds (Re), Weber (We) and Ohnesorge (Oh) numbers. In this work, the dimensionless numbers and the film thickness are averaged over all measured samples in the three measurement planes for the PDA data, and over 3000 frames for the high-speed camera data.

The splashing phenomenon of the impacting droplets has the appearance of an upraising crown-like liquid sheet. In [81] it has been shown that crown appears if the inertial effects in the lamella are much larger than the capillary effects and the following expression is introduced for the splash threshold.

$$K_i = We_i^{4/5}\,\mathrm{Re}_i^{2/5} = \left[\frac{\rho_L^3 D_i^3 U_{ni}^5}{\sigma^2 \mu}\right]^{2/5} \tag{6.10}$$

In figure 6.17a the ratio between the average outgoing droplet diameter to the average incoming droplets diameter is plotted against K_i. It is shown that the ratio of the ejected droplet size to the primary spray droplet size is almost constant despite the increase of the splash threshold; where as figure 6.17b shows no correlation between the normalized average flux density with the splash threshold.

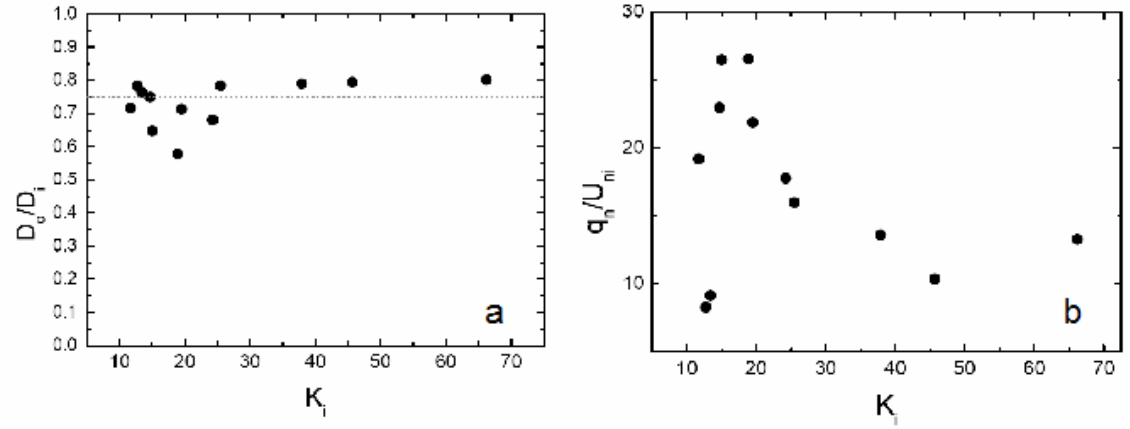

Figure 6.17: a) Outgoing to incoming droplet size ratio and b) dimensionless flux density against splash threshold

Further correlation to describe the relation between the incoming and the outgoing droplets is presented by [81] based on stability analysis of the raising liquid lamella is shown in figure 6.18. The value of $\mathrm{Re}_i^{1/2}\, D_o / D_i$ is plotted against Re_i of the incoming droplets. The figure shows a linear correlation for $\mathrm{Re}_i \geq 250$. Comparing this result with that obtained in [81] for normal spray impact shows a good agreement for the relatively small angles, which indicates that the mechanism of the secondary spray formation in spray impact onto inclined targets is the similar to the normal spray impacts. At higher impact angles (45°, 60°) some discrepancy between the model [81] and the present results accounted for by more significant effect of the tangential component of the impact velocity on the hydrodynamics of splash.

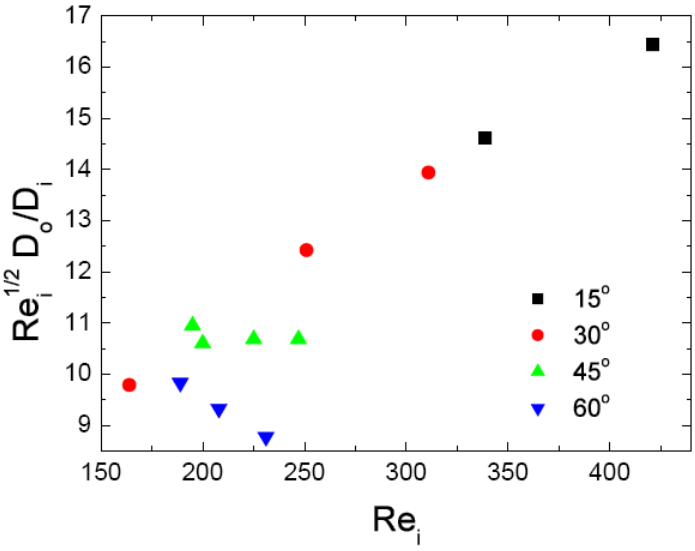

Figure 6.18: The ratio between the outgoing and incoming droplets scaled by Re of the incoming droplets.

6.2.4 Model for the film thickness generated by spray impact

The data obtained by processing the PDA results and the high-speed video camera images is summarized in table 6.1.

In figure 6.19, the 3-D plot shows the film thickness as function of two parameters U_n and q_n. The film thickness H shows an increase when increasing U_n.

Table 6.1: Summary of the results for impact studies

Angle	H_{meas}	**Incoming droplets**					**Outgoing droplets**					q_n
		SMD	U_n	Re	We	Oh	SMD	U_n	Re	We	Oh	
[°]	[mm]	[µm]	[m/s]				[µm]	[m/s]				[cm3/cm2/s]
15	0.145	111	5.49	339	27.7	0.0151	88	3.14	172	8.1	0.0158	56.8
15	0.158	105	6.77	421	41.7	0.0150	84	3.19	170	8.0	0.0161	89.9
30	0.115	117	2.81	164	7.2	0.0157	89	3.11	164	7.8	0.0162	25.7
30	0.128	112	3.95	251	14.4	0.0148	88	3.47	190	9.7	0.0159	63.2
30	0.110	104	5.03	311	22.4	0.0150	82	3.72	196	10.6	0.0162	68.4
45	0.099	139	2.32	195	6.5	0.0129	109	2.70	176	7.0	0.0146	19.2
45	0.116	129	2.66	200	7.7	0.0136	97	3.33	193	9.3	0.0155	61.1
45	0.106	120	3.23	225	10.6	0.0142	86	3.88	200	11.2	0.0164	70.7
45	0.105	110	3.81	247	13.6	0.0146	75	4.11	195	11.6	0.0171	67.7
60	0.097	135	2.12	189	5.9	0.0125	97	2.92	172	7.2	0.0154	40.7
60	0.123	128	2.56	208	7.8	0.0130	83	3.40	172	8.3	0.0165	67.8
60	0.068	121	2.98	231	10.1	0.0133	70	3.96	172	9.6	0.0178	79.1

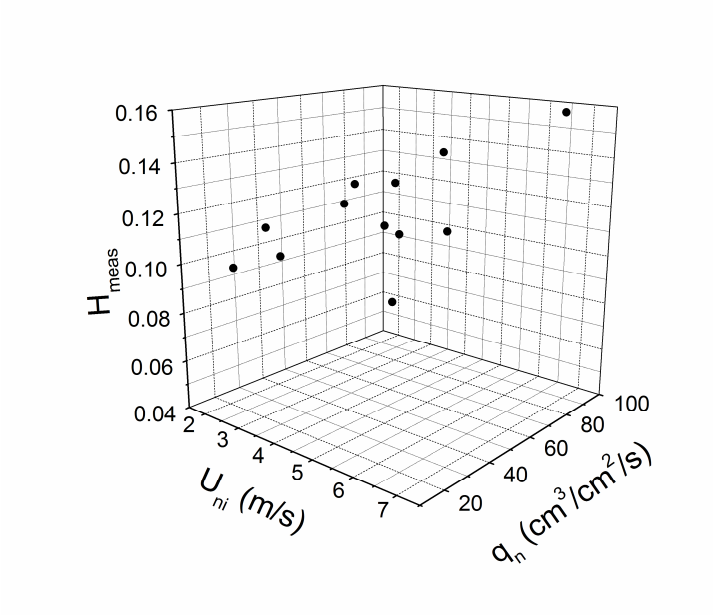

Figure 6.19: The effect of U_n and q_n on the film thickness

The estimation of the film thickness is rather a complicated task since the hydrodynamics of the wall flow generated by spray impact is not completely understood. This flow is determined by the typical time and velocity scales associated with single drop impacts.

The characteristic time scale of the wall flow can be taken as the maximum time of the crown spreading, $T_{\max}$. This time for a single drop impact with the relatively high Weber number is estimated in the study [82] in the following form

$$T_{\max} \approx \frac{\beta HWe}{8U_i}, \qquad \text{where} \quad \beta = 0.62\left(\frac{H}{D_i}\right)^{-1/3} \tag{6.11}$$

The film thickness formed by the relatively sparse spray impact, in which the effect of the single drop impacts is dominant, can be scaled by the thickness of the oscillating viscous boundary layer

$$H_\nu \sim \sqrt{\nu T_{\max}} \tag{6.12}$$

Solution of the equation $H \sim H_\nu$ immediately yields the scaling for the film thickness:

$$\frac{H_{film}}{D_i} \sim \left(\frac{We}{\mathrm{Re}}\right)^{3/4} \tag{6.13}$$

The measured dimensionless film thickness, H/D_i, is shown in figure 6.20 as a function of the dimensionless group $(\mathrm{We/Re})^{3/4} = \mathrm{Ca}^{3/4}$, where Ca is the capillary number. The almost linear

dependence of the dimensionless film thickness on this parameter supports the assumptions. Finally the film thickness produced by spray impact is estimated in the form

$$\frac{H}{Di} = 8.95\,\mathrm{Ca}^{3/4} \tag{6.14}$$

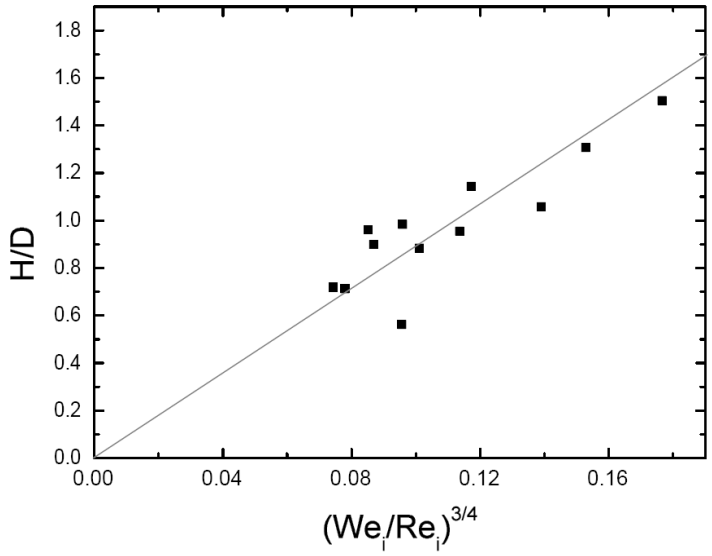

Figure 6.20 Dimensionless film thickness as a function of the parameter $(We/\mathrm{Re})^{3/4}$.

One should admit that at the present stage of research, the proposed empirical model for the film thickness is rather preliminary. The most universal and reliable results can be obtained only after performing experiments over a wide range of the influencing parameters and after complete understanding of the hydrodynamics of the flow generated by spray impacting on a wall. For example, it is of interest to know what is the film thickness generated by sprays with relatively low Reynolds numbers (in which the viscosity significantly influences the impact of single drops) or by very dense fuel spray impact.

In equation 6.14, the right side has a constant and a ratio between We and Re numbers. This constant depends on different parameters, flux density for example. It might also depend on the target angle and the liquid properties.

6.2.5. Application of the spray impact model to the atomizer conditions

High-speed video images are captured to visualize the outcome of the pressure swirl spray impingement onto inclined targets. The images show that no secondary droplets are ejected from the film despite the fact that the Weber number of droplets in the primary pressure swirl spray that impacts onto the pre-filmer in the airblast atomizer have the same range of values as the incoming droplets in the spray impact experiments as shown in figure 6.21.

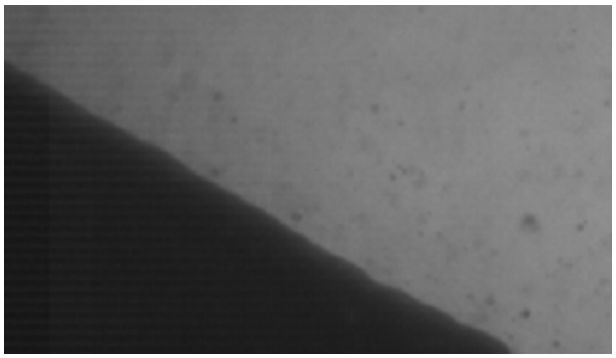

Figure 6.21: Impact of pressure swirl spray (2.66 L/hr) onto 30° inclined target

This qualitative result indicates that almost the total flux of the primary spray contributes in the thin liquid film on the pre-filmer. This implies the primary source of the airblast spray droplets is the disintegration of the thin liquid film on the pre-filmer as a result of its interaction with the high-speed air streams.

The empirical formula (6.14) in the previous section is used to estimate the order of the film thickness in the airblast atomizer. Figure 6.22 shows the ratio of the measured SMD of the airblast spray droplets to the estimated film thickness as a function of We_g in logarithmic scale, where $We_g = \frac{\rho_a H_{film} U_a^2}{\sigma_L}$. The figure shows a strong dependency of the SMD on We_g.

For very low We_g, the generated droplets have SMD values equal or even larger than the estimated film thickness. This can be related to the low air velocity, which indicates that the breakup takes place due to the gravitational and surface tension forces (Rayleigh breakup). As We_g increases, the breakup mechanism starts to be influenced by the shear forces applied by the air stream, therefore, the film starts to deform more before the breakup takes place, which leads to smaller droplet diameters.

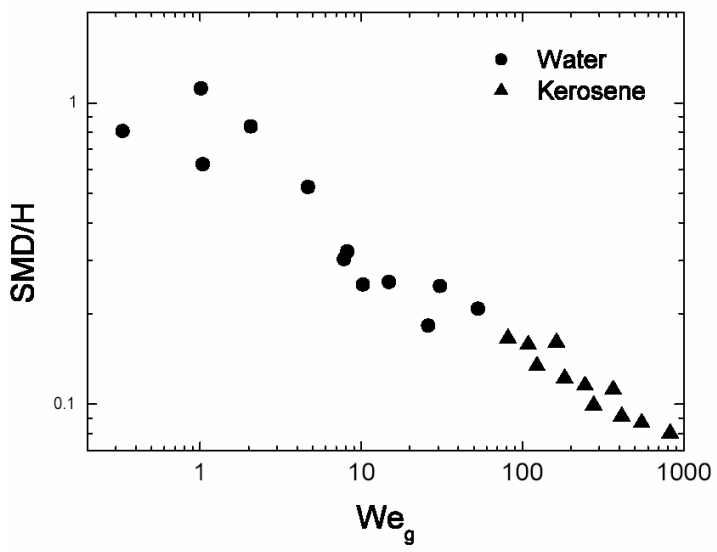

Figure 6.22: The normalized calculated film thickness on the atomizer pre-filmer as a function of We_g

The linear relation showed in logarithmic plot of figure 6.22 indicates a power dependence of the dimensionless drop diameter on the Weber number We_g. The best fit of the experimental data yields

$$\frac{SMD}{H_{film}} \sim We_g^{-0.33} \tag{6.15}$$

This dependence of the Sauter mean diameter of the drops in the airblast spray will be further explained in the following section based on the chaotic disintegration theory of the liquid film.

6.3. Chaotic disintegration model for the size of the drops in spray

The spray generated by an airblast atomizer is influenced by a number of the operating parameters, like the volumetric flow rates of the airflow and of the liquid flow, parameters of the primary spray, pressure in the chamber, material properties of the fluids, etc. Since the mechanism of atomization is extremely complicated the main problem is not the luck in finding formulas relating the operating parameters with the spray parameters.

Such formulations however do not add much to the understanding of the processes occurring inside the atomizer. There is also no confidence that such relations are universal. In this situation the scaling of the problem, relating even one of the parameters with the drop size of the spray can be valuable.

The details of the mechanism of atomization are not considered in the present model. The size of the drop is estimated from the energy balance as in [83].

The primary spray creates a liquid film of the thickness H_{film} on the pre-filmer. The flow in the film is accelerated by the fast airflow. At some instant the film breaks up and creates drops. The initial drop velocity is comparable with the film velocity; therefore, the total kinetic energy cannot be used in the energy balance of the atomization. The main assumption is that the reason for the atomization is the liquid film deformation. The kinetic energy of the film deformation goes to the creation of the surface of the drops.

Consider an element in the liquid film of the typical size *a*. The volume of this element is proportional to a^3. Denote $\dot{\gamma}$ the rate of its deformation. Therefore, the kinetic energy of deformation of the element is approximately

$$E \sim \rho_L a^3 (\dot{\gamma} a)^2 \tag{6.16}$$

During the breakup this energy goes to the creation of the new surface. The corresponding surface energy is estimated as

$$S \sim \sigma a^2 \tag{6.17}$$

The smallest possible drop corresponds to the case when the entire kinetic energy of deformation transforms to the surface energy of the fragment. Therefore, the typical size of the drops, a, can be estimated equating *E* and *S*. The resulting expression is obtained in [83] in the form

$$a \sim \left[\frac{\sigma}{\rho_L \dot{\gamma}^2} \right]^{1/3} \tag{6.18}$$

It is assumed that the main deformation of the liquid and of the gas takes place in a thin turbulent boundary layer. The shear stress at the interface between the liquid and the air can be estimated from the Blasius law in the turbulent boundary layer in the air

$$\tau_w \sim \rho_A U_A^2 \left(\frac{\nu_A}{U_A \delta_A} \right)^{1/4} \tag{6.19}$$

$$\delta_A \sim \left(\frac{U_A x}{\nu_A} \right)^{-1/5} x \tag{6.20}$$

Now, the rate of deformation of the fluid element in the film at the edge of the pre-filmer ($x = L$) is basically the shear stress divided by the film thickness and can be estimated in the form

$$\dot{\gamma} = \frac{1}{H_{film}} \sqrt{\frac{\tau_w}{\rho_L}} \sim \frac{\rho_A^{1/2} U_A^{9/10} \nu_A^{1/10}}{\rho_L^{1/2} H_{film} L^{1/10}} \tag{6.21}$$

The typical size of the drops in the spray can be thus estimated using (6.18)-(6.21) in the follwong form

$$a \sim \frac{H_{film}^{2/3}\sigma^{1/3}L^{1/15}}{\nu_A^{1/15}\rho_A^{1/3}U_A^{3/5}} \tag{6.22}$$

In figure 6.23 the dependence of the *SMD* is shown as a function of the typical size a determined in expression (6.22). It is shown that SMD is proportional to a:

$$SMD = 0.3\,a$$

This linear dependence confirms our assumption that at the relatively high airflow velocities the mechanism of the liquid film atomization can be well described by the chaotic disintegration theory.

It should be noted that not each deforming liquid flow leads to chaotic disintegration. The atomization condition is the smallness of the typical size a (determined by (6.18)) in comparison with the characteristic size of the entire flow region (in our case the film thickness H). In some cases the experimental values of the drop diameters are comparable with the film thickness. These results are related to the experiments under high-pressure conditions where the air velocity is relatively low. The atomization in such cases cannot be described by the chaotic disintegration theory. The corresponding values of the SMD are marked in figure 6.23 as open circles. As expected, their values lie far from the theoretical line, clearly indicating a different mode of atomization.

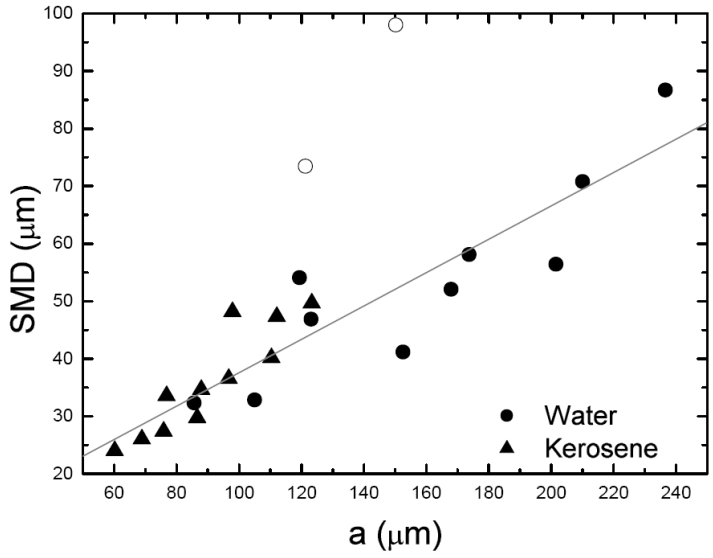

Figure 6.23: SMD as a function of the typical size a, for water and kerosene.

The new expression for a is also checked for data from other experiments for different operating conditions and found to be applicable. For example, the data provided by [15] for kerosene film breakup at room temperature conditions is used and the results fit well as shown in figure 6.23.

To compare this result with that obtained in the previous section, the expression of a can be normalized to the film thickness H and rewritten as a function of We_g as per the following equation.

$$\frac{a}{H_{film}} = \frac{L^{1/15}\sigma^{1/30}}{H_{film}^{1/30}\nu_A^{1/15}\rho_A^{1/30}We_g^{3/10}} \tag{6.23}$$

The theoretical prediction for the ratio a/H behaves as $We_g^{-0.3}$ which is very close to that obtained from the experimental data previously (see the empirical relation (6.15)). The powers of the other terms beside We_g in equation (6.23) are very small; 1/15 and 1/30. These functions change very slowly. Therefore the combination of these terms are almost constant in these experiments.

It should be stated that this model for predicting the SMD of the droplets in the airblast atomizer predicts rather well the Sauter mean drop diameter at the low a/H values. When this value is relatively high the results diverge from the linear dependence as shown in some of the data in figure 6.23.

We should admit that the atomization of the liquid film in the airblast atomizer is rather complicated, but in this work a novel model is introduced which successfully predicts the average diameter of the drops in the spray generated in the airblast atomizer.

The detailed experimental data, collected in the framework of this study and which are used in this model, are listed table 6.2.

Table 6.2: Main integral parameters of primary and aiblast sprays.

Chamber pressure	Airblast spray		Primary spray	
	Air velocity	SMD	U	SMD
Bar	m/s	μm	m/s	μm
1	57.2	54	10.0	55
1	91.1	33	10.6	66
1	130.1	32	11.3	64
1	57.2	58	26.2	47
1	57.2	52	23.2	49
10	5.2	71	5.1	78
10	9.1	98	5.1	78
10	13.0	73	5.1	78
1	57.2	56	36.3	46
1	91.1	41	36.3	46
1	130.1	47	36.3	46
5	10.4	87	19.5	45

7 Conclusions and Recommendations

7.1 Conclusions

This work is aimed at a better understanding of the airblast atomizer and the mechanisms of spray formation. The effect of different parameters; chamber pressure, airflow rate and liquid flow rate on the steady and unsteady features of the airblast spray characteristics is investigated and discussed.

The main achievements and results of this work can be summarized as follows:

1- Qualitative and quantitative characterization of the two phases of the airblast spray and the primary spray is reported and discussed.

2- A novel scaling method for the characteristic frequency of the aerodynamic oscillations in the airblast spray is introduced. Two different techniques used to estimate the spray dominant frequency give the similar frequency estimations.

3- The behavior of airblast spray under oscillating pressure conditions is qualitatively investigated. The effect of the pressure oscillation frequency, pressure oscillation magnitude and the chamber pressure were reported.

4- The mechanisms of airblast spray formation are investigated, discussed and modeled. The thickness of the liquid film on the pre-filmer in the airblast atomizer is estimated through analysis of the spray/wall interaction phenomenon.

5- A new scaling analysis for the droplet size in the airblast spray is proposed based on the energy balance principle in the framework of chaotic disintegration theory. The model is validated by comparison with the experimental data.

7.2 Recommendations

Different suggestions and recommendations can be given to improve the experimental setup and also to further enhance and improve the results obtained in this work.

One of the problems raised during the PDA measurements in the pressure chamber is that the optical access to the chamber becomes wetted during the measurements, which leads to lower data rate and longer measurement times. Introducing heated optical windows would improve the quality of the optical access and eliminate this problem.

Further experiments can be performed to investigate the effect of liquid viscosity on the droplet film thickness in the airblast atomizer.

The effect of oscillating pressure conditions on the airblast spray can be quantitatively investigated based on the qualitative results achieved by this work. This can be done using high-frequency PIV system to obtain droplet velocity. In a more advanced stage, using Interferometeric Particle Imaging (IPI) technique, more information about the change in the droplet size during the oscillatory conditions can be obtained.

The effect of the nozzle geometry on the spray frequency has not been investigated; therefore, the effect of co and counter flow on the studied frequency is an interesting subject for future work.

References

[1] Lefebvre, H. Arthur, GAS TURBINE COMBUSTION, Hemisphere Publishing Corporation, New York 1983.

[2] Olesen, M., Prediction of Drop-Size Distributions Based on Ligament Breakup, Ph.D. thesis, Queen's University at Kingston, Ontario, Canada, 1997.

[3] Fraser R. P.: Liquid Fuel Atomisation. 6th Symposium on Combustion, New York: 687-701, 1957.

[4] Rayleigh, On the Instabilities of Jets, Proceedings London Mathematical Society, 10: 4-13, 1878.

[5] Tyler F., Instability of Liquid Jets, Philosophical Magazine (London) 16, 504-518, 1933.

[6] Weber C., Disintegration of Liquid Jets, Z. Angew, Math. Mech., 11(2): 136-159, 1931.

[7] Haenlein A., Disintegration of Liquid Jets, NACA TN 659, 1932.

[8] Ohnesorge W., Formation of Drops by Nozzles and Breakup of Liquid Jets, Z. Angew, Math. Mech., 16: 355-358, 1936.

[9] York J. I., Stubbs H. E. and Tek M. R., The Mechanism of Disintegration of Liquid Sheets, Transactions of ASME, October 1279-1286, 1953.

[10] Hagerty W. W. and Shea J. F., A Study of the Stability of Plane Liquid Sheets. ASME Applied Mechanics, December: 509-514, 1955.

[11] Dombrowski N. and Fraser R. P., A Photographic Investigation into Disintegration of Liquid Sheets, Philosophical Transactions of the Royal Society of London. Series A, Mathematical and Physical Sciences, Vol. 247, No. 924, September, 1954, pp. 101-130.

[12] Clark C. J. and Dombrowski N., Aerodynamic Instability and Disintegration of Inviscid Liquid Sheets, Proceedings of the Royal Society of London. Series A, Mathematical and Physical Sciences, Vol. 329, No. 1579 September, 1972, pp. 467-478.

[13] Crapper G. D., Dombrowski N. and Pyott G. A. D., Large Amplitude Kelvin-Helmholtz Waves on Thin Liquid Sheets, Proceedings of the Royal Society of London. Series A, Mathematical and Physical Sciences, Vol. 342, No. 1629 February, 1975, pp. 209-224.

[14] Crapper G. D., Dombrowski N. and Jepson W. P., Wave Growth on Thin Sheets of Non-Newtonial Liquids, Proceedings of the Royal Society of London. Series A, Mathematical and Physical Sciences, Vol. 342, No. 1629 February, 1975, pp. 225-236.

[15] Bhayaraju, U. C., Analysis of Liquid Sheet Breakup and Characterisation of Plane Prefilming and Nonprefilming Airblast Atomisers, Ph.D. thesis, Darmstadt, 2007.

[16] Faeth, G.M., L.-P. Hsiang and P.-K. Wu (1995). Structure and Breakup Properties of Sprays. Int. J. Multiphase Flow 21, pp. 99-127.

[17] Faeth, G.M. (2002). Dynamics of Secondary Drop Breakup- a Rate Controlling Process in Dense Sprays. *Proc. ILASS-Europe 2002*, p. Invited Lecture.

[18] Pilch, M. and C.A. Erdman, Use of Breakup Time Data and Velocity History Data to Predict the Maximum Size of Stable Fragments for Acceleration-Induced Breakup of a Liquid Drop. *Int. J. Multiphase Flow* 13, pp. 741-757, 1987.

[19] Findeisen B., Dreizler J. and Hennecke D.K., Untersuchung der Turbulenzstruktur einer verdrallten Brennkammerstroemung, GALA , Kalsruhe, Germany, September, 2004.

[20] Gnirss M., Findeisen J., Damaschke N., Tropea C. and Schiffer H.-P., Experimental Investigation of Coherent Flow Structures in a Gas-Turbine Combustor Model, Tubulence, Heat and Mass Transfer, 2005.

[21] Chrigui M., Batarseh, F. Z., Roisman, I. V., Sadiki A. and Tropea, C., "Numerical and Experimental Study of Spray Produced by an airblast atomizer under Elevated Pressure conditions", Proceedings of ASME Turbo Expo 2008, Berlin, Germany, June, 2008.

[22] Batarseh F. Z., Roisman I. V. and Tropea C., Spray Generated by an Airblast Atomizer under High-Perssure Conditions, Proceedings of ASME Turbo Expo 2007, Power for Land, Sea and Air, Montreal, Canada, May, 2007.

[23] Batarseh F. Z., Roisman I. V. and Tropea C., Effect of Primary Spray Characteristics on the Spray Generated by an Airblast Atomizer under High-Pressure Conditions, ILASS Americas, Orlando, Florida, May, 2008.

[24] Batarseh F. Z., Chrigui M., Janicka J., Roisman I. V., Sadiki A. and Tropea C., "Spray Produced by an Airblast Atomizer under Elevated Pressure Conditions: Experimental and Numerical Study", International Conference on Multiphase Flow, ICMF, Leipzig, Germany, July, 2007,

[25] Batarseh F. Z., Gnirss M., Roisman I. V. And Tropea C., Aerodynamic Instability of a Spray Generated by an Airblast Atomizer, Proceedings if ILASS-Europe, September, 2007.

[26] Batarseh F. Z., Gnirss M., Roisman I. V. and Tropea C.,Fluctuations of a Spray Generated by an Airblast Atomizer, Experiment in Fluids, Accepted, 2008.

[27] Albrecht, H.-E., Borys, M., Damaschke, N. and Tropea, C., Laser Doppler and Phase Doppler Measurement Techniques, Springer, Heidelberg 2003.

[28] Dantec Software Catalogue, BSA Flow Manager, Tousbakken 16-18, 2740 Skovlunde, Denmark, 2005.

[29] Becker J. and Hassa Ch., Experimental Investigation of Spatial and Temporal Aspects of the Liquid Fuel Placement in a Swirl Cup at Elevated Pressure, Proceedings of ASME Turbo Expo 2004, Power for Land, Sea and Air, Vienna, Austria, June, 2004.

[30] Christanti Y, Walker L (2006) Quantifying Air Atomization of Viscoelastic Fluids Through Fluid Relaxation Times. Atomization and Spray 16(7):777–790

[31] Merlo-Sosa L, Cota-Sanchez G, Soucy G (2006) Effect of the Liquid Atomization Quality on the Pyrolysis of Organic Compounds by Induction Thermal Plasma. High Temp Mater P-US 10(1):79–102

[32] Karnawat J, Kushari A (2006) Controlled Atomization Using a Twin-Fluid Swirl Atomizer. Exp Fluids 41:649–663

[33] Clack H, Koshland C, Lucas D, Sawyer RF (2004) Development of an Airblast Atomizer for Independent Control of Droplet Size and Spray Density. Atomization and Spray 14(3):265–287

[34] Uhm J. H. and Acharya S., Low-Bandwidth Open-Loop Control of Combustion Instability. Combust Flame 142(4):348–363, 2005.

[35] Lee J. Y, Lubarsky E, Zinn B. T, Slow Active Control of Combustion Instabilities by Modification of Liquid Fuel Spray Properties. P Combust Inst 30:1757–1764, part 2, 2005.

[36] Midgley K, Spencer A nad McGurik J J, Vortex Beakdown in Swirling Fuel Injector Flows In: ASME Turbo Expo: Fostering Gas Turbine Education, Technology & Networking, The American Society of Mechanical Engineers, Montreal, Canada, GT2007-27803, 2007.

[37] Van Maanen H., Nobach H. and Benedict L., Improved Estimator for the Slotted Autocorrelation Function of Randomly Sampled LDA Data. Meas Sci Tech 10:L4–L7, 1999.

[38] Nobach H., Local Time Estimator for the Slotted Correlation Function of Randomly Sampled LDA Data, Experiments in Fluids 32, 337-345, 2002.

[39] Nobach H., Mueller E. and Tropea C., Correlation Estimator for Two-Channel, non-Coincidence Laser-Doppler-Anemometer, Proceedings 9th International Symp. on Applications of laser Techn. to Fluid Mechanics, Lisbon, July, 1998.

[40] Lumley J. L., The Structure of Inhomogeneous Turbulent Flows Atmospheric Turbulance and Radio Wave Propagation ed A M Yaglom and Tatarsky V. I., (Moscow: Nauka) pp 166-178, 1967.

[41] Bekooz G, Holmes P, Lumley J., The Proper Orthogonal Decomposition in the Analysis of Turbulent Flows. Ann Rev Fluid Mech 25:539–575, 1993.

[42] Gnirß M, Tropea C., Simultaneous PIV and Concentration Measurements in a Gas-Turbine Combustor Model. In: 7th International Symposium on Particle Image Velocimetry, Rome, Italy, 2007.

[43] Wang X., F., and Lefebvre A., H., Mean Drop Sizes from Pressure-Swirl Nozzles, AIAA J. Propul. Power, Vol. 3 No. 1, pp. 11-18, 1987.

[44] Lorenzetto, G.E., and Lefebvre, A.H.,"Measurements of Drop Size on a Plain Jet Airblast Atomizer", AIAA J. 15, 1006–1010, 1977.

[45] Rizk, N.K., and Lefebvre, A.H. "Spray Characteristics of Plain-Jet Airblast Atomizers", Trans. ASME J. Eng. Gas Turbines Power, 106, 639–644, 1984.

[46] Rizkalla, A.A., and Lefebvre, A.H., The Influence of Air and Liquid Properties on Airblast Atomization, Trans. ASME J. Fluids Eng. 97, 316–320, 1975.

[47] El-Shanawany, M.S. M.R., and Lefebvre, A.H., Airblast Atomization: The Effect of Linear Scale on Mean Drop Size, J. Energy 4, 184–189, 1980.

[48] Lefebver, Arthur H., ATOMIZATION and SPRAYS, Hemisphere publishing corporation, 1989.

[49] Lefebvre A. H., Properties of Sprays, Part. Part. Syst. Charact. 6, 176-186, 1989.

[50] Lefebvre A. H., Some Recent Developments in Twin-Fluid Atomization, Part. Part. Syst. Charact. 13, 205-216, 1996.

[51] Jasuja A. K. and Lefebvre A. H., Pressure-Swirl Atomizer Performance under Varying Air Pressure Conditions, ILASS Europe, Toulouse 7-7 July 1999.

[52] Rao K. V. L. and Lefebvre A. H., Fuel Atomization in a Flowing Airstream, Technical Notes, October 1975.

[53] Rizk N. K. and Lefebvre A. H., Airblast Atomization: Studies on Drop-Size Distribution, J. Energy, Vol. 6 No. 5, Sep.-Oct. 1982.

[54] Rizk N. K. and Lefebvre A. H., Influence of Atomizer Design Features on Mean Drop Size, AIAA Journal, Vol. 21, No. 8, August 1983.

[55] Wang X. F. and Lefebvre A. H., Atomization Performance of Pressure-Swirl Nozzles, AIAA Journal, 1986.

[56] Wang X. F. and Lefebvre A. H., Influence of Fuel Temperature on Atomization Performance of Pressure-Swirl Atomizers, J. Propulsion, Vol. 4, No. 3, 1987.

[57] Beck J. E., Lefebvre A. H. and Koblish T. R., Airblast Atomization at Conditions of Low Air Velocity, J. Propulsion, Vol. 7, No. 2, March-April 1991.

[58] Chen S. K. and Lefebvre A. H., Influence of Ambient Air Pressure on Effervescent Atomization, L. of Propulsion and Power, Vol. 9, No. 1, Jan.-Feb. 1993.

[59] Ortman J. and Lefebvre A. H., Fuel Distribution from Pressure –Swirl Atomizers, J. Propulsion, Vol. 1, No. 1, Jan.-Feb. 1985.

[60] Ingebo, R.D., Atomization of Liquid Sheets in High Pressure Airflow, ASME Paper HTWA/HT-27, 1984.

[61] Becker J., Heitz D. and Hassa Ch., Spray Disperesion in a Counter-Swirling Double-Annular Airflow at Gas Turbine Conditions, ILASS Europe 2001, Zurich, September 2001.

[62] Hage M., Dreizler A. and Janicka J., Flow Fields and Droplet Diameter Distributions of Water and N-Heptane Sprays at Varied Boundary Conditions in a Generic Gas Turbine

Combustor, Proceedings of ASME Turbo Expo 2007, Power for Land, Sea and Air, Montreal, Canada, May, 2007.

[63] Roisman I. V. and Tropea C., Impact of a Drop onto a Wetted Wall: Description of Crown Formation and Propagation, Journal of Fluid Mechanics, vol. 472, pp. 373-397, 2002.

[64] Bai C. X., Rusche H. and Gosman A. D., Modeling of Gasoline Spray Impingement, Atomization and Sprays, Vol. 12, pp. 1-27, 2002.

[65] Bai C., and Gosman A. D., Development of Methodology for Spray Impingement Simulation, SAE paper, no. 950283, 1995.

[66] Mundo C., Sommerfeld M. and Tropea C., On the Modeling of Liquid Sprays Impinging on Surfaces, Atomization and Sprays, vol. 8, pp. 625-652, 1998.

[67] Roisman I. V. and Tropea C., Fluctuating Flow in a Liquid Layer and Secondary Spray Created by an Impacting Spray, International Journal of Multiphase Flow, vol. 31, pp. 179-200, 2005.

[68] Panao, M.R.O., and Moreira, A.L.N.,: Experimental Study of the Flow Regimes Resulting from the Impact of an Intermittent Gasoline Spray, Experiments in Fluids, Vol. 37, pp. 834-855, 2004.

[69] Mundo, C., Tropea, C., and Sommerfeld, M.: Numerical and Experimental Investigation of Spray Characteristics in the Vicinity of a Rigid Wall, Experimental Thermal and Fluid Science, Vol. 15, pp. 228-237, 1997

[70] Roisman I. V. and Tropea C., Flux Measurements in Sprays using Phase Doppler Techniques, Atomization and Sprays, vol. 11, pp. 667-699, 2001.

[71] Dhiman, R., and Chandra, S.,: Freezing-Induced Splashing During Impact of Molten Metal Droplets with High Weber Numbers, International Journal of Heat and Mass Transfer, Vol. 48, pp. 5625-5638, 2005.

[72] Sivakumar D. and Tropra C., Splashing Impact of a Spray onto a Liquid Film, Physics of Fluids, Vol. 14(12), pp 85-88, 2002.

[73] Cossali G. E., Marengo M. and Santini M., Single-Drop Empirical Models for Spray Impact on Solid Walls: a Review, Atomization and Sprays, vol. 15, pp. 699-736, 2005.

[74] Samenfink W., Grundlegende Untersuchung zur Trofeninteraktion mit Schubspannungsgetriebenen Wandfilmen, Ph.D. thesis, Universitaet Karlsruhe, Germany, 1997.

[75] Park K. and Watkins P., Comparison of Wall Spray Impaction Models with Experimental Data on Drop Velocities and Sizes, Int. J. Heat Fluid Flow, vol. 17, pp. 424-438, 1996.

[76] Stanton D. W. and Rutland C. J., Modelling Fuel Film Formation and Wall Interaction in Diesel Engines, SAE Paper No. 960628, 1996.

[77] Marengo M. and Tropea C., Aufprall von Tropfen auf Fluessigkeitsfilme, DFG, Zwischenbericht zum Forschungsvorhaben, vol. 194, pp. 10-18, 1999.

[78] Tropea C. and Roisman I. V., Modeling of Spray Impact on Solid Surfaces, Atomization and Sprays, vol. 10, pp. 387-408, 2000.

[79] Weiss, C.,: The Liquid Deposition Fraction of Sprays Impinging Vertical Walls and Flowing Films, International Journal of Multiphase Flow, Vol. 31, pp. 115-140, 2005.

[80] Roisman I. V., Prunet-Foch B., Tropea C. and Vignes-Adler M., Multiple Drop Impact onto a Dry Solid Subtrate, Journal of Colloid Interface Science, vol. 256, pp. 396-410, 2002.

[81] Roisman I. V., Horvat K. and Tropea C., Spray Impact: Rim Transverse Instability Initiating Fingering and Splash, and Description of a Secondary Spray, Physics of Fluids Vol. 18, 102104, 2006

[82] Roisman I. V., Van Hinsberg N. P. and Tropea C., Propagation of a Kinematic Instability in a Liquid Layer: Capillary and Gravity Effects, Phys. Rev. E, 77, 046305, 2008.

[83] Yarin, A.L. FREE LIQUID JETS and FILMS: HYDRODYNAMICS and RHEOLOGY, John Wiley & Sons, Inc., New York, 1993.

[84] Gambaryan-Roisman T., Kyriopoulos O., Roisman I. V., Stephan P., and Tropea C., Gravity Effect on Spray Impact and Spray Cooling. 2nd International Topical Team Workshop on Two-Phase Systems for Ground and Space Applications. Kyoto, Japan, 2007.

Syna'a Street-Bayader Wadi Alsair
P.O.Box:851439 Amman
11185 Jordan
Tel:+962 6 5856630/1
Fax: +962 6 5865766
Mobile: +962 79 5533386
E-mail: fbatarseh@wathba.com

Feras Z. Batarseh

Experience

July 2008- **Wathba Inv. Co. ltd.** Amman - Jordan

General Manager

June,1999-March, 2005 **Wathba Inv. Co. ltd.** Amman - Jordan

Sales and Marketing Manager	January, 2004 – March, 2005
Technical Department Manager	July, 2002- December, 2003
Tenders and Major Projects Dept. Manager	July, 2001 – June, 2002
Technical Support Supervisor	July, 2000 – June, 2001
Technical Support Engineer	June, 1999 – June, 2000

Education

2005 - 2008 TU Darmstadt Darmstadt – Germany

PhD in Mechanical Engineering (Thesis title "Spray generated by an air-blast atomizer: atomization, propagation and aerodynamic instability")

2001 – 2003 The University of Jordan Amman – Jordan

M.Sc in Mechanical Engineering (Thesis title Performance Study of Radiant Panel System for Heating and Cooling)

1995 – 1999 The University of Jordan Amman - Jordan

B.Sc. in Mechanical Engineering (finished my study in 4 years)

(Final year project title is Tunnel Ventilation)

Scholarships, sponsored activities and awards

DAAD: German Academic Exchange Service, **(Darmstadt-Germany, 2005)**

ESA parabolic flight campaign for *micro* gravity experiments and gravity-loss simulation, "Investigation of surface tension effects on liquid transportation on structured surfaces" **(Bordeaux-France, 2007)**

Training Courses

Improving your leadership skills by success (November 2001)

Improving your management skills by success (November 2001)

Leadership in 21st century by SGS. (April 2002)

New way in strategically planning by SGS. (April 2002)

Industrial Projects

IPI measurements of non-transparent spray – Daimler/ Mercedes – Fraunhofer Institute – Stuttgart – Germany (November 2007)

Impact of iso-octan spray onto heated target – simulation of benzene spray impact in SI BMW engine – BMW – Germany

	(October 2007) Developing data base for shower-head flow through characterizing breakup of water jets using high-speed video camera – Hansgrohe – Schiltach – Germany (October 2007) Characterization of glue spray for pharmasutical applications – Novartis Pharma – Darmstadt – Germany (June 2006)
Publications	Batarseh F. Z, Roisman I. V. and Tropea C., Spray generated by an airblast atomizer under high-pressure conditions, Proceedings of ASME Turbo Expo 2007, Montreal, Canada, 18-21 May, 2007. Batarseh F.Z., Chrigui M., janicka J., Roisman I. V., Sadiki A. and Tropea C., Spray produced by an airblast atomizer under elevated pressure conditions: experimental and numerical study, ICMF, Leipzig, Germany, 9-13 July, 2007 Batarseh F. Z., Gnirss M., Roisman I. V. and Tropea C., Aerodynamic instability of a spray generated by an airblast atomizer, proceedings of ILASS Europe, Turkey, September, 2007. Batarseh F. Z., Gnirss M., Roisman I. V. and Tropea C., Fluctuations of a spray generated by an airblast atomizer, Experiment in Fluids, Accepted 2008. Batarseh F. Z., Roisman I. V. and Tropea C., Effect of primary spray characteristics on the spray generated by an airblast atomizer under high-pressure conditions, ILASS Americas, Orlando, Florida, 18-21 May, 2008.
Personal Information	Date of Birth: December 9th, 1977 Nationality: Jordanian Gender: Male Current situation: Single Hobbies: Sport and Traveling
Languages	**Arabic:** Tongue language **English:** V. good **German:** Good
References	**Eng. Bassem Farradj** Owner and CEO Wathba Inv. co. Mobile: +962 (079) 552 4070 Amman - Jordan **Prof. Cameron Tropea** Institute of Fluid Dynamics and Aerodynamics Tel.: +49 (06151) 16 2854 Darmstadt – Germany